POLITECNICO DI TORINO

DIPARTIMENTO DI ELETTRONICA E TELECOMUNICAZIONI

CORSO DI LAUREA MAGISTRALE IN NANOTECHNOLOGIES FOR ICTs

SESSIONE DI LAUREA LUGLIO 2023

High-Performance and Miniature Greenhouse Gas Sensor for Drone-based Remote Sensing

Relatore:
Carlo Ricciardi

Correlatori:
Matteo Rinaldi
Pietro Simeoni

Laureando:
Aurelio Venditti

ANNO ACCADEMICO 2022 - 2023

Abstract

Human activities have significantly increased the concentration of greenhouse gases in the atmosphere, intensifying the greenhouse effect and contributing to global climate change. Since CO_2 is the most abundant greenhouse gas to be released in the atmosphere, the effect of the others is calculated with respect to it through the global warming potential, which estimates the energy-trapping capability of a gas with respect to CO_2 over a 100-years period. Among all the main other greenhouse gases, N_2O has a global warming potential of around 270, while its concentration is about 3 orders of magnitude smaller than the one of CO_2, leading to a contribution to heat-trapping approximately equal to the 25% of the one of CO_2. This makes an accurate assessment of N_2O emissions essential. Unlike CO_2, the main source of N_2O released into the atmosphere is agricultural land use. However, many technical challenges associated with the capability of achieving reliable emission estimates with low uncertainties at the field level come out due to the significant variations of N_2O flux in space and time and they are ultimately attributed to the lack of suitable sensors and platforms that can precisely capture the in-field variations in a large area while remaining low cost and non-invasive to farming activities. Researchers have been striving to overcome these limitations and a novel approach combining piezoelectric MEMS resonators with plasmonic metamaterials has been recently proposed, offering advantages including ultra-miniaturized footprint, low power consumption, and high detection accuracy. This innovative approach typically involves an oscillator loop that includes a resonator covered by a spectrally selective metamaterial layer. When the incident IR light is absorbed by the metamaterial and converted into heat, the resulting temperature change causes a shift in the admittance response of the resonator, thereby altering the oscillator frequency.

The purpose of this thesis is to design through numerical simulations, fabricate, and test a sensor achieving a measurement sensitivity of N_2O molecules' concentration at the ppb level by combining a MEMS-based spectrally-selective IR detector with an IR spectroscopic gas cell. The enabling technology is laser absorption spectroscopy, which allows the detection of trace gases molecules through the absorption of highly coherent IR light at wavelengths that corresponds to their roto-vibrational states: the optical power of the IR laser beam passing through the gas cell is modulated by the concentration of N_2O molecules and sensed by the detector. This thesis eventually provides the experimental demonstration of the functioning of all the sub-parts of the designed system. In particular, it presents the first implementation of a high temperature coefficient of frequency ($TCF \sim$ - 55 $ppm/°C$) and good electromechanical properties ($Q_m \sim$ 800 and $k_t^2 \sim$ 3.3%) 30%-doped $ScAlN$ resonator on a patterned interdigitated bottom electrode with an enhanced absorption peak of 80% at a wavelength of 4.8 μm. This result has been achieved by replacing SiO_2 with AlN as the dielectric layer of the metal-insulator-metal metamaterial absorbers without compromising the IR absorbance.

Contents

List of Figures

List of Tables

Chapter 1

Introduction

Earth's atmosphere is a gaseous layer that regulates the exchange of energy between the planet and outer space. Changing its composition changes the net energy absorbed in the atmosphere, affecting its temperature and climate patterns. This is referred to as the greenhouse effect. There are 4 main greenhouse gases (GHG) that are released into the atmosphere by human activity: carbon dioxide (CO_2), methane (CH_4), nitrous oxide (N_2O), and water vapor H_2O. Since CO_2 is the most abundant gas to be released in the atmosphere, the effect of the other GHG is calculated with respect to it through the Global Warming Potential (GWP), which estimates the energy-trapping capability of a gas with respect to CO_2 over a 100-years period. N_2O has a GWP of around 270, while its concentration is about 3 orders of magnitude smaller the one of CO_2 (nowadays the average concentration of N_2O is around 350 ppb, while the one of CO_2 is around 400 ppm). This means that the contribution of N_2O to heat-trapping is approximately equal to the 25% of the one of CO_2. However, unlike CO_2, the main source of N_2O released into the atmosphere is not fossil fuels burning, but rather agricultural land use. In fact, the main cause of the increase of N_2O atmospheric concentration is anthropogenic emissions, and over 80% of the current global anthropogenic flux is related to agriculture, including associated land-use change.

In particular, agricultural soil management-produced N_2O is a primary contributor to the total N_2O emissions in the United States [1]. Therefore, monitoring N_2O emissions from agricultural lands will have a significant impact on the agricultural and energy sectors because:

1. N_2O molecules are $\sim$ 300 times more powerful than CO_2 as a greenhouse gas (GWP of $\sim$ 270), and have an atmospheric lifetime of $\sim$ 114 years, thereby making N_2O the third most important anthropogenic GHG [2];
2. N_2O is a dominant ozone-depleting substance [3];
3. N_2O emissions to the atmosphere are extremely heterogeneous with a high spatial and temporal variability [4], and are often characterized by high episodic fluxes [5];
4. N_2O emissions are expected to increase by 20% through land-use change and agricultural intensification (in particular, fertilizer use) by 2030 [6].

Therefore, an accurate assessment of N_2O emissions from agriculture activities is vital not only for understanding the global N_2O balance and its impact on climate but also for designing crop systems with lower GHG emissions, since any irregular N_2O emissions in farmlands can be an indicator of over-fertilization [7]. However, such assessments are currently hampered by the lack of instrumentation and methodologies to measure ecosystem-level fluxes at appropriate spatial and temporal scales. In fact, there are many technical challenges associated with producing reliable emission estimates with low uncertainties at the field level due to the significant variations of N_2O flux in space and time. These unresolved challenges are ultimately attributed to the lack of suitable N_2O sensors and platforms that can precisely capture the in-field variations in a large area while remaining low-cost and non-invasive to farming activities.

For example, a typical Eddy Covariance (EC) system requires a stationary tower mounted with complex and expensive instrumentation for near-continuous and highly accurate measurements of gas concentrations and air movements, which are not only not scalable due to the cost but also disruptive to the farming management. Therefore, drone-based remote sensing of N_2O emissions was recently proposed with the hope to address the challenges associated with coverage, cost, and interference with farming practices. Indeed, thanks to the airborne advantage, drone-based sensing can provide wide-area sensing without large costs or big equipment. In fact, this concept of using drones and onboard imaging sensors for the survey of large areas of agricultural lands gathering information about crop, soil, and field conditions has long existed and is well-studied in both research and industrial domains. However, in terms of greenhouse gas emission monitoring, the drone-based approach remained a largely unexplored area primarily due to the complexity involved with integrating an EC system with the constantly moving aerial platform.

However, while being a promising approach considered from these aspects, new challenges emerged because of the drastically changed sensing platform, which is now highly mobile and extremely sensitive to the size, weight, and power (SWaP) of the attached instruments. In fact, commercially available N_2O sensors that meet the performance requirement for stationary EC systems are simply too heavy and power-hungry for drone operation. Furthermore, their sampling speed is not fast enough to capture the concentration of N_2O when the drone is cruising at a high speed. As a consequence, the severely impacted flight time per charge and the insufficient time resolution of N_2O measurement greatly limits the capability of the drone system to capture the temporal variation of N_2O flux in the field, hence the accuracy of the estimated overall emission throughout a growing season. Therefore, innovations at the sensor level aiming at greatly reduced SWaP and fast speed are required to enable the integration of N_2O sensors with drones for greenhouse gas emission monitoring and reduction.

1.1 Overview

Molecular absorption spectroscopy has a number of applications in the detection and quantification of small traces of biomarkers, toxins, or other interesting molecules in gaseous samples. Examples of these applications are atmospheric and environmental monitoring of trace gases.

From the fundamental point of view, the detection sensitivity can be optimized by doing spectroscopy in the mid-wavelength infrared (MWIR) region, where many trace gas molecules have their strongest absorption features. In fact, most trace gas molecules have their fundamental rotational-vibrational bands in this region. These latter are typically at least two orders of magnitude stronger than the respective overtone bands. The so-called *atmospheric window* at 3–5 μm is particularly important, as it occupies the strongest absorption bands of the carbohydrates (CH stretch) and molecules with NH or OH stretching vibration. It is also worth noting that within the atmospheric window water vapour absorption is relatively small.

Direct laser absorption spectroscopy (DAS), in which the mid-infrared laser beam is passed through the gas sample and then detected using a photodetector, is the simplest method for trace gas analysis. When used for spectroscopy of strong fundamental vibrational transitions of molecules, this translates into a detection limit of 1 ppm with a typical absorption path length of 1 m. An obvious solution to improve the sensitivity of trace gas detection is to increase the absorption path length. Apart from certain applications in atmospheric monitoring, an increase of the path length simply by placing the detector far away from the light source is impractical. A common approach to achieve a path length of up to a couple of hundred meters is to use a multipass cell (MPC). The spectrometers based on multipass cells are relatively simple, compact, and robust, and hence suitable for field applications of trace gas detection. While the increase of absorption path length by use of an MPC aims at enhancement of the absorption signal, the spectrometer performance can also be improved by noise-reduction techniques, based on modulation. The detection sensitivity of DAS can be improved by 2–3 orders of magnitude by using wavelength modulation spectroscopy (WMS) or frequency modulation spectroscopy (FMS). As an example, a 3.3 μm light source combined with an 80 m Herriot cell has been used to detect CH_4 in the air with a sub-ppb detection sensitivity. Other compounds measured in air with similar setups and with essentially similar performances include CO (5 ppb), N_2O (2 ppb), and CO_2 (100 ppb). As usual, these measurements were carried out using a sample pressure lower than the atmospheric pressure, to reduce pressure broadening of the absorption lines and hence to improve the spectroscopic resolution and selectivity [8].

In recent years, the field of infrared (IR) sensing has witnessed significant advancements. IR sensing is a versatile technology that finds applications in a variety of domains, including thermal imaging, medical diagnostics, and spectroscopy for chemical fingerprinting and threat detection [9] [10] [11]. The mechanics of IR sensors can be broadly classified into two categories: photon detection-based and temperature measurement-based. While photon detection-based sensing offers high resolution, it comes at the cost of increased system complexity, necessitating active cooling in most cases. On the other hand, temperature-based sensing approaches typically feature simpler designs, but their sensitivity is limited. Therefore, researchers have been striving to overcome this trade-off by developing methods to improve the sensitivity of temperature-based IR sensors. Notably, examples of such methods include bolometers [12], thermopiles [13], and pyroelectric [14] detectors. More recently, a novel approach combining piezoelectric microelectromechanical system (MEMS) resonators with plasmonic metamaterials has been proposed, offering advantages including ultra-miniaturized footprint (chip area < 1 mm^2), low power consumption (~ 1 mW), and high detection accuracy (ppb level). This innovative approach typically involves an oscillator loop that includes a resonator covered by a spectrally selective metamaterial layer. When incident IR is absorbed by the metamaterial and converted into heat, the resulting temperature change causes a shift in the admittance response of the resonator, thereby altering the oscillator frequency.

The main aim of this project is the implementation of a N_2O concentration sensor with an accuracy $\sim$ 1 ppb based on IR-absorption spectroscopy. However, the detector is not a photodetector, but a MEMS based on a resonator on top of which plasmonic metamaterial absorbers are integrated to selectively absorb IR radiations at the required wavelength. The overall system design is constrained by SWaP matrices coming from its final application since it is going to be mounted on a drone in order to map the concentration of N_2O over crop fields.

1.2 Proposed technology

The use of unmanned aerial vehicles (UAVs) for atmospheric research is rapidly growing. In fact, UAV platforms have demonstrated promise for atmospheric chemistry field studies, and, as an example shown in Figure 1.1, they are already used for such a kind of purpose. The ease of deployment and high maneuverability of UAVs allow sampling areas relatively inaccessible with conventional platforms, particularly within the planetary boundary layer of the troposphere. The main alternatives to such a kind of application are suborbital research aircraft with onboard pilots, but they do not fly over populated areas at low altitudes, volcanoes, or into severe weather for safety reasons. Moreover, remote sensing measurements from satellites do not have the vertical or horizontal spatial resolution to identify local sources, sinks, and distributions of air pollutants and trace gases within the Earth's boundary layer, while tethered balloons and kites can provide vertical resolution measurements but only over a single location, and their deployment is limited to specific weather conditions.

Figure 1.1: Drone-based remote sensing: application example. The payload carried by the drone includes a sensor capable of properly working on such a platform.

Following this trend, the proposed solution uses a new class of high-performance and miniature gas sensors based on laser absorption spectrometry (LAS) and advanced MEMS resonant IR detectors to implement a lightweight and power-efficient IR-spectroscopy N_2O sensing system suitable for drone mounting, dramatically increasing the area that can be monitored compared to EC systems at a fraction of the cost. In particular, taking into account both SWaP constraints and the performance of current EC flux towers [15], the initial target specifications for the proposed system were the following:

1. $< 1\ W$ power consumption (drone constrained);
2. $< 400\ g$ weight and $< 0.5\ L$ volume (drone constrained);
3. $\sim 1\ ppb$ accuracy (comparable to EC systems);
4. $> 20\ Hz$ sampling rate (based on EC system $1\ Hz$ rate for $7\ mph$ wind).

It is worth mentioning that, after a more detailed analysis of the system, these specifications have been slightly refined in section 4.1 to make the sensor more feasible without losing applicability and quality in its performance. Therefore, a high-performance ($\sim 1\ ppb$ accuracy with $> 10\ Hz$ sampling rate), low-power ($< 2.5\ W$ power consumption), and ultra-miniaturized ($<$ 0.5 L volume and $< 500\ g$ weight) IR spectroscopy-based N_2O gas sensor suitable for drone-based remote sensing, as the one shown in Figure 1.2, will be eventually developed. Such an unprecedented combination of high performance and SWaP is achieved by the combination of a Herriott cell with the development of ultra-fast detection speed and high-resolution uncooled MEMS IR detector, together with the adoption of state-of-the-art uncooled low-power quantum cascade laser (QCL) and the design of a proper low-noise and low-power read-out circuit. In fact, MEMS-based spectrally-selective IR detectors, as a newly emerged counterpart to conventional thermal detectors, allow for fast and high-resolution IR detection enabled by their low noise performance, high thermal sensitivity, and the seamless integration with spectral filters at the microdevice level. In particular, the enabling technology consists of a Scandium-doped Aluminum Nitride ($ScAlN$) laterally vibrating resonator (LVR) on top of which a near-perfect nano-plasmonic narrowband IR absorbers suitable for ultra-high resolution and fast spectroscopic IR sensing is integrated. The unique combination of such a piezoelectric-plasmonic MEMS sensing technology with a low-noise and low-power read-out circuitry results in an IR spectrometer microsystem characterized by an excellent IR detection capability (noise equivalent power, NEP $\sim 100\ pW/Hz^{1/2}$), ultra-miniaturized footprint (total chip area of $< 2\ mm^2$), low power consumption ($\sim 1\ mW$), and fast response ($< 100\ ms$ per spectral scan).

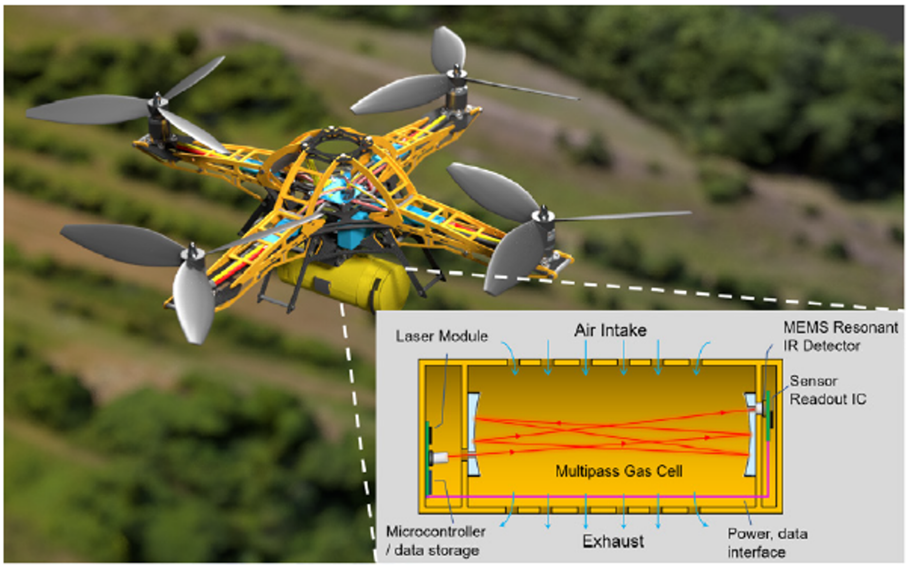

Figure 1.2: Schematic illustration of the proposed gas sensor for drone-based remote sensing.

The innovation lies in the integration of the plasmonic metamaterial absorber on top of the piezoelectric LVR. The integration of plasmonic structures in the design of $ScAlN$ nanoplate resonant thermal detectors allows to achieve of strong and narrowband absorption in such deeply subwavelength thin resonant structures while maintaining high piezoelectric transduction and quality factor, hence low noise performance. In fact, a plasmonic absorber allows to have high spectral resolution to absorb a specific wavelength and this is what is needed for the final application because N_2O absorption peak is centered at 4.5 μm, being sandwiched between the CO (4.7 μm) and CO_2 one (4.3 μm). Such a high spectral resolution cannot be achieved without bulky and/or expensive cooling and filtering systems to limit noise in the current state-of-the-art IR sensors previously described, except with plasmonic metamaterial absorbers.

1.3 Thesis structure

The thesis has been divided into six main chapters:

- Chapter 1 - brief introduction of the thesis work, including its context, aims, main starting hypothesis, and assumptions;
- Chapter 2 - presentation of the state of the art. It refers to the frame taken at the moment the thesis work started of the level of the general development of the technology used to achieve the N_2O concentration detection problem. It defines the context where the thesis' work takes place and shows its starting point and background;
- Chapter 3 - description of the operating principle of the system under study from the purely theoretical standpoint;
- Chapter 4 - presentation of the methods used to identify the final specifications of the system, the steps followed to fabricate its core, and the experimental setup needed to test its correct functioning;
- Chapter 5 - description of the performed numerical simulations, presentation of the obtained results on which a first design of the system has been conducted, and first experimental proof of the single sub-parts of the system;
- Chapter 6 - discussion of the experimental results shown in the previous chapter, potential different applications of the same technology, and possible future studies.

1.4 Thesis notation

The notation used throughout this thesis is specified in Table 1.1.

Symbol or acronym	***Definition***
AC	Alternating Current
ADC	Analog-to-Digital Converter
Al	Aluminum
AlN	Aluminum Nitride
BAW	Bulk Acoustic Wave
CH_4	Methane
CMOS	Complementary Metal-Oxide-Semiconductor
CO	Carbon Monoxide
CO_2	Carbon Dioxide
COTS	Commercial Off The Shelf
CW	Continuous Wave
DAS	Direct Absorption Spectroscopy
DC	Direct Current
EC	Eddy Covariance
FBAR	thin Film Bulk Acoustic wave Resonator
FEM	Finite Element Method
FIT	Finite Integration Technique
FMS	Frequency Modulation Spectroscopy

FoM	Figure of Merit
FTIR	Fourier Transform Infrared
FWHM	Full Width at Half Maximum
GC	Gas Chromatography
GHG	GreenHouse Gas
GWP	Global Warming Potential
H_2O	Water
HWHM	Half-Width at Half-Maximum
IC	Integrated Circuit
ICL	Interband Cascade Laser
IDE	InterDigitated Electrode
IoT	Internet of Things
IR	InfraRed
LAS	Laser Absorption Spectroscopy
LED	Light Emitting Diode
$LiNbO_3$	Lithium Niobate
LVR	Laterally Vibrating Resonator
MBVD	Modified Butterworth-Van Dyke
MEMS	MicroElectroMechanical Systems
MIM	Metal Insulator Metal
MWIR	Mid-Wavelength InfraRed
MPA	Metamaterial Perfect Absorber
MPC	MultiPass Cell
N_2O	Nitrous Oxide
$NaCl$	Sodium Chloride
NDIR	Non-Dispersive InfraRed
NEMS	NanoElectroMechanical Systems
NEP	Noise Equivalent Power
Pt	Platinum
PZT	Lead Zirconate Titanate
QCL	Quantum Cascade Laser
RF	Radio Frequency
$ScAlN$	Scandium-doped Aluminum Nitride
SEM	Scanning Electron Microscope
SiO_2	Silicon Dioxide
SNR	Signal-to-Noise Ratio
SOP	Short Open Load
SP	Surface Plasmon
SWaP	Size Weight and Power
WMS	Wavelength Modulation Spectroscopy
T2M	Technology-to-Market
TCF	Temperature Coefficient of Frequency
TIPS	Total Internal Partition Sums
VNA	Vector Network Analyzer
ZnO	Zinc Oxide

Table 1.1: Description of the symbols and acronyms used throughout the thesis.

Chapter 2

State of the art

This section deeply describes the state of the art of every technology involved in this project.

2.1 Nitrous oxide sensors

The rapid development of advanced and versatile drones in commercial space has enabled a number of applications for agriculture purposes. However, the constraints on payload weight and size still prevent the use of drones for more sophisticated remote sensing other than imaging. For instance, even an industrial-grade drone optimized for loading capacity suffers a flight time reduction of $\sim 40\%$ when carrying a payload of only 3 kg [16]. In the context of monitoring N_2O emissions with drones, this shortened flight time per charge means smaller coverage and possibly missed pulse emission events (i.e., "hot moments"), which leads to increased operational cost and inaccurate estimation of season-long emissions. While the hybrid drones currently under development may provide relief to the problem to some extent, miniaturization of high-precision sensors represents a more sustainable approach leading to enhanced capabilities and reduced cost of any kind of drone-based remote sensing platforms.

Nowadays N_2O monitoring mostly uses tower-mounted EC systems. This technology is bulky and power-hungry. As such, it is not scalable. In fact, state-of-the-art N_2O sensors that meet the performance requirement for stationary EC systems are simply too heavy and power-hungry for drone operation. Furthermore, their sampling speed is not fast enough for the measurement of N_2O concentration when the drone is cruising at a high speed. As a consequence, the severely impacted flight time per charge and the insufficient time resolution of N_2O measurement will greatly limit the capability of the drone system to capture the temporal variation of N_2O flux in the field.

In general, state-of-the-art gas sensors are either high-performance or highly portable, but not both. Conventional N_2O concentration sensing methodologies including gas chromatography and IR spectroscopy have been used in quantifying N_2O emissions in the agricultural sector. A comparison of state-of-the-art gas sensing technologies is shown in Table 2.1.

	FTIR	**Electron Capture**	**Gas Chromatography**	**Electro-chemical**	**Thermopile NDIR**	**LAS MEMS Gas Sensors**
Resolution	$\sim$ 1 ppb	$\sim$ 10 ppb	$\sim$ 10 - 100 ppb	$\sim$ 10 ppm	$\sim$ 10 ppm	$\sim$ 1 - 1000 ppb
Power use	High	High	High	Moderate	Low	Moderate / High
Cost	High	High	High	Moderate	Moderate	Moderate / High
Size	Benchtop	Benchtop	Benchtop / Portable	Portable	Portable	Portable

Table 2.1: Comparison of the state-of-the-art greenhouse gas sensors

For low-cost in-field N_2O flux measurements, a chamber is typically used for monitoring N_2O concentration change above the soil for a short duration of time. Static and automatic chambers are the most widely used techniques for quantifying soil N_2O flux in the field. These devices allow for a fine-scale study of fields and are relatively inexpensive. However, static chambers are often associated with significant labor efforts and reduced measurement reliability due to the need of manually collecting air samples. Furthermore, laboratory offline analysis of collected samples by gas chromatography (GC) is required to determine the N_2O concentrations. Automatic chambers can achieve higher reliability by substituting manual sample collection with an automated configuration but at the cost of increased system complexity (GC analysis is still required). There have been few demonstrations of chamber-based in-field N_2O measurement setups that combine both sample collection automation and in-field gas analysis. However, they have been used only for research purposes in test fields due to the massive size of the setup (that would inevitably interfere with regular farming activities), as well as the high cost of the required equipment. Nevertheless, compared to EC analyzers, the coverage of a chamber is very limited and therefore does not sufficiently address spatial heterogeneity. Dense deployment of chambers could solve the problem, but the installation of many chambers can introduce disturbances to soil, plants, and field operations.

Benchtop GC requires a continuous supply of high-purity carrier gases which leads to an overall bulky and power-inefficient system. The transportation from the field to the lab and the slow throughput (each analysis can take up to 10 minutes) further prevent frequent sampling to acquire high-resolution data (both spatial and temporal) even from the lab [17]. On the other hand, IR spectroscopy technologies provide a reliable alternative solution for non-disruptive analysis of gas composition with a fast measurement speed and high resolution. In fact, in the past decade IR spectroscopy has become a key technique in laboratory environments for accurate and non-disruptive analysis of chemical composition [18]. In general, IR sensing is a versatile technology that finds applications in a variety of domains, including thermal imaging, medical diagnostics, and spectroscopy for chemical fingerprinting and threat detection. The mechanics of IR sensors can be broadly classified into two categories: photon detection-based and temperature measurement-based. While photon detection-based sensing offers high resolution, it comes at the cost of increased system complexity, necessitating active cooling in most cases. On the other hand, temperature-based sensing approaches typically feature simpler designs, but their sensitivity is limited. In particular, photonic detectors exploit the interaction between photons and electrons in a semiconductor material to produce an electrical output signal upon exposure to infrared radiation. They have the advantages of a high signal-to-noise ratio (hence high resolution) and fast response time. However, to achieve such a high performance, they typically need cryogenic cooling to prevent thermally generated carriers, making them bulky, expensive, and power inefficient. On the other hand, thermal detectors rely on the temperature-induced change of material physical properties upon exposure to infrared radiation. They are generally less expensive, more compact, and power efficient than semiconductor photon detectors, given their intrinsic capability to operate at room temperature, but they exhibit relatively worse resolution and slower response time [19].

Generally, two types of IR spectroscopic gas sensors are available: non-dispersive infrared (NDIR) and laser absorption spectroscopy (LAS). Although both are based on IR absorption spectroscopy, NDIR gas sensors do not require a laser to operate since they rely on optical filters in front of the IR sensors to achieve spectral selectivity. Therefore, they feature a small footprint, low-cost, and power-efficient solutions for fast and reliable measurements on the go. However, the NDIR technique for in-field measurement of N_2O has not been extensively utilized due to the fundamental challenges associated with the state-of-the-art MWIR detectors and the inherent spectral interference by other environmental species. The resolution of state-of-the-art NDIR gas sensors (~ 10 of ppm) is limited by the poor noise performance (noise equivalent power, NEP $\sim 10\ nW/Hz^{1/2}$) of the commercially available uncooled IR detector technologies (i.e. thermal detectors) [20]. Furthermore, existing NDIR sensors inherently require additional external filtering elements for spectral analysis making the spectral resolution, the sensitivity (i.e. the detection of low concentration N_2O, for example within other background gases such as CO_2), and the possibility of miniaturization particularly poor. The reason is that N_2O (main absorption peak at $\lambda \sim 4.5\ \mu m$) is closely located CO_2 (main absorption peak at $\lambda \sim 4.3\ \mu m$) in their IR absorption spectra, which causes strong interference if the band-pass IR filters are not ideal (moreover, it is worth noting that CO_2 concentration in atmosphere is about 3 orders of magnitude higher than that of N_2O). For this reason, commercially available N_2O detectors are equipped with a pre-detection gas absorbent (such as soda lime desiccant to reduce the interfering gas concentration) and multiple narrowband IR filters (leads to high cost), which are unfavorable for in-field N_2O sensing applications that require low cost and miniaturization [21]. Another challenge associated with the miniaturization of NDIR N_2O sensors is the requirement of a relatively large multipass optical gas cell. Extending the optical path length is an effective way to achieve high resolution (i.e., low minimum detectable gas concentration) for all IR absorption spectroscopy gas sensors (with the trade-off of power and speed). However, the non-dispersive broadband IR source used in NDIR sensors produces diverging light, hence impossible to achieve a long path ($> 5\ m$) in a compact gas cell ($< 1\ L$). In this context, the coherent and collimated light produced from a laser is advantageous in terms of immunity to interference from CO_2 and the miniaturization of gas cells. However, in most LAS systems designed for Eddy Covariance measurement (with $\sim ppb$ accuracy), the laser source itself is cumbersome and power-hungry due to the high output power and the active cooling. The high-power laser also leads to the use of a large capacity battery pack for untethered operation which further increases the size and weight of the system. In principle, the MWIR laser can be miniaturized thanks to the recent advances in uncooled low-power QCLs [22]. However, in order to achieve $\sim 1\ ppb$ level detection limit, a cooled IR photodetector must be used which again leads to increased size and power consumption due to the cooling requirement. With existing uncooled thermal detector technologies (i.e., thermoelectric and pyroelectric sensors), such miniaturization directly results in a 400 times reduced accuracy for greenhouse gas measurement [23] making them incapable of in-field monitoring of greenhouse gas emissions. On the other hand, existing uncooled thermal detectors also limit the maximum sampling speed of the gas sensor to $\sim 1\ Hz$ due to their relatively large thermal constant and the required long averaging time in the readout circuit to reduce the noise. Such a sampling rate is sufficient for stationary EC systems but too slow for the measurement conducted on a cruising drone since the required sampling rate increases as average wind speed increases [15]. This essentially means the drone must be kept at a low speed for continuous measurement or operated in a stop-and-go mode for discreet measurement.

More recently, there has been a growing demand for exploring such IR spectroscopy techniques beyond traditional laboratory settings. In fact, the ongoing trend in sensor development toward compact size, power efficiency, and reliable measurement has accompanied the increasing effort to implement ultra-miniaturized IR spectrometers, in lieu of the conventional IR spectrometers that are bulky, costly, and power inefficient. The implementation of compact IR spectrometers can enable fast and accurate chemical composition analysis on the go, allowing for the IR spectroscopy technique to be easily accessible in diverse applications. In this context, resonant IR detectors are the ideal candidates, thanks to the fast response and high resolution enabled by their low noise performance, high thermal sensitivity, and the use of frequency shift as the output parameter for high measurement accuracy. In fact, among different micro/nano electromechanical systems (MEMS/NEMS) sensor technologies, the one based on a resonant-sensing mechanism offers significant advantages over other non-resonant approaches. In general, micro–nanoresonant sensors are characterized by a unique combination of high sensitivity to external perturbations, due to the greatly reduced dimensions of the sensing element, and ultra-low noise performance, due to the intrinsically high quality factor of such resonant systems. Furthermore, resonant sensors use frequency as the output variable, which is one of the physical quantities that can be monitored with the highest accuracy and converted to digital form by simply measuring zero crossings. In particular, among different resonant IR sensor technologies the one based on aluminum nitride (AlN) piezoelectric nanoplate resonant thermal detectors has shown unique advantages in terms of detection limit, response time, and detector size. This is due to the fact that, differently from any other piezoelectric materials, high-quality AlN thin films can be deposited on any arbitrary substrate using a low-temperature sputtering process, enabling the fabrication of ultralow volume resonators with high electromechanical performance due to the significantly reduced thermal mass of the resonant element. Such advantages combined with the post-Complementary Metal-Oxide-Semiconductor (CMOS) compatible microfabrication process make the AlN resonant thermal detector technology one of the most promising candidates for the implementation of ultra-compact, high resolution, and fast IR detectors [24].

2.2 Optics

2.2.1 IR light source

From the technological point of view, the highest sensitivity, i.e., the capability of detecting small concentrations can usually be obtained by using laser spectroscopy. This results from the high brightness and spatial coherence of lasers, which makes it possible to reach high signal-to-noise ratios and long absorption path lengths. The high brightness also means that the high measurement sensitivity can be obtained with a short averaging time, which leads to fast, in practice real-time measurements. Also the spectroscopic selectivity, i.e., the capability of resolving one molecular absorption line or species from another, is superior in laser spectroscopy, as compared to more conventional methods. In particular, the high spectral resolution and hence high selectivity can be obtained by using single-mode continuous-wave (CW) lasers [8].

Mid-infrared molecular spectroscopy and, in particular, its application to trace gas analysis, has progressed significantly during the past two decades, owing to the development of coherent mid-infrared sources, detectors, and methods. One of the important enabling technological advances has been the invention of room-temperature quantum cascade lasers (QCL) and interband cascade lasers (ICL), which have extended the operating range of tunable semiconductor lasers from the visible and near-infrared to the mid-infrared. In particular, the use of recently introduced ICL as an alternative to the QCL operating at ambient temperature led to the huge benefit of operating at substantially lower power.

2.2.2 Multipass cell

In laser spectroscopy, it is often needed to measure the absorption coefficient of light in a gas, or some other effect resulting from the interaction of the gas with light. The gas under test is often within some type of gas cell because, in order to obtain a high detection sensitivity of the spectroscopic measurement, it is often needed to realize a long path length of the light in the gas [25].

In principle, it could be possible to use a correspondingly long single-pass gas cell. This approach, however, is often not practical, mostly because the gas cell would become too bulky to be integrated into a compact device. Therefore, for these kinds of applications, it is usual practice to use multipass cells (MPCs), where a long path length is realized by multiple passes through a moderately long cell. Moreover, realizing a small gas volume for a given path length can be important for some applications. For example, it could be necessary to achieve a fast turnover of the gas in the cell in order to rapidly monitor changes in the composition of the gas in the environment [26].

A common feature of MPCs is that the beam path is folded by some kind of highly reflecting mirrors that are often characterized by concave surfaces, which provide some refocusing of the beam so that the beam radius can be kept relatively small throughout the cell, even when realizing a long beam path. Curvatures of mirrors also often serve the purpose of appropriately modifying the propagation direction of the laser beam. Further, a large number of reflections is usually obtained by using only two or three different mirrors so that reflections occur on multiple points on the same mirrors. Different designs of such MPCs differ in various aspects such as:

- how many passes can be realized;
- whether it is possible to vary the number of passes;
- how difficult and critical the alignment of the mirrors is;
- how small the gas volume can be made;
- how sophisticated mechanical parts are required;
- how the beam radius evolves during the passage.

A particularly simple MPC is the Pfund cell (see Figure 2.1a), invented by August Pfund in the late 1930s for atmospheric studies, which consists of two identical concave spherical mirrors, each one having a hole carefully machined at their center. An input beam is injected through such a hole at some angle, such that it hits the reflecting part of the other mirror and, after one reflection, the beam is always parallel to the axis of the gas cell. The second reflection directs the beam toward the hole in the other mirror. The distance D between the mirrors is set to be half their curvature radius r, i.e. equal to their focal length f. The precise direction of the input beam and the beam divergence are not critical. A modified version has a hole only in the first mirror so that the output beam passes back through the hole of the input mirror after five reflections, i.e. six passes instead of three.

Circular MPCs (see Figure 2.1b) were first introduced by Thoma and co-workers in 1994 [27]. This type of MPC has all the reflection points around a circle, so that beam enters the cell under a certain angle and propagates depicting a path with a star-shaped pattern. The path length can be varied by adjusting the incidence angle ϕ of the beam. It is possible to use a separate spherical mirror for each reflection point arranged along a circular shape so that its curvature radius can be arbitrarily chosen. Alternatively, a single circular mirror can be used, which can essentially be the only part of the whole cell, making it mechanically simple and robust. In fact, the main advantage lies in their robustness towards mechanical stress such as vibrations or temperature changes. However, in the latter case, the radius of curvature is of course half the diameter of the mentioned circle and cannot be freely chosen. Such cells can be used to realize a relatively large number of passes in combination with a rather small cell volume [28].

The White cell was first described in 1942 by John U. White and was a significant improvement over previous long-path spectroscopic measurement techniques [29]. It is made of three spherical concave mirrors (see Figure 2.1c), in particular a larger one on one side and two smaller ones on the other side, all having the same radius of curvature. They are separated by a distance equal to their radii of curvature r, i.e. equal to twice their focal length f. Due to the splitting of the mirrors on one side, i.e. mirrors M2 and M3, one can independently adjust their orientation to the laser beam by making slight rotational adjustments, which allows to realize different numbers of passes. However, the total number of traversals is always an integer multiple of four. The input beam is injected from the side of mirror M1, rather than through a hole as for the Pfund cell. The entering and exiting beams do not change position as passes are added or removed, while the total number of traversals can be increased many times without changing the volume of the cell, and therefore the total optical path length can be made large compared to the volume of the sample under test. The spots from various passes can overlap on mirrors M2 and M3 but must be distinct on mirror M1. If the input beam is focused in the plane of M1, then each round trip will also be focused in this plane. The tighter the focus, the more nonoverlapping spots there can be on M1 and so the higher the maximum path length.

However, for realizing a large number of passes, it is common practice to use the design of the Herriott cell, named after Doland R. Herriott [30] [31], which consist of only two facing spherically curved mirrors (see Figure 2.1d), or alternatively a flat and a curved mirror. A hole is machined into one of the mirrors to allow the input and output beams to enter and exit the cavity. Alternatively, the beam may exit through a hole in the opposite mirror. In a Herriott cell, the beam is somewhat away from that axis so that the reflection points on each mirror lie in a circle around the mirror center. After each round trip, the reflection point advances by a certain angle that depends on the ratio of mirror distance D and curvature radius, which affects also the evolution of beam radius. Moreover, unlike the White cell, also the number of passes is controlled by adjusting the separation distance between the two mirrors.

At present the White cell is still the most commonly used MPC and provides many advantages. For example, the number of passes is easily controlled so that it is available with path lengths ranging from less than a meter to many hundreds of meters, it allows for high numerical aperture, and it is reasonably stable [32]. However, the Herriott cell has some advantages over the White cell. In particular, the Herriott cell is simpler than the White cell because it has only two mirrors that are easier to position and less susceptible to mechanical disturbance of the cell. This makes the Herriott cell more stable than the White cell to small perturbations. However, the Herriot cell does not accept high numerical aperture beams. In addition, larger-sized mirrors must be used when longer path lengths are needed.

The mechanical stability is the main reason why the Herriott cell has been selected for this project due to the highly unstable platform on which the system will be mounted.

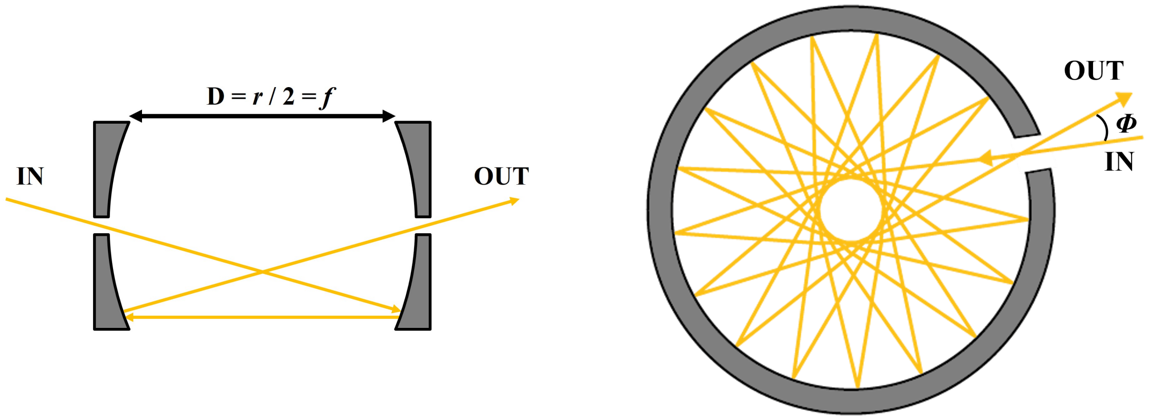

(a) Pfund cell.

(b) Circular cell.

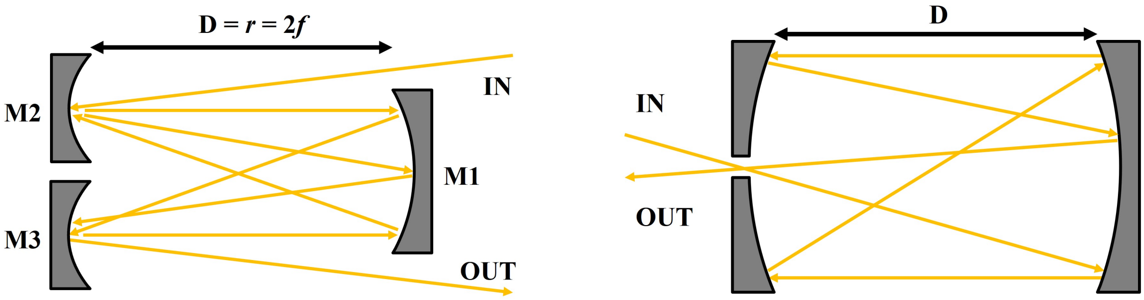

(c) White cell.

(d) Herriott cell.

Figure 2.1: Different architectures of multipass cells.

2.3 MEMS

2.3.1 Plasmonic absorber

In a general IR absorption spectroscopy system, the characteristic IR response of a sample is recorded by a detector, which typically relies on a highly IR-absorbing material. Spectrally selective IR absorbers, in particular, are key components for implementing compact IR spectroscopy systems, as they completely eliminate the need for additional narrowband filter elements to discriminate spectral regions of interest. The achievement of high absorbance in a narrow spectral band is particularly important for IR spectroscopy, since multiple chemical species may exhibit strongly confined spectral emission/absorption bands closely located to each other, like the current example of the N_2O molecule absorption peak, which is centered around 4.5 μm, thereby being sandwiched between the CO (4.7 μm) and CO_2 one (4.3 μm).

Moreover, both the acceptance angle and polarization sensitivity of the absorbers play a significant role in maximizing the total absorption. On the other hand, due to the burgeoning development of miniaturized sensors with the advent of the Internet of Things (IoT), nowadays the demand for compact IR sensor arrays capable of addressing multiple wavelengths in a small form factor has been steadily growing. Therefore, the key challenge lies in realizing miniaturized multispectral absorber arrays monolithically integrated on the same chip, with a minimized footprint. This challenge has been tackled in the field of plasmonics and metamaterials, which is a rapidly growing research field that has enabled the design of materials with optical properties not found in nature, which allows overcoming the diffraction limit and focusing light in deep subwavelength volumes. Metamaterial perfect absorbers (MPAs), in particular, are artificial materials composed of an array of subwavelength structures that manipulate electromagnetic waves to achieve extraordinary light absorption properties and plasmonic IR absorbers leverage the strong light–matter interaction enabled by surface plasmons (SPs) at deep subwavelength scales to achieve ideal absorber responses. Therefore, driven by the advent of the IoT, MPAs have been employed in microelectromechanical systems for the development of efficient and miniaturized IR detectors thanks to their lithographically tunable peak absorption, ultra-narrow spectral selectivity, and ultrathin thickness. In fact, MPAs characterized by high near-unity absorbance in narrow spectral bands are particularly desirable for the implementation of high-resolution IR spectroscopic sensors.

The Metal-Insulator-Metal (MIM) Metamaterial IR absorbers have been studied and employed in a variety of applications due to their unique characteristics of lithographically-controlled absorption wavelengths and near-unity absorption with little constraints on angle and polarization [33]. As a matter of fact, these characteristics have made these absorbers the ideal candidates for a new class of plasmonically-enhanced IR sensing microsystems, such as spectrally selective microbolometers [34], MEMS resonance IR sensors, solar cells [35], refractive index sensors [36] [37], thermal sensors [38] [39], surface-enhanced spectroscopy [40], and optically actuated micromechanical photoswitches [41].

The MIM IR absorbers used in this project adopt a similar structural configuration as the artificial metamaterial with magnetic response reported in [42], which consists of an array of two parallel layers of metallic structures separated by a thin dielectric gap inducing the effective electric and magnetic responses that are different from the bulk-state materials. However, differently from the last mentioned approach, the here adopted structure for the MIM IR absorbers has an un-patterned bottom metallic layer that is an optically thick continuous plane to suppress any transmitted power of incident IR, separated from an array of plasmonic nanostructures by a subwavelength thick dielectric spacer. Furthermore, even if other arbitrary structures such as square and circular patches have been demonstrated in the past, the strong 2D plasmon excitation of 4-fold symmetric cross-shaped nanostructures ensures a better field confinement and a response with minimal constraints on the property of incident IR waves (i.e., angle and polarization insensitivity), while maintaining spectral selective near-unity absorption [43]. Therefore, MIM IR absorbers with 4-fold symmetric cross-shaped nanostructures are almost independent of incident angle and polarization of the impinging IR radiation. In fact, it is found that the cross-shaped nanostructures with a high length-to-width ratio and a wider periodicity result in maximized field confinement and reduced cross-talk (minimized capacitive coupling between neighboring plasmonic nanostructures), leading to the narrow absorption bandwidth reaching its limit, while maintaining a near unity absorption at peak wavelength and angle and polarization insensitivity due to both the axial XY-symmetry of the cross-type nanostructure and the vertical field confinement in the sub-wavelength thickness of the structure [44]. These unprecedented absorption properties are key enablers for the development of a new class of miniaturized, low-cost, and high-resolution plasmonically enhanced IR sensing microsystems.

An analytical tool that captures the physics of the system, i.e. that directly relates absorption properties, with respect to the characteristic parameters, such as geometric dimensions and constituent materials, of MIM IR absorbers, is particularly important when designing an absorber with specific process constraints, such as lithography limits or material compatibility, or for specific high-performance applications. However, many analytical models proposed to date unfortunately failed to provide all the characteristic absorption properties or did not give insights into the geometric configurations of the plasmonic nanostructures or the electric dipole resonance between them. Sakurai et al. first proposed an RLC equivalent circuit model to describe the magnetic response of the MIM IR absorbers by interpreting the plasmonic absorption as an RLC resonance inside the system and the associated loss [45] [46]. In particular, an LC circuit model provided a helpful understanding of the MIM IR absorber, such as the prediction of the resonance frequency, i.e. location of peak absorption wavelength of an arbitrary MIM IR absorber [45]. Nevertheless, in addition to the resonance frequency, the bandwidth of the absorption peak is also important for the proper design of metamaterial absorbers. This is the reason why an updated RLC circuit model, consisting in a single RLC resonance branch of lumped circuit elements as functions of width, length, and dielectric spacing, has been developed to predict not only the resonance frequency but also the Full Width at Half Maximum ($FWHM$) and the quality factor (Q) [46]. However, the latter model lacks the off-resonance reactance coming from the capacitive coupling between neighboring nanostructures. Therefore, a modified circuit model has been proposed by Kang, which provides an accurate description of the effective surface impedance of the absorbers to be eventually used in the transmission line theory to compute the absorption spectral response of absorption, thereby allowing for the analysis of all absorption characteristics, included the peak wavelength, absorptance, and bandwidth, of a given MIM IR absorber simultaneously [43]. This last model is the one here adopted and it is extensively described in section 3.2.1.

2.3.2 Lateral vibrating piezoelectric MEMS resonator

Historically, the adoption of thin films of piezoelectric materials for manufacturing MEMS followed a relatively bumpy path. Many of the engineers working in the integrated circuit (IC) industry used to label piezoelectric materials as exotic. To add to this perception, many of the materials initially used for piezoelectric MEMS, such as zinc oxide (ZnO) and lead zirconate titanate (PZT), were indeed not compatible with semiconductor-focused manufacturing facilities. The advent of new materials, such as aluminum nitride (AlN), has transformed the space and generated a growing interest in the use of piezoelectric materials for the making of MEMS.

However, piezoelectric thin films are of interest for MEMS devices since the earliest developments in MEMS technology because the piezoelectric effect is an electromechanical effect. In the 1970s and 1980s, the investigated thin film materials were mainly ZnO and AlN and, in the 1990s, PZT was added to the list for having a stronger piezoelectric material for actuators. In particular, for higher-frequency applications as pass-band filters for telecommunication in the GHz frequency range, the two wurtzite structures of AlN and ZnO remained the best solution, simply because they exhibit much higher mechanical quality factors than PZT, and they are much more easily grown in thin film form in comparison to lithium niobate ($LiNbO_3$). Moreover, integration and process compatibility with the rest of the device are less difficult using the relatively simple wurtzite materials. In addition, the strong polarity of their crystalline structure allows for a polar growth and a stable piezoelectric response with time, whereas ferroelectrics always risk depoling.

Nowadays, among the two aforementioned wurtzite crystals, AlN is the elective material for practically all radio frequency (RF) devices based on piezoelectric thin films, even if its maximum piezoelectric coefficient is slightly lower than that of ZnO. Here are explained the two main reasons for this choice:

1. the deposition process of AlN thin films appears to be very well reproducible and it is CMOS compatible, in contrast to PZT and ZnO. In fact, reactive magnetron sputtering enables deposition at rather moderate temperatures below 400° of high-quality thin films with thickness from 10 nm to several μm, making the process post-CMOS compatible and so allowing integration on silicon substrates, which means also large-scale manufacturing in modern lines;
2. AlN exhibits a high thermal conductivity for an electrically insulating material.

In particular, AlN grows in the wurtzite structure that allows for piezoelectricity and pyroelectricity, but not ferroelectricity. Moreover, like many nitrides, AlN is a very chemically stable material with excellent acoustic properties such as high hardness, low loss, and large stiffness constants. In fact, it is a hard material with light atoms and exhibits a high mechanical quality up to very large microwave frequencies together with a relatively large Poisson ratio. The relative dielectric constant of thin films amounts to typically 10–11 and a rather specific feature of AlN is its high sound velocity. Future applications may also include devices operated at high temperatures because AlN exhibits a very high melting point of 2470 K and a quite a large bandgap of 6.1 eV at room temperature so that it is a good dielectric material up to high temperatures [47].

In conclusion, AlN offers some unique advantages compared with other piezoelectric materials: high-quality thin films of various thicknesses can be easily deposited on a silicon substrate by low-temperature sputtering process showing very reproducible properties with high quality factor Q and intermediate values of electromechanical coupling k_t^2. Furthermore, this deposition process enables the staking of multiple AlN and electrode layers which can be properly configured to efficiently transduce the desired mode of vibration of the structure and simultaneously achieve the optimum input and output impedance values. For these reasons, AlN has been often considered as a preferred material for the fabrication of purely piezoelectric laterally vibrating resonators.

Some years ago, $ScAlN$ was discovered as a stronger piezoelectric material than AlN and looks very promising [48]. In fact, since Sc is a strictly 3-valent cation like Al, Al substitution by Sc in the wurtzite phase of AlN is possible and it allows for an increase of the piezoelectric response due to mainly two reasons:

1. Sc atoms are larger than Al ones. In fact, Al^{3+} (32 pm) has most likely a tetrahedral coordination with N, while Sc^{3+} is in general not found in tetrahedral coordination because its radius is too large (88.5 pm) and so the natural ScN structure is the rock-salt, i.e. sodium chloride, ($NaCl$) structure with octahedral coordination. This means that Sc in AlN spreads the N tetrahedron to find more space, leading to a distortion of the unit cell;
2. Sc atoms are less electronegative than Al ones so that their bonds have a larger ionic nature.

This material is progressively being integrated into mass-produced products such as acoustic filters for RF front-ends [49]. Moreover, in addition to its higher coupling, Sc-doping of AlN films has been found to exhibit a significantly higher temperature coefficient of frequency (TCF). While this property is commonly deemed undesirable in filtering applications, where SiO_2 is frequently employed as a thermal compensation layer in acoustic resonators owing to its positive TCF (one of the few materials that exhibit this characteristic) [50], it can be advantageous in resonant thermal IR-sensing applications like the one described in this thesis, where larger changes in acoustic properties from temperature fluctuations can enhance system sensitivity. This is the reason why $ScAlN$ has been selected as a piezoelectric material for the fabrication of the LVR on which the proposed IR detector is based.

In general, micro and nano-electromechanical piezoelectric resonators have been used successfully as ultra-sensitive detectors for sensing mass, fluids flow, and specific chemical or biological agents, but the fundamental advantage of MEMS/NEMS resonant sensors over other existing sensor technologies is related to the unique combination of extremely high sensitivity to external perturbations (due to their very reduces dimensions) and ultra-low noise performance (due to the intrinsically high quality factor of such resonant systems). Among them, LVRs belong to this category and represent one of the most suitable technologies to devise high-performance resonant sensors.

Being a resonator, LVRs are formed either entirely by a thin piezoelectric film sandwiched between metallic electrodes or by a composite constituted by the same piezoelectric film stacked on top of another structural layer such as semiconducting or insulating material. However, the substantial difference between laterally vibrating piezoelectric resonant sensors and the other MEMS/NEMS resonant sensors technologies is that the sensitivity of a laterally vibrating resonator to the particular external perturbation of interest can be set independently of its vibration frequency. In fact, differently from more conventional piezoelectric resonant sensors, whose sensitivity per unit area and operating frequency are highly dependent on the thickness of the structure, in a laterally vibrating resonant sensor the sensitivity per unit area can be adjusted by varying the thickness of the piezoelectric layer without any significant effect on the chosen optimal operating frequency of the device. This is an important and unique feature that offers a further degree of flexibility in the sensor design when its operation is constrained to a particular frequency that is dictated by the application requirements such as in wireless or radio frequency identification components. Furthermore, attaining high sensitivity at a low frequency translates into the use of lower power electronic readout circuits than what is possible with other devices, which require operating at approximately two orders of magnitude higher frequencies in order to achieve the same levels of sensitivity. In fact, the power consumption of the CMOS circuitry used as readout typically increases with the square of the operating frequency. In conclusion, for laterally vibrating resonators, once the desired frequency of operation has been set, the performance of the sensor can be improved by reducing the thickness of the piezoelectric layer up to the limit for which a high Q is preserved. Thanks to these unique features, LVRs can address some of the most important challenges in the areas of physical, chemical, and biological detection and can be simultaneously used to synthesize high-Q multifrequency RF resonant devices. In fact, piezoelectric LVRs have also shown great potential for the development of high-resolution and low-power chemical physical and biological sensors.

Combining the aforementioned features of AlN as novel piezoelectric material and LVRs as highly performing devices, the AlN Nano-Plate Resonator (NPR) technology has been successfully used for the implementation of multiple high-performance physical, chemical, and biological sensors. Recently, the extraordinary transduction properties of this technology have also been combined with the unique physical, optical, and electrical properties of advanced materials such as graphene, photonic metamaterials, and magnetic materials, to devise laterally vibrating resonant sensors with unprecedented sensitivity to infrared radiation and magnetic field. In particular, the combination of nanoplasmonic and piezoelectric resonances enabled the simultaneous achievement of efficient transduction, high-quality factor, low detection limit, and strong, polarization-independent and spectrally selective absorption of infrared radiation, addressing all fundamental challenges associated with the development of performing resonant IR detectors which could potentially lead to a new paradigm for high-performance, miniaturized, power-efficient IR spectroscopy and multispectral imaging systems. Moreover, replacing AlN thin films with $ScAlN$ ones will lead to further improvement.

2.4 Read-out circuit

The read-out circuit is based on the detection of the frequency of oscillation of a signal, which has to be somehow related to the temperature-sensitive resonance frequency of the resonant body.

First of all, in general, in order to realize oscillations, the following elements are strictly required:

1. an active element producing amplification;
2. a positive feedback;
3. a frequency selective network to determine the oscillation frequency;
4. a nonlinearity to maintain the oscillation amplitude in stable equilibrium.

Therefore, a harmonic oscillator in its basic form consists of an electronic amplifier connected to a feedback loop with its output fed back into its input through a frequency-selective filter to provide positive feedback. In this way, when the amplifier is switched on, its output consists only of noise, which travels around the loop and is progressively filtered and re-amplified until it resembles a sine wave at a single frequency.

The oscillators can be classified according to the type of frequency-selective filter used in the feedback loop:

- *RC oscillators*, where the filtering element is a network of resistors and capacitors. Common types of RC oscillator circuits are the phase shift oscillator and the Wien bridge oscillator;
- *LC oscillators*, where the filtering element is a tank circuit consisting of an inductor and a capacitor connected together. Typical LC oscillator circuits are the Hartley, Colpitts, and Clapp circuits;
- *crystal oscillators*, where the frequency selective element in the feedback network is a piezoelectric crystal acting as a resonator whose resonance frequency determines the output frequency of the oscillation. Quartz crystals are commonly used to cover frequencies up to a few hundred MHz, but also piezoelectric resonators allow to achieve much higher operating frequencies up to a few GHz, have a small form factor, and can be fully integrated with CMOS IC [51]. In general, piezoelectric crystals have a higher quality factor and also better temperature stability, thereby allowing them to achieve much better frequency stability than LC or RC oscillators. Crystal oscillators often use the

same circuits as LC ones by simply replacing the tank circuit with the piezoelectric crystal. The typical crystal oscillator circuit is the Pierce oscillator.

Significant advancements have been made in the development of MEMS resonator technologies based on both electrostatic and piezoelectric transduction mechanisms for use in reference oscillator applications [52]. Notably, the AlN contour-mode RF MEMS technology is distinctive [53], as it can be considered as the MEMS counterpart of quartz crystal Bulk Acoustic Wave (BAW) resonators and it is the only technology that can consistently cover a broad frequency spectrum from 10 MHz to several GHz. At the same time, it provides a high quality factor in the air and a low motional resistance, eliminating the requirement for special circuit design or complex matching networks, thus allowing for straightforward integration with traditional electronics.

Due to its excellent performance in terms of stability and reliability [54], the elective oscillator for this kind of application turns out to be a Pierce oscillator, i.e. a circuit that uses a piezoelectric crystal (in this case a $ScAlN$ LVR) as a frequency-selective element in its passive feedback network. In particular, the problem arising from using a real inductor in the Pierce oscillator is related to its relatively low quality factor. Therefore, it is typically substituted by a high-quality factor piezoelectric resonator, which satisfies the Barkhausen criterion just in the narrow spectral range between the series and parallel resonance frequencies. Moreover, using a MEMS resonator whose resonance frequency is sensitive to temperature changes, a detection mechanism is built.

In fact, a change in the resonance frequency of a resonator is typically monitored by an oscillator-based interface. In particular, an example of a low-power sensor interface IC suitable for a differential frequency measurement application was already demonstrated by [55], where it was used in a thin Film Bulk Acoustic wave Resonator (FBAR)-based mass or pressure sensor system that integrates two matched Pierce oscillator structures with two separate resonators (the actual sensor and a reference FBAR) in close proximity and uses one of them as a reference to track the resonance frequency change due to unwanted variables like temperature, humidity, package stress, and aging in order to cancel out any unwanted resonance frequency drift to first order. In this way, a differential input resulting from a sensor variable (mass or pressure) change affects only the sensor oscillator and changes the output, which directly provides the sensor response since the close proximity of the sensor FBAR with the reference one makes them experience the same resonance frequency drift due to the aforementioned unwanted variables. In this thesis, a similar approach is followed and described in section 3.3.

Chapter 3

System architecture and model

This section is aimed to extensively describe the operating principles of the system and its sub-parts from a theoretical standpoint. In particular, the system is composed of three main parts:

1. Optics: a custom QCL to target the optimal wavelength needed to detect N_2O molecules and a Herriott multipass cell [56] [57] [30] [58]. In general, LAS quantifies the concentration of analytes by exploiting the absorption due to the characteristic resonant mode of vibration of a target gas at a specific IR wavelength, which results in a reduced IR laser power delivered to an IR sensor after passing through a gas cell. Moreover, as the method primarily relies on the intrinsic IR absorption of a gas sample, in order to achieve a high sensor detection sensitivity, the system requires a gas cell to allow for a long optical path length. Here, a Herriott-type optical cell is exploited and optimized to minimize the gas cell volume without compromising the effective optical path length. Therefore, the IR power delivered by the QCL to the MEMS-based IR detector is attenuated as the IR beam passes through the long-path optical cell and gets absorbed by the gas-specific characteristic IR absorption. The reduction in the available IR power can be detected by the MEMS-based IR detector and translated into a corresponding concentration level of a target gas;

2. MEMS: plasmonic metamaterial absorbers integrated on top of a piezoelectric LVR [43] [44] [24] [59]. In particular, a $ScAlN$ resonator covered by near-perfect nano-plasmonic metamaterial narrowband absorbers suitable for ultra-low noise and fast spectroscopic IR sensing is used in order to exploit its volume scaling (ensuring reduced thermal capacitance), excellent thermal isolation (translating into a high thermal resistance), and the use of frequency shift as the output parameter (guaranteeing high measurement accuracy) for the fast and high-resolution thermal sensing performance. Its unique advantage of compatibility with CMOS fabrication for on-chip frequency read-out will be eventually exploited for the development of a complete chip-level sensor-IC integration. In fact, the low-temperature sputtering process used for the deposition of ultra-high quality $ScAlN$ thin films on an arbitrary substrate indicates that the technology can be realized post-CMOS process, allowing for the seamless MEMS-CMOS integration;

3. Read-out circuitry: integrated circuit properly designed to perform the read-out of the shift in resonance frequency of the resonator covered by plasmonic metamaterial absorbers, where a pair of independent oscillators is used for differential reading. In particular, the frequency shift differential read-out is carried out using as a reference oscillator a $ScAlN$ resonator identical to the IR detector, but covered with an IR-reflective coating instead of the plasmonic metamaterial absorber;

Furthermore, monolithically integrated and properly characterized in-situ commercial off-the-shelf (COTS) temperature, humidity, and CO_2 sensors are also included in order to compensate for any inherent frequency drift of the detector in response to any change of:

- concentration of molecules whose absorption spectrum partially overlaps with the N_2O one, like CO_2 and CO, thereby interfering with the measurement since the power of the IR beam is partially modulated also by them;
- humidity conditions, since also the absorption spectrum of H_2O molecules partially overlap with the N_2O one;
- ambient temperature, since the absorption spectrum of each molecule in the atmosphere is sensitive on both the temperature and pressure conditions. In particular, since the sensor will eventually operate at the typical altitudes of drones' flight, where the air pressure they experience does not distance itself from the one at the sea level, the pressure fluctuations from the atmospheric one, i.e. 1 atm at the sea level, are considered negligible, while temperature fluctuations can be significant, especially if the sensor operates over a long period of time or during different seasons, and so their assessment necessary. Moreover, due to the inherent characteristics of the resonant thermal detector, there exists an output error related to the intrinsic shift in resonance frequency due to a change in ambient temperature according to the TCF of the resonant body.

Such errors will be eventually mitigated by compensation, i.e. using the measurement of the integrated COTS sensor to offset the output signal from the MEMS IR detector.

3.1 Optics: gas cell

3.1.1 Beer-Lambert's Law

The absorption of just specific bands of the IR radiation spectrum by molecules depends on their constituent bonds that have characteristic resonant modes of vibration at different wavelengths. Therefore, when the IR radiation wavelength matches the one related to the resonant mode of vibration of a certain bond of the molecule, the electromagnetic energy gets coupled to the vibrational resonant mode of the bond, resulting in a reduced IR power exiting the sample. In particular, the ratio of IR power entering the sample with the exiting one, i.e. the *transmittance* T, is governed by the Beer-Lambert's Law:

$$T = \frac{P_{out}}{P_{in}} = 10^{-A}, \tag{3.1}$$

where P_{in} and P_{out} is the *IR radiation power* (W) entering and exiting the sample, respectively, while:

$$A = l \sum_i \varepsilon_i c_i \tag{3.2}$$

is the so-called *absorbance*, where l is the *optical path length* (cm), c_i the *molar concentration* (mol/cm^3) and ϵ_i the *molar absorption cross-section* (cm^2/mol) of the i-th molecule contained inside the sample.

As a consequence, for a certain molecule (i.e. a fixed *molar concentration* ϵ_i at a specific IR radiation wavelength) and *optical path length* l, the *molar concentration* c_i of that specific molecule can be determined by measuring the IR radiation power transmitted through the sample. This is achieved through an $ScAlN$ resonant IR detector with a narrowband plasmonic metamaterial IR absorber integrated on top of it whose absorption wavelength is specifically designed to match the chemical bond's resonance wavelength of the target molecule.

3.1.2 Mirrors

The elective approach implemented to obtain high detection sensitivity is to increase the *optical path length* l covered by the IR laser beam while interacting with the gas sample by using a commercial or custom MPC, which is constructed with two facing highly reflective mirrors. However, the traditional Herriott cell [30], which is based on two spherical mirrors, yields a standard low-density circular or elliptical spot pattern with a low utilization efficiency of the mirror surfaces that makes difficult to achieve long *optical path length* l in a small form factor to realize compact sensor systems. Many variants based on the Herriott cell, such as astigmatic mirror cells, can produce dense spot patterns to take better advantage of the entire mirror surfaces, thereby realizing a compact size sensor with a long *optical path length* l. However, the manufacturing of aspheric surfaces is more complex. Moreover, it is difficult to produce a mirror of sufficient surface accuracy to follow the designed curvature. Therefore, spherical mirrors are usually required in MPCs because of their low requirements for mirror processing technology, more easily controlled surface quality, and, more importantly, lower cost [60].

Conventional calculations of a two-identical-spherical-mirrors MPC, such as a Herriott cell, are based on a standard ABCD matrix within the paraxial approximation of a thin lens, which models the one pass count as the product between a standard transmission matrix describing a ray propagating through the free-space and a standard reflection matrix describing a ray reflecting off a concave spherical mirror:

$$\begin{bmatrix} A & B \\ C & D \end{bmatrix} = \begin{bmatrix} 1 & 0 \\ -2/R & 1 \end{bmatrix} \cdot \begin{bmatrix} 1 & d \\ 0 & 1 \end{bmatrix}, \tag{3.3}$$

where R is the *curvature radius* of the spherical mirrors and d their *spacing* since all the rays are supposed to make small angles to the optical axial of the system so that the optical path lengths of any rays between two mirrors are constantly equal to the mirror spacing d. Therefore, describing a ray propagating between the two mirrors as a column vector containing the coordinate x (or y) and the inclination angle θ_x or θ_y, the ray characteristics at each pass count n can be retrieved from those of the one at the $(n-1)$-th as follows:

$$\begin{gathered} \begin{bmatrix} x_n \\ \theta_{n_x} \end{bmatrix} = \begin{bmatrix} A & B \\ C & D \end{bmatrix} \cdot \begin{bmatrix} x_{n-1} \\ \theta_{n-1_x} \end{bmatrix} \\ \begin{bmatrix} y_n \\ \theta_{n_y} \end{bmatrix} = \begin{bmatrix} A & B \\ C & D \end{bmatrix} \cdot \begin{bmatrix} y_{n-1} \\ \theta_{n-1_y} \end{bmatrix}. \end{gathered} \tag{3.4}$$

However, with a more highly curved surface of the reflective mirrors and more pass counts in the MPCs, the conventional ray calculations based on a standard ABCD matrix, specifically marginal rays, generate deviations from the actual trajectories on account of spherical mirror aberrations. These deviations accumulate and are amplified, ultimately distorting the real spot pattern. In fact, these intrinsic aberrations can be effectively exploited to produce a set of intricate variants with respect to a Herriott circular or elliptical spot pattern, which can be completed by manipulating these parameters, such as the mirror spacing d, the initial entry location (x_0, y_0), and the incident angle of the ray $(\theta_{0_x}, \theta_{0_y})$. Therefore, in order to take into account the spherical mirror aberrations, a modified ABCD matrix describing the one-pass count of both the paraxial and marginal rays without the paraxial approximation of a thin lens can be expressed as follows:

$$\begin{bmatrix} A & B \\ C & D \end{bmatrix} = \begin{bmatrix} 1 & 0 \\ L & 1 \end{bmatrix} \cdot \begin{bmatrix} 1 & d_n S \\ 0 & 1 \end{bmatrix}, \tag{3.5}$$

where d_n is the optical path length for the n-th transmission between two spherical mirrors, and L and S represent two operators introduced in order to remove the paraxial approximation, which are defined as $L\phi = -2arcsin(\phi/R)$ and $S\phi = sin\phi$, respectively. Here, ϕ is an arbitrary rational number. Therefore, the new ABCD matrix consists of a modified transmission matrix and a modified reflection matrix. With an incident ray of a specific initial location (x_0, y_0) and incident angle $(\theta_{0_x}, \theta_{0_y})$, the spot coordinates (x_n, y_n) on the spherical mirror surfaces and the ray trajectories between them expressed as inclination angles $(\theta_{n_x}, \theta_{n_y})$ at each pass count n can be exactly traced knowing their values at the $n-1$-th pass count, thereby using an iterative algorithm described as follows according to the modified ABCD matrix:

$$\begin{cases} x_n = x_{n-1} + d_n \cdot sin(\theta_{n-1_x}) \\ \theta_{n_x} = -2 \cdot arcsin(\frac{x_n}{r}) + \theta_{n-1_x} \end{cases} \quad \begin{cases} y_n = y_{n-1} + d_n \cdot sin(\theta_{n-1_y}) \\ \theta_{n_y} = -2 \cdot arcsin(\frac{y_n}{r}) + \theta_{n-1_y}. \end{cases} \tag{3.6}$$

The above iterative equations can be carried out as long as d_n is obtained at each pass count n as follows:

$$d_n = \frac{z_n - z_{n-1}}{sin(\theta_{n-1_z})}, \tag{3.7}$$

where

$$\begin{cases} z_n = sin^2(\theta_{n-1_z}) \cdot \left[-\frac{b_n}{2} + (-1)^{n-1} \cdot \sqrt{\left(\frac{b_n}{2}\right)^2 - a_n \cdot c_n} \right] \\ \theta_{n_z} = \frac{arcsin\sqrt{1 - sin^2(\theta_{n_x}) - sin^2(\theta_{n_y})}}{(-1)^n} \end{cases} \tag{3.8}$$

with

$$\begin{gathered} a_n = sin^{-2}(\theta_{n-1_z}) \\ b_n = \left[\frac{x_{n-1} \cdot sin(\theta_{n-1_x}) + y_{n-1} \cdot sin(\theta_{n-1_y})}{sin(\theta_{n-1_z})} + \left(1 - \frac{1}{sin^2(\theta_{n-1_z})}\right) \cdot z_{n-1} - \left(\frac{1+(-1)^{n-1}}{2} \cdot D + (-1)^n \cdot r\right) \right] \cdot 2 \\ c_n = \left(x_{n-1} - \frac{sin(\theta_{n-1_x})}{sin(\theta_{n-1_z})} \cdot z_{n-1}\right)^2 + \left(y_{n-1} - \frac{sin(\theta_{n-1_y})}{sin(\theta_{n-1_z})} \cdot z_{n-1}\right)^2 + \left(\frac{1+(-1)^{n-1}}{2} \cdot D + (-1)^n \cdot r\right)^2 - r^2. \end{gathered} \tag{3.9}$$

The initial location z_0 and inclination angle θ_{0_z} with respect to the optical axis can be calculated by using the spherical equation as follows:

$$\begin{gathered} z_0 = r - \sqrt{r^2 - x_0^2 - y_0^2} \\ \theta_{0_z} = arcsin\sqrt{1 - sin^2(\theta_{0_x}) - sin^2(\theta_{0_y})}. \end{gathered} \tag{3.10}$$

3.2 MEMS detector

To model the plasmonic piezoelectric MEMS resonant IR detector, the two-port electrothermal equivalent circuit with both electrical and mechanical inputs shown in Figure 3.1 is utilized. In particular, the circuit comprises of two input sources: the voltage that drives the acoustic resonance, and the infrared power converted into heat by the plasmonic absorbers. At the thermal port, the device is modeled by a shunt between a *thermal capacitance* C_{th} and a *thermal resistance* R_{th}. The value of the *thermal capacitance* is determined by the materials stack specific heat and the total volume of the suspended plate. Conversely, the *thermal resistance* is primarily determined by the thickness and width of the anchors connecting the free-standing resonance body to the substrate, as well as the thermal conductance of the stack. On the other hand, at the electrical port, the device is modeled by the modified Butterworth-Van Dyke (mBVD) equivalent circuit, extensively described in section 3.2.2.

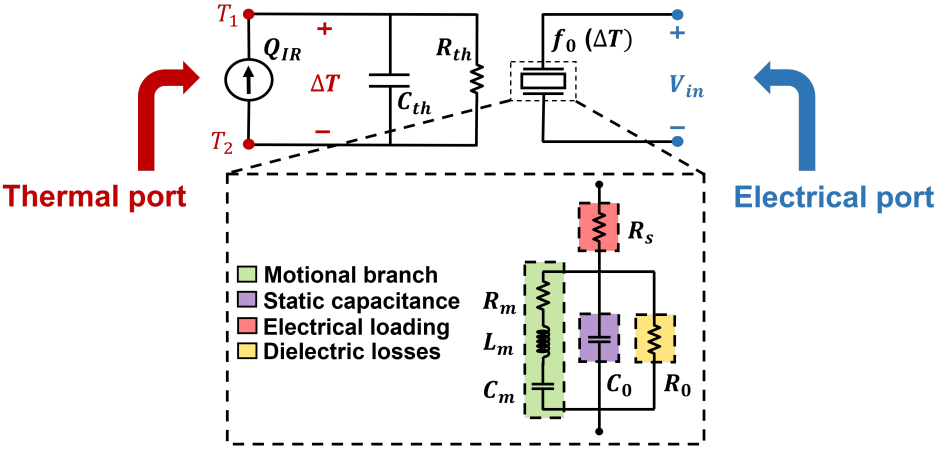

Figure 3.1: Thermo-electric lumped equivalent circuit of the detector and mBVD model of the resonator.

The fraction of power of the IR beam P_{out} impinging the device after exiting the gas cell, where it is subjected to a modulation due to the presence of gas molecules inside the cell according to equation 3.1, is absorbed by the plasmonically enhanced resonant body and converted into heat Q_{IR}, which causes a large and fast increase of the resonant body's temperature ΔT due to the high *thermal resistance* R_{th} and extremely low *thermal capacitance* C_{th} of the freestanding nanomechanical structure, respectively, according to the following equation:

$$\Delta T = \frac{\eta Q_{IR}}{\sqrt{\frac{1}{R_{th}^2} + \omega^2 C_{th}^2}} \approx \frac{\eta Q_{IR}}{\sqrt{\frac{1}{R_{th}^2}}} = \eta R_{th} Q_{IR}, \tag{3.11}$$

where η is the IR *absorption efficiency* of the plasmonic metamaterial absorber. The approximation holds in the case of slowly modulated, i.e low *angular modulation frequency* ω, impinging IR radiation.

From the general definition of the TCF of a resonant plate, stated in equation 3.60 later on, and according to equation 3.11, the downshift Δf in the *acoustic resonance frequency* f_0 of the piezoelectric LVR due to the IR-induced temperature rise ΔT occurring in the resonant body (see Figure 3.2) can be evaluated as follows:

$$\Delta f = f_0 \cdot TCF \cdot \Delta T \approx f_0 \cdot TCF \cdot \eta R_{th} Q_{IR}. \tag{3.12}$$

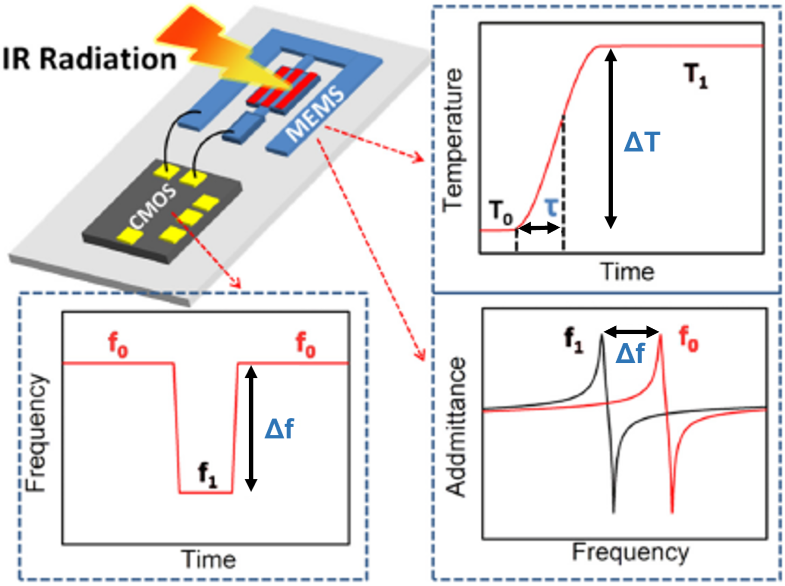

Figure 3.2: Schematic illustration of the working principle of the resonant IR detector based on a MEMS resonator.

In conclusion, as shown in Figure 3.3, a variation of the molar concentration Δc in the gas cell function of the variation of incident optical power can be detected by monitoring the resonance frequency shift Δf of the resonant body, which is one of the physical quantities that can be monitored with the highest accuracy via the readout IC. The latter includes also a frequency-to-voltage conversion module and an analog-to-digital converter to finally obtain a voltage output signal V_{OUT} readable by a micro-controller.

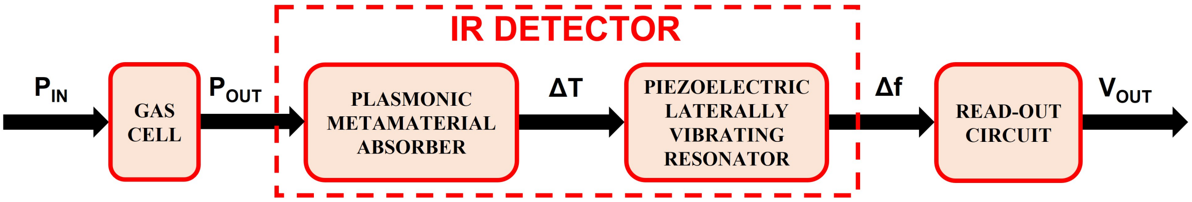

Figure 3.3: High-level schematic illustration of the signal transduction path of the device.

The *responsivity* R of the proposed resonant IR detector is defined as the resonant frequency shift of the device Δf in response to the heating induced by the impinging power of the IR radiation Q_{IR}, and can be expressed as follows in the case of slowly modulated impinging IR radiation:

$$R = \frac{\Delta f}{Q_{IR}} = f_0 \cdot TCF \cdot \eta \cdot R_{th} = \eta \cdot f_0 \cdot S, \tag{3.13}$$

where S (equal to the product between the TCF and the thermal resistance R_{th}) is defined as the *sensitivity* of the sensor, i.e. a measure of how efficiently the heating induced by the impinging power of the IR radiation is converted into a shift of the resonance frequency.

Therefore, the *responsivity* must be maximized in order to obtain the largest possible shift of resonance frequency with the same amount of impinging optical IR power. In particular, a high responsivity can be achieved by maximizing:

- the resonance frequency f_0 by miniaturizing the device as much as possible;
- the temperature coefficient of frequency TCF by properly designing the material stack;
- the absorption efficiency η of the plasmonic absorber at the IR frequency of the impinging wave by properly designing the metasurface;
- the thermal resistance R_{th} by improving the thermal isolation of the resonator from the substrate, i.e. by properly designing the anchors that directly connect the resonant body to the substrate.

A crucial parameter that ought to be considered for the design and optimization of the proposed resonant IR thermal detector is the *noise equivalent power* (NEP), which represents the IR power that gives a signal-to-noise ratio equal to 1 in a 1 Hz measurement bandwidth (minimum detectable IR power) and it is defined as the *noise-induced frequency fluctuation* f_n divided by the *responsivity* R of the detector:

$$NEP = \frac{f_n}{R} = \frac{f_n}{f_0 \cdot TCF \cdot \eta \cdot R_{th}}. \tag{3.14}$$

Among different noise sources, the fundamental limit to frequency stability of a thermal resonant sensor is given by:

1. the thermal fluctuation noise associated with the spontaneous temperature fluctuations of the detector element due to the finite heat conductance G_{th} to the surroundings, which leads to a contribution to the total NEP equal to:

$$NEP_{th} = \frac{2T_0}{\eta}\sqrt{\frac{K_B}{R_{th}}}; \tag{3.15}$$

2. the background fluctuation noise due to radiative heat exchange with the environment, which leads to a contribution to the total NEP equal to:

$$NEP_{rad} = \frac{1}{\eta}\sqrt{16A\epsilon\sigma K_B T_0^5}; \tag{3.16}$$

3. the thermomechanical noise originated from the thermally driven random motion of the mechanical structure, which leads to a contribution to the total NEP that has been identified to be inversely proportional to the quality factor Q of the resonator:

$$NEP_{mec} = \sqrt{\frac{K_B T_0}{4P_c}}\frac{1}{TCF \cdot \eta \cdot R_{th} \cdot Q}; \tag{3.17}$$

where K_B is the *Boltzmann constant*, T_0 is the temperature of the resonant body, A is the area of the device, ϵ is the *emissivity*, σ is the *Stefan-Boltzman constant*, and P_c is the power used to drive the mechanical resonance in the structure. The total NEP can be expressed as:

$$NEP = \sqrt{NEP_{th}^2 + NEP_{rad}^2 + NEP_{mec}^2}. \tag{3.18}$$

Differently from the other two noise sources, the thermomechanical noise originating internally from the MEMS resonator itself is the dominant source of frequency fluctuation. Therefore, the NEP can be minimized not only by maximizing R, as illustrated before, but also by maximizing the quality factor Q, and power handling P_c.

Another crucial parameter to be considered for the design of a high-performance IR thermal detector is its response time which is limited by the *thermal time constant* τ of the device, defined as the product between its *thermal resistance* R_{th} and *thermal capacitance* C_{th}:

$$\tau = R_{th} \cdot C_{th}. \tag{3.19}$$

Therefore, the τ must be minimized in order to obtain the highest possible speed of the sensor while reaching a stable temperature. In particular, a low thermal time constant can be achieved by minimizing both R_{th} and C_{th}.

However, equation (3.14) indicates that by increasing R_{th} the NEP of the device is reduced, while on the other hand equation (3.19) indicates that its *response time* is increased. Therefore, a trade-off between these two important performance metrics needs to be generally considered for the design of the detector and, in particular, a common *figure of merit* (FoM) that is considered for such a kind of device is the product between the NEP and the *response time*:

$$FoM = NEP \cdot \tau \simeq NEP_{mec} \cdot \tau = \sqrt{\frac{K_B T_0}{4P_c}} \frac{C_{th}}{TCF \cdot \eta \cdot Q}. \tag{3.20}$$

Therefore, this FoM is independent of the *thermal resistance* R_{th} and the device should be designed to have its FoM as small as possible. Nevertheless, for a given *thermal resistance* R_{th} guaranteeing a satisfactory NEP, the *response time* of the sensor can be reduced by minimizing its *thermal capacitance* C_{th}, which directly translates into reducing the volume of the resonant structure through its miniaturization because:

$$C_{th} = c_{eq} \cdot \rho_{eq} \cdot V = c_{eq} \cdot \rho_{eq} \cdot A \cdot t, \tag{3.21}$$

where c_{eq} and ρ_{eq} are the equivalent *specific heat capacity* and *density* of the device, respectively, while V is its volume (equal to the product between the area A of the device and the total thickness t of the material stack forming the resonator). Although the device lateral dimensions can in principle be lithographically scaled, a reduction in device area directly causes a considerable decrease in the device *static electrical capacitance* C_0, which is proportional to the device area and inversely proportional to the device thickness if the resonator is simplified to a parallel plate capacitor:

$$C_0 = \frac{\epsilon \cdot A}{t}, \tag{3.22}$$

where ϵ is the permittivity of $ScAlN$. When the device capacitance falls below the substrate parasitic capacitance, the effective electromechanical coupling of the resonant element can be heavily deteriorated (higher electrical impedance and insertion loss) [61]. Therefore, in order to maintain a reasonably high C_0, the three dimensions of the device need to be scaled proportionally.

In conclusion, if a minimum C_0 that needs to be maintained to ensure a high electromechanical coupling and ease electronic readout is set, the equations 3.20, 3.21, and 3.22 lead to:

$$FoM \propto \frac{C_0 \cdot t^2}{TCF \cdot \eta \cdot Q}. \tag{3.23}$$

This last equation indicates that the scaling of the device thickness, while maintaining the resonator static electrical capacitance constant to a value larger than the substrate parasitic capacitance, inevitably yields a greatly improved IR detector figure of merit. Moreover, it is worth mentioning again that the absence of thermal resistance suggests that it can be freely tailored (by altering the anchor design of the resonant IR detector) to fit the requirements of detector resolution or speed of specific applications without affecting the figure of merit.

Current state-of-the-art devices have already demonstrated ultrafast (*thermal time constant* $\tau \sim 166$ μs) and high resolution (*noise equivalent power* NEP ~ 549 $pW/Hz^{1/2}$) thermal detectors based on high-quality factor 50 nm-thick AlN piezoelectric resonant nanoplates [62], so that an over doubled FoM is achieved if compared to the previous devices with thicker AlN.

In this work, the core element of the proposed IR thermal detector is an LVR (see Figure 3.4). The resonant body is composed of a 350 nm-thick 30%-doped $ScAlN$ piezoelectric layer sandwiched by a 100 nm-thick bottom Pt interdigitated electrode (IDE, used to excite a lateral-extensional vibrational mode when an AC current signal with the same frequency of the natural resonance frequency of the resonator is applied) and a 100 nm-thick top Al floating plate (used to confine and route the electric field in the piezoelectric layer across its thickness and so increase the electromechanical coupling by exploiting the high e_{31} piezoelectric coefficient). Therefore, since the structure is suspended and supported by two anchors to allow it to vibrate freely, given the *sound velocity* v_0 of the material stack, i.e. the *equivalent Young's modulus* E_{eq} and *equivalent mass density* ρ_{eq} of the $ScAlN$-metal electrodes stack that forms the resonator, the mechanical resonance frequency f_0 is primarily set by the *pitch* W_0 of the IDE:

$$f_0 = \frac{1}{2W_0} v_0 = \frac{1}{2W_0} \sqrt{\frac{E_{eq}}{\rho_{eq}}}. \tag{3.24}$$

In this way a further degree of freedom is gained due to the dependence of the resonance frequency not on the geometry of the resonator itself, but just on the lithographically definable pitch size of the IDE.

Since the pitch size of the IDE is fixed to be 19 μm, the resonance frequency is ~ 160 MHz. Therefore, when an alternating current (AC) signal is applied to the bottom 100 nm-thick Pt IDE of the device and its frequency coincides with the natural resonance frequency f_0 of the resonator, the top electrically floating 100 nm-thick Al electrode acts to confine the electric field across the device thickness and a high order contour-extensional mode of vibration is excited in the 350 nm-thick $ScAlN$ nanoplate through the equivalent e_{31} piezoelectric coefficient.

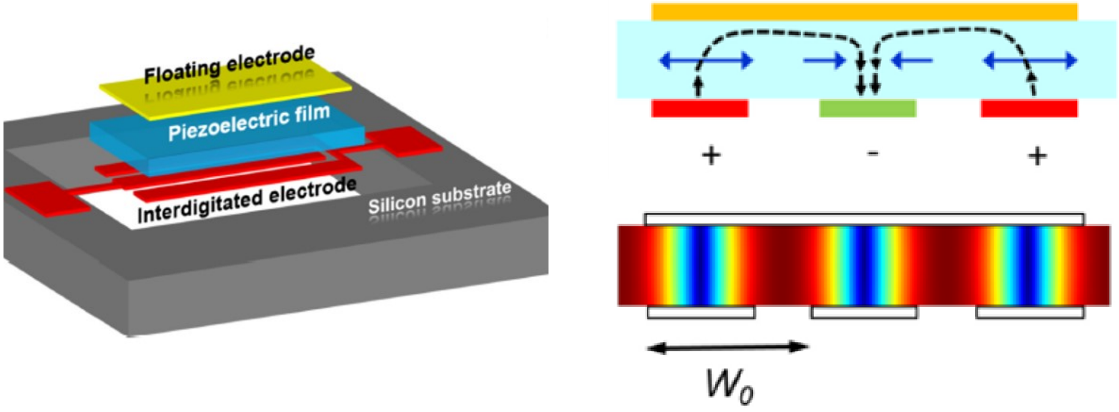

(a) 3-dimensional representation in layer view with bottom inter-digitated electrode and top floating electrode.

(b) Cross-sectional view of the device showing the lateral field excitation on top (the black dash lines represent the electric field and the blue arrows represent the strain induced by the e_{31} piezoelectric coefficient) and the 2D FEM simulation of the lateral-extensional mode of vibration on the bottom (the red and blue colors indicate the locations of maximum and minimum mechanical displacement, respectively).

Figure 3.4: Schematic illustration of an LVR.

3.2.1 Plasmonic absorber

The adopted technology is based on a stack which, going from the bottom to the top, consists in:

1. a continuous and optically thick ground metal layer acting as reflector;
2. a subwavelength thickness dielectric spacer where the impinging field is confined;
3. an array of cross-type plasmonic metal nanostructures whose geometrical parameters select the targeted wavelength at which the absorption has to be maximized.

When the transmitted electromagnetic waves in a specific spectral band impinge on the absorber, both the electric and magnetic dipole resonances are excited in the array of top metal nanostructures, inducing an image current in the ground layer via plasmonic coupling in the subwavelength dielectric gap so that a loop due to a pair of plasmonically-coupled anti-parallel currents is formed between the metasurface and the ground plane acting as a reflector. This current loop gives rise to a strong and efficient confinement of both impinging electric and magnetic fields and, if the right level of intrinsic material Ohmic loss is present to support critical coupling and conjugate matching, i.e. the effective surface impedance of the MIM IR absorber matches the impedance of free space, a near-unity and narrowband absorption at the designed spectral band range is achieved so that the fraction of energy of the incident electromagnetic wave in that particular spectral range is efficiently absorbed and turns into heat.

In order to design and optimize the geometry of the plasmonic absorber without the need of time-consuming numerical computations, a resistor-inductor-capacitor (RLC) lumped equivalent circuit model is exploited. It describes the magnetic resonances, i.e. magnetic polaritons (MPs), inside the metamaterial nanostructures and the associated less (both Ohmic and dielectric losses), allowing the prediction of not only the resonance frequency f_{peak} but also the bandwidth, i.e. the full width at half maximum $FWHM$ of the absorption peak for various geometric patterns. In fact, absorption characteristics of metamaterials strongly depend on the geometric shape and size of the nanostructures and this is the reason why the lumped circuit elements are defined as a function of their geometrical parameters and layers' thickness and material properties.

In particular, this RLC lumped element equivalent circuit allows the modeling of the *effective surface impedance* of the MIM structure $Z_{surface}$ to be used in the equivalent transmission line circuit in order to evaluate the absorption spectral response through simple impedance matching theory, i.e. to predict the condition for critical coupling and conjugate impedance matching that leads to a strong absorption (see Figure 3.5). It consists of the series between:

- the periodic capacitance C_P, which contributes to the electric dipole resonance and the out-of-resonance impedance level. It originates from the capacitive coupling between neighboring cross-shaped nanostructures due to the air gap between them and is approximated by the capacitance between two neighboring wires as follows:

$$C_P = \pi\epsilon_0 \frac{a}{ln\left[\frac{2(\Lambda-b)}{t_c} + \sqrt{\left(\frac{2(\Lambda-b)}{t_c}\right)^2 - 1}\right]}; \tag{3.25}$$

- the RLC circuit branch, which models the magnetic dipole resonance by describing the near-field coupling of localized plasmons and current loop. It consists of a pair of:
  - mutual inductances L_m, which is originated from the magnetic energy stored in the dielectric spacer and equal in both branches to:

$$L_m = \frac{1}{2}\mu_0 \frac{t_d b}{a}; \tag{3.26}$$

  - gap capacitances C_m, which is due to the dielectric spacer separating the top metal structure from the ground plate that serves as a capacitor on each side and expressed as a parallel-plate capacitance:

$$C_m = c\frac{1}{2}\epsilon_0\epsilon_d \frac{ba}{t_d}, \tag{3.27}$$

    where c is a constant appropriately chosen to take into consideration the fringe effect of the capacitance and non-uniform electric field distribution along the surfaces of the capacitor;
  - kinetic inductances L_k, which arise from the imaginary part of the top and bottom metallic layers and model the phase delay in high-frequency current flow, originated from the finite kinetic energy of the electrons inside the metal due to their finite inertia. The kinetic inductance of the bottom continuous ground plane L_{k_g} is different from the one of the top cross-shaped nanostructures L_{k_c} because of the different field (and so current) distribution due to the different electrons confinement:

$$L_{k_c} = \frac{b'}{a\delta_c}\frac{1}{\omega_{p_c}^2\epsilon_0} \tag{3.28}$$

$$L_{k_g} = \frac{b}{a'\delta_g}\frac{1}{\omega_{p_g}^2\epsilon_0}, \tag{3.29}$$

where ω_{p_c} and ω_{p_g} are the *plasma frequencies* of the top and bottom metals, respectively, while δ_c and δ_g are the *penetration depths* of the top and bottom metals, respectively:

$$\delta_{c,g} = \frac{\lambda}{2\pi\kappa_{c,g}(\lambda)}, \tag{3.30}$$

where λ and $\kappa_{c,g}(\lambda)$ are the *wavelength in free space* and the *extinction coefficient.*

- resistances, which arise from the real part of the top and bottom metallic layers. Also in this case, the resistance of the bottom continuous ground plane R_g is different from the one of the top cross-shaped nanostructures R_c because of the different field (and so current) distribution due to the different electrons confinement:

$$R_c = \frac{c'b}{a\delta_c}\frac{1}{\sigma_c} \tag{3.31}$$

$$R_g = \frac{b}{a'\delta_g}\frac{1}{\sigma_g}, \tag{3.32}$$

where $c' = 1 - c$ is a correction factor related to both the fringing effect and the non-uniform electric field distribution, while σ_c and σ_g are the *plasma frequencies* of the top and bottom metals, respectively:

$$\sigma_{c,g} = \epsilon_0\omega_{p_{c,g}}\tau_{c,g}, \tag{3.33}$$

where $\tau_{c,g}$ is the relaxation time.

In all the aforementioned formulas, ϵ_0 and μ_0 are the permittivity and permeability of free space, respectively, while ϵ_d is the relative permittivity of the dielectric spacer. Moreover, all lumped circuit elements are expressed in terms of geometric variables a (width of the cross-type nanostructure) and a' (effective width of the cross-type nanostructure approximately equal to half the length $0.5b$), b (length of the cross-type nanostructure) and b' (effective length of the cross-type nanostructure equal to $c'b$ and so smaller than the designed length due to the uneven current distribution), Λ (periodicity of the cross-type nanostructures), $t_{c,g}$ (thickness of the top and bottom metal layers, respectively) and t_d (thickness of the dielectric spacer).

Based on a conventional transmission-line model used to describe the interaction of the metasurface with the impinging wave, the *absorption efficiency* η is evaluated as follows:

$$\eta = 1 - R_{in} = 1 - |\Gamma_{in}|^2 = 1 - \left|\frac{Z_{surface} - Z_0}{Z_{surface} + Z_0}\right|^2, \tag{3.34}$$

where Z_0 is the impedance of free space, i.e. 377 Ω. Therefore, when the value of $Z_{surface} = R_{surface} + jX_{surface}$ is close to Z_0, i.e. the real and imaginary parts of $Z_{surface}$ are close to 377 Ω and 0 Ω, respectively, the reflectance R_{in} approaches zero, leading to near-unity absorption. In fact, the conjugate impedance matching condition is obtained when the total resistance $R_{surface}$ is equal to 377 Ω, while the resonance condition can be obtained by zeroing the total reactance $X_{surface}$.

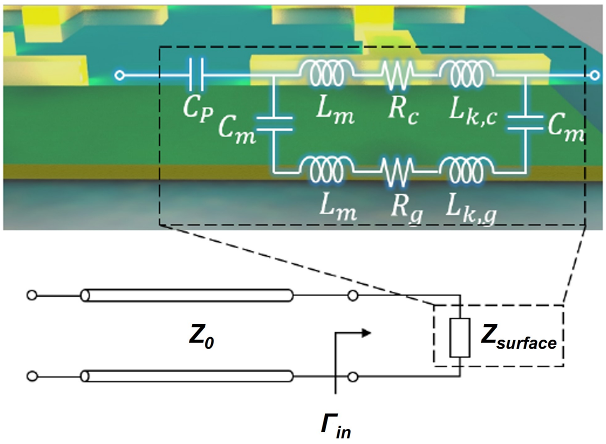

Figure 3.5: Lumped equivalent circuit model and transmission-line model for MIM IR absorbers.

In the end, this RLC lumped element equivalent circuit model allows to express the $FWHM$ and the f_{peak} in terms of geometric parameters as follows:

$$f_{peak} \propto \frac{1}{b} \tag{3.35}$$

$$FWHM \propto \frac{a}{ln(\Lambda)}. \tag{3.36}$$

Equation (3.36) indicates that one can achieve narrow bandwidth by:

- maximizing the periodicity Λ while reducing the width a. However, the upper limit of Λ is set by the wavelength of operation because:

  $$\Lambda_{max} = \frac{\lambda_{peak}}{1 + sin\theta}, \tag{3.37}$$

  where $0^\circ < \theta < 90^\circ$ is the angle of incidence. For Λ exceeding this limit, diffraction occurs and the RLC lumped element equivalent circuit model is no longer valid. Moreover, this limit is more stringent, i.e. smaller Λ_{max}, at oblique incidence, i.e. $\theta > 0$, making the device more susceptible to diffraction.

- reducing the width a up to the point when the absorption starts to decrease due to impedance mismatch because $Z_{surface} >> Z_0$ with smaller a, which sets the limit of scaling for a.

On the other hand, equation (3.35) indicates that the position of the peak can be independently tuned by changing the length b. Therefore, for a given f_{peak}, an optimal set of Λ and a which guarantees a narrow $FWHM$ and a near-unity η exists.

In this work, the proposed plasmonic absorber is formed by 90 nm-thick periodically spaced squared-shaped Au patches, sitting through a 10 nm-thick Ti adhesion layer on top of a 250 nm-thick AlN layer placed on top of a 100 nm-thick Al continuous plate. As a matter of fact, SiO_2 is conventionally used as the dielectric layer, but other materials were investigated and AlN was finally chosen instead, since SiO_2 has a positive TCF, thereby resulting in the decrease of the overall TCF of the sensor. More details about the choice of the patches' shape and size, together with the one for the dielectric material, are reported in section 5.1.2.

3.2.2 Laterally vibrating piezoelectric resonator

In general, a piezoelectric-based resonator is an electromechanical device in which electrical and mechanical energies are reciprocally converted to each other at a resonance frequency through the two-way coupling between stress and electric field in a piezoelectric material. Moreover, the mechanical energy in the resonator body and the applied electrical energy through the metallic electrodes convert from potential to kinetic and back in every vibration half cycle. Therefore, the overall performance of a resonant system is determined by both of the energy conversion mechanisms mentioned above. To quantify the efficiency of these energy conversions in a resonator, there are two specific parameters defined as [63]:

1. *effective electromechanical coupling factor* k_t^2, which is a unitless quantity (usually expressed in terms of percentage) that describes the efficiency of energy conversion processes in a resonator. It is different from the *piezoelectric coupling factor* K^2 of the material used in the resonator because, as expected, even if both unitless quantities, the latter is solely dependent on material properties and is not a function of the resonator design/implementation so that it could be used to compare the efficiency of different piezoelectric material in mutually converting electrical energy to mechanical energy. Therefore, once a piezoelectric material is used in a resonant device, the energy conversion efficiency at resonance is of great interest to the designers, and the K^2 will be always the upper bound of the k_t^2 of a resonator that uses a certain type of piezoelectric material because part of it is always lost because of the non-ideal design, even though optimal. In fact, the *effective electromechanical coupling factor* is largely affected by the properties of the piezoelectric material used as a transducer (i.e. its *piezoelectric coupling coefficient*), but it is also affected by the design of the resonator.

   To quantify this conversion efficiency, the *effective electromechanical coupling factor* can be extracted from the features of the frequency response plot as follows:

   $$k_t^2 = \frac{f_p^2 - f_s^2}{f_p^2}, \tag{3.38}$$

   where f_s and f_p are the frequencies at which the magnitude of the impedance is minimum and maximum, respectively. In particular, f_s is the *resonance frequency* where the series resonance occurs, while f_p is the *anti-resonance frequency* where the parallel resonance occurs.

   An alternative definition for the *effective electromechanical coupling factor* of a resonator is developed based on the equivalent electrical circuit representing the electrical characteristic of the resonator, which will be described later in this section.

2. *quality factor* Q, which represents a measure of energy loss in a resonator. As the energies convert from one form to the other, a portion of the energy contained in the system will either directly escape or repetitively turns into a form that could no longer be restored. It is generally defined as follows:

   $$Q = 2\pi \frac{\text{energy stored per cycle}}{\text{energy dissipated per cycle}}. \tag{3.39}$$

   There are several distinct dissipation mechanisms in a resonator. In particular, any loss mechanism is a coupling between the energy of the resonator and other forms of undesirable energy that randomly fluctuate. Therefore, each of these mechanisms can create a path for such energy fluctuations to perturb the energy of the system so that such random influx of energies are sources of noise/interference.

In principle, the overall quality factor of a system can be found by summing up the dissipated energies, but also in this case, since resonators are commonly characterized by their frequency response, it is practically convenient to extract it from the features of the frequency response plot as follows:

$$Q = \frac{f_0}{BW_{3dB}}, \tag{3.40}$$

where f_0 is the *fundamental resonance frequency* and BW_{3dB} stands for the *-3 dB frequency bandwidth*. Therefore, as expected, the Q increases in a resonator when the frequency response becomes sharper or, in other words, when the energy is more confined to the resonance frequency. A high quality factor is therefore desirable because it minimizes the amount of energy that is dissipated.

In conclusion, the *figure of merit* (FoM) for a piezoelectric-based resonator is proportional to both Q and k_t^2 as follows:

$$FoM = k_t^2 \cdot Q. \tag{3.41}$$

In particular, a typical laterally vibrating piezoelectric resonator is formed by a thin piezoelectric film sandwiched between metallic electrodes (see Figure 3.6). The application of a potential across the thickness of the piezoelectric film induces a lateral strain in the plane of the device. When the frequency of the excitation signal coincides with the mechanical resonance of the piezoelectric body, the device exhibits an enhanced amplitude of vibration, which is translated to an electrical signal by the direct piezoelectric effect and generates a charge proportional to the amplitude of the displacement.

For a longitudinal bar resonator vibrating along its width, the wave equation in one space dimension can be written as follows:

$$\rho_{eq}\frac{\partial^2 u}{\partial t^2} = E_{eq}\frac{\partial^2 u}{\partial x^2}, \tag{3.42}$$

where ρ_{eq} and E_{eq} are respectively the *equivalent density* and *Young's modulus* of the material stack forming the resonator, t is the *time* and x is the *direction of vibration* along which the *displacement* u occurs.

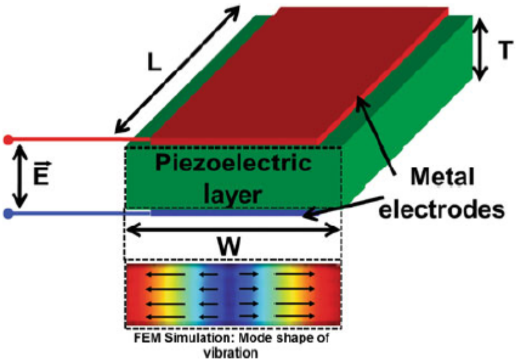

Figure 3.6: Mock-up view of a typical laterally vibrating piezoelectric resonator.

Considering a resonator of *width* W and applying the boundary conditions that there is no stress and no stress gradient at the free lateral boundaries of the resonator, i.e. at $x = \pm W/2$, the solution of the wave equation for the width-extensional vibration of the resonator becomes the product of a spatial component $U(x)$ representing the vibration mode shape and a temporal one $X(t)$:

$$u(x,t) = U(x) \cdot X(t) = sin(\beta_n x)e^{j\omega_0 t}, \tag{3.43}$$

where

$$\beta_n = (2n-1)\frac{\pi}{W}, \tag{3.44}$$

from which it is possible to derive the *fundamental resonant frequency* f_0 by computing the solution for $n = 1$:

$$f_0 = \frac{\omega_0}{2\pi} = \frac{1}{2W}\sqrt{\frac{E_{eq}}{\rho_{eq}}}. \tag{3.45}$$

Equation (3.45) highlights one of the main features of laterally vibrating resonators, i.e. the operating frequency of the resonator is set by the *width* W only. This allows to lithographically define its operating frequency independently from the *thickness* T and *length* L of the piezoelectric structure. Therefore, the device thickness and length can be independently selected to properly design both:

- the *electrical static capacitance* C_0, in order to keep it larger than the substrate parasitic capacitance so that the deterioration of the electromechanical coupling factor is avoided;
- the *motional resistance* R_m, in order to keep it as small as possible so that the direct interface of the device with compact and low-power 50-Ω electronics can be achieved;

of the piezoelectric transducer, which will be described in detail later in this section.

In fact, an LVR, as any other second-order mechanical system, can be represented by an *equivalent lumped mass* m_{eq}, a *spring* with constant k_{eq} and a *damper* with coefficient c_{eq} that depend on the mode of vibration of the structure and of its *quality factor* Q as follows:

$$m_{eq} = \rho_{eq}\frac{LTW}{2} \tag{3.46}$$

$$k_{eq} = \frac{\pi^2}{2}E_{eq}\frac{LT}{W} \tag{3.47}$$

$$c_{eq} = \frac{m_{eq}\omega_0}{Q} \tag{3.48}$$

These lumped mechanical variables of the LVR can be made to correspond to equivalent electrical variables in order to model the behavior of this mechanical structure in terms of circuit parameters and the most common equivalent electrical circuit of a resonator is known as the *Butterworth - Van Dyke* (*BVD*) model, shown in Figure 3.1 as the electrical port of the detector, which consists of the parallel between:

- a series RLC circuit called the *motional* or *acoustic branch*, composed by the series combination of the *motional resistance* R_m (quantifying dissipative losses and so directly proportional to the equivalent damping coefficient c_{eq}), the *motional capacitance* C_m (quantifying the elasticity of the resonant body and so inversely proportional to the equivalent stiffness constant k_{eq}) and the *motional inductance* L_m (quantifying the mass of the resonant body and so directly proportional to the equivalent mass m_{eq}):

$$R_m = \frac{c_{eq}}{\eta^2} \tag{3.49}$$

$$C_m = \frac{\eta^2}{k_{eq}} \tag{3.50}$$

$$L_m = \frac{m_{eq}}{\eta^2}, \tag{3.51}$$

where η is the *electromechanical transduction factor* that, relating force to voltage and so charge to displacement, represents the intrinsic capability of the piezoelectric structure to convert mechanical displacement into an electrical signal (and vice versa):

$$\eta = \frac{F}{V} = \frac{q}{u}. \tag{3.52}$$

Therefore, for a given geometry and material properties of the mechanical structure, the value of η determines the equivalent electrical impedance of the resonator. In particular, labeling the axis direction x, y, and z with numbers 1, 2, and 3, respectively, and assuming that:

- a uniform electric field E_3 applied across the thickness of the piezoelectric layer generates an orthogonal stress T_1 along the width of the structure;
- the electrode covers the entire surface of the piezoelectric material;
- the force is applied on both the electrode edges (i.e. at $x = \pm W/2$) in order to maximize the efficiency of this force in exciting the vibration mode described because it depends on the location where the force is applied along the width of the piezoelectric material and, indeed, the structure is most efficiently actuated from the two ends since they have the highest vibration amplitude;

the *electromechanical transduction factor* η of a width-extensional LVR can be expressed as follows:

$$\eta = 2e_{31}L, \tag{3.53}$$

where e_{31} is the *piezoelectric coefficient* (in C/m^2) relating the electric field along the z direction (i.e. 3) to the longitudinal stress along the x direction (i.e. 1). Therefore, now it is possible to express the lumped elements of the equivalent electrical circuit describing the width-extensional resonator as functions of the device's geometrical dimensions and material properties as follows:

$$R_m = \frac{\pi}{8}\frac{T}{L}\frac{\sqrt{E_{eq}\rho_{eq}}}{e_{31}^2 Q} \tag{3.54}$$

$$C_m = \frac{8}{\pi^2}\frac{WL}{T}\frac{e_{31}^2}{E_{eq}} \tag{3.55}$$

$$L_m = \frac{1}{8}\frac{WT}{L}\frac{\rho_{eq}}{e_{31}^2}; \tag{3.56}$$

- the *static* or *electrical branch*, composed by the *static electrical capacitance* C_0 of the piezoelectric transducer, which expresses the electrostatic coupling between two electrodes and is modeled as a parallel plate capacitance formed by the piezoelectric material sandwiched between two metal electrodes:

  $$C_0 = \epsilon_0 \epsilon_{33} \frac{LW}{T}, \tag{3.57}$$

  where ϵ_0 is the permittivity of the free space and ϵ_{33} is the *relative permittivity* (i.e. the *dielectric constant*) of the piezoelectric material in the direction of the electric filed (i.e. along z) applied in order to excite the vibration mode.

The modified BVD model, named mBVD, shown in Figure 3.1 includes also R_s in series with the parallel of the two branches described before, which models the electrical losses associated with the ohmic resistance of metal electrodes and traces' routing, and R_0 in parallel with C_0 in the electrical branch, which models the dielectric losses in the piezoelectric film. Other loss mechanisms such as the acoustic leakage may be also included in R_s and/or R_0. In fact, electric losses introduced by metal lines with relatively high resistivity such as Pt (knowing that Pt resistivity is about four times that of Al) can become significant especially if the *motional resistance* R_m of the resonators keeps decreasing up to very low values, which is what it is crucially necessary to achieve for the direct interface of the device with compact and low-power 50-Ω electronics. It is worth noting that this model neglects the intrinsic coupling between transversal and axial strains determined by the *Poisson's ratio* ν_{eq} of the material stack.

From the BVD model, it is possible to define the two parameters that best describe the performance of an electromechanical resonator, i.e. the *quality factor* Q:

$$Q = \frac{\omega_0 L_m}{R_m} = \frac{1}{R_m}\sqrt{\frac{L_m}{C_m}} = \frac{1}{R_m}\left(\frac{\pi}{8}\frac{T}{L}\frac{\sqrt{E_{eq}\rho_{eq}}}{e_{31}^2}\right) \tag{3.58}$$

knowing that $\omega_0 = \sqrt{k_{eq}/m_{eq}} = 1/\sqrt{C_m L_m}$, and the *effective electromechanical coupling factor* k_t^2:

$$k_t^2 = \frac{\pi^2}{8}\frac{C_m}{C_0} = \frac{e_{31}^2}{\epsilon_0 \epsilon_{33} E_{eq}}, \tag{3.59}$$

where e_{31} is the *piezoelectric constant* (with the unit of C/m^2) in the direction of the electric field and mechanical stress, E_{eq} is the *stiffness* (i.e. elastic constant with the unit of N/m^2) at zero electric fields, ϵ_0 is the *permittivity of the free space* (with the unit of F/m) and ϵ_{33} (dimensionless) is the *relative permittivity* or *dielectric constant* of the piezoelectric material in the direction of the electric field at zero stress so that in the end k_t^2 is dimensionless and expressed in percentage %.

In general, a temperature rise ΔT occurring in a resonant body leads to a shift Δf in the acoustic resonance frequency f_0 of the piezoelectric resonator due to its intrinsically large change of the Young's modulus of the material stack that forms the resonant body, which is quantified as the *temperature coefficient of frequency* TCF [64]. In fact, a resonator's resonance frequency often drifts as a result of temperature variation, due to the dependency of its material properties and physical dimensions on temperature so that the variation of f_0 with T is one of its most important characteristics. In particular, at a certain temperature point, the TCF of an LVR is given by the rate of frequency change with respect to temperature (with the unit of ppm/K or ppb/K):

$$\begin{aligned} TCF = \frac{\partial(\ln f_0)}{\partial T} = \frac{1}{f_0}\frac{\partial f_0}{\partial T} &= -\frac{1}{W}\frac{\partial W}{\partial T} - \frac{1}{2\rho_{eq}}\frac{\partial \rho_{eq}}{\partial T} + \frac{1}{2E_{eq}}\frac{\partial E_{eq}}{\partial T} \\ &= -\alpha_1 + \frac{1}{2E_{eq}}\frac{\partial E_{eq}}{\partial T} + \frac{1}{2}(2\alpha_1 + \alpha_3), \end{aligned} \tag{3.60}$$

where α_1 and α_3 are the *linear coefficient of thermal expansion* along x (i.e. in-plane) and z (out-of-plane), respectively, while $\partial(\ln E_{eq})/\partial T$ quantifies the temperature variation of the in-plane equivalent Young's modulus. Therefore, equation 3.60 states that, since the resonance frequency of a resonator is a function of the elastic constants of its materials and its physical dimensions, the sensitivity of the resonance frequency with respect to the temperature mainly comes from both the temperature coefficients of each material's elastic constants, i.e. the Young's modulus, and the thermal expansion coefficient of each material. However, between these two factors, the temperature coefficients of the elastic constants are usually at least an order of magnitude larger than the thermal expansion coefficients of the materials and so they play the dominant role.

It is worth mentioning once again that the fabrication process of an $ScAlN$ nano-plate resonator is post-CMOS compatible, which means that the micro-fabrication process starts with a CMOS wafer and only uses materials that are post-CMOS compatible, i.e. which can be deposited with temperature < 400 °C and dry etched using standard CMOS tools.

3.3 Read-out circuit

The MEMS-CMOS read-out circuit consists of a Pierce oscillator incorporating the IR detector, i.e. the $ScAlN$ resonator with plasmonic metamaterial absorbers integrated on top of it, in its feedback loop. A reference oscillator, which uses the same $ScAlN$ resonator, but simply coated with a blanket Au layer acting as a reflector for IR light, is used to differentially estimate the shift in resonance frequency caused by the N_2O concentration-modulated IR beam impinging on the chip. The output of the mixer is fed to a frequency-to-voltage converter and an analog-to-digital converter (ADC) to obtain a voltage output ready to be correlated to the gas concentration. The circuit also includes a COTS (Commercial Off-The-Shelf) temperature and humidity sensor, and an NDIR CO_2 sensor to monitor and compensate for temperature, humidity, and CO_2 fluctuations, respectively. The overall system is powered by a compact and light-weighted 12 V battery. Figure 3.7 shows the high-level schematic of the proposed read-out circuit.

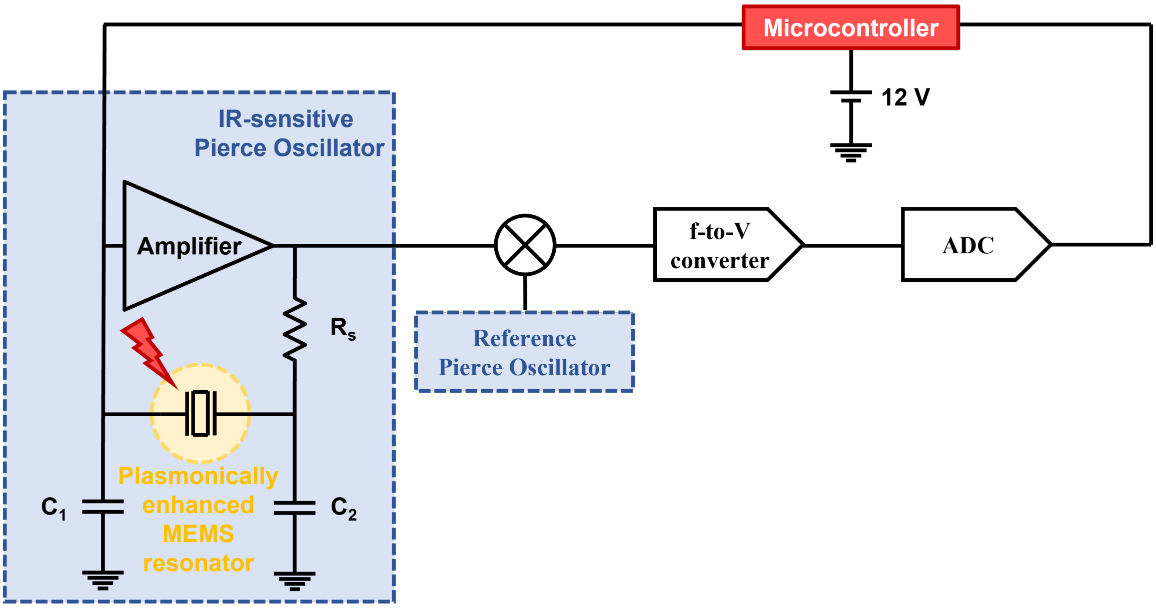

Figure 3.7: High-level schematic of the read-out circuit.

In general, oscillators are circuits that are typically used to generate a time reference, consisting of a signal that is as close as possible to be perfectly periodical, i.e. as stable as possible. In particular, any oscillator can be described by an amplifier connected in a feedback loop with its output fed back into its input through a frequency selective component to provide positive feedback, such as the one shown in Figure 3.8 so that, at a steady state, the *closed-loop voltage gain* is given by:

$$\frac{v_o}{v_i} = \frac{A_v}{1-\beta A_v} \tag{3.61}$$

where A_v is the voltage gain of the amplifier and β is the frequency response of the feedback network. Their product is defined as *loop gain*.

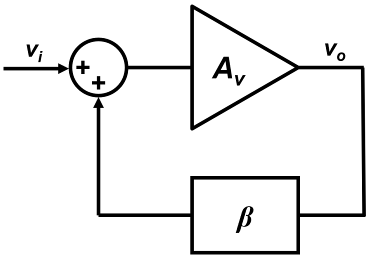

Figure 3.8: General block diagram of an oscillator.

In order to generate a sustained oscillation, i.e. a sinusoidal output signal that neither dies out nor goes unstable at a certain frequency (while all the other frequency components die out), the input noise signal v_i must be progressively filtered and amplified traveling around the loop. In particular, for oscillation to occur, the output signal v_o must exist when no input signal v_i is applied, which means that, when v_i is 0, v_o must be finite. This condition is satisfied when the loop gain is equal to 1, known as *Barkhausen criterion*:

$$A_v\beta = 1. \tag{3.62}$$

In fact, when v_i is equal to 0, v_0 is finite only when the denominator of equation 3.61 is equal to 0. In particular, since A_v and β are complex, when v_i is equal to 0, v_o has a finite value different from 0 if:

$$\begin{cases} |A_v\beta| = 1 \\ \angle A_v\beta = \pm n360^\circ \end{cases} \tag{3.63}$$

where n is an integer. In particular, the *amplitude condition* states that the voltage gain A_v of the amplifier must perfectly compensate the losses β introduced by the feedback path to make the oscillation stable. However, to start the oscillation, the loop gain must be greater than unity. On the other hand, the *frequency of oscillation condition* states that the total phase shift associated with the closed-loop must be equal to zero or a multiple of 360°, so that, if the amplifier is an inverter, the feedback network must provide an additional phase shift of 180° ± 360 °.

The Pierce, Colpitts, and Clapp oscillators consist of the same circuit, but their ground is placed in a different location [65]. There are many other circuit configurations, but they are generally more complicated to design and use a larger amount of parts. Among them, the most common is the Pierce oscillator, where:

- the amplifier is an inverter, i.e. its voltage gain A_v is negative;
- the feedback network is a frequency-selective π-network (see Figure 3.9), so that:

$$\beta = \frac{Z_1}{Z_1 + Z_3}. \tag{3.64}$$

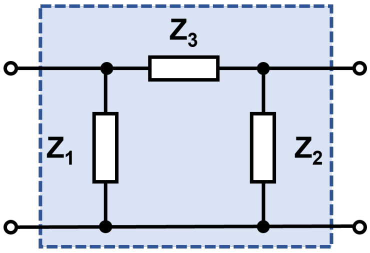

Figure 3.9: General configuration for the feedback network of a Pierce oscillator.

Assuming that Z_1, Z_2, and Z_3 are purely reactive impedances equal to jX_1, jX_2, and jX_3, respectively, the phase condition of the Barkhausen criterion can be demonstrated to be satisfied at a certain frequency f_{osc} such that:

$$X_1(f_{osc}) + X_2(f_{osc}) + X_3(f_{osc}) = 0. \tag{3.65}$$

From equation 3.65 the frequency of oscillation of the oscillator can be determined. Moreover, equation 3.64 can be rewritten at the frequency of oscillation as follows:

$$\beta(f_{osc}) = -\frac{X_1(f_{osc})}{X_2(f_{osc})}, \tag{3.66}$$

so that the loop gain at the frequency of oscillation is now equal to:

$$A_v(f_{osc})\beta(f_{osc}) = -A_v(f_{osc})\frac{X_1(f_{osc})}{X_2(f_{osc})}, \tag{3.67}$$

which means that, since A_v is negative, $X_1(f_{osc})$ and $X_2(f_{osc})$ must have the same sign in order to satisfy the amplitude condition of the Barkhausen criterion.

Typically, Z_1 and Z_2 are pure capacitive reactances, thereby implying that Z_3 is a pure inductive reactance. Therefore, in this case, the oscillator circuit becomes the one shown in Figure 3.10 and equation 3.66 can be rewritten as follows:

$$\beta(f_{osc}) = -\frac{-\frac{1}{2\pi f_{osc} C_1}}{-\frac{1}{2\pi f_{osc} C_2}} = -\frac{C_2}{C_1}. \tag{3.68}$$

Equation 3.68 states that the phase shift induced by this feedback network is equal to 180°. Therefore, since the amplifier is an inverter, i.e. the induced phase shift is equal to 180°, the overall loop gain has a phase shift equal to 360°, thereby satisfying the phase condition of the Barkhausen criterion. Moreover, from the amplitude condition of the Barkhausen criterion, it follows that the absolute value of the voltage gain of the amplifier must be larger than the ratio between C_1 and C_2.

The problem arising from using a real inductor in the Pierce oscillator is related to its relatively low quality factor. Therefore, it is typically substituted by a high-quality factor piezoelectric resonator, which satisfies the phase condition, i.e. it behaves as a pure inductor (see Figure 3.11), just in the narrow spectral range between the series and parallel resonance frequencies [66]. All the other harmonics whose frequency is out of that range violate the Barkhausen criterion, thereby being suppressed and so allowing to generate an oscillation exactly around the resonance of the piezoelectric resonator.

It can be demonstrated that, replacing a pure inductor with a piezoelectric resonator in the feedback network of a Pierce oscillator as shown in Figure 3.10, the oscillation frequency turns out to be equal to:

$$f_{osc} \simeq f_{r_s}\left[1 + \frac{C_1}{2(C_0 + C_L)}\right], \tag{3.69}$$

where f_{r_s} and C_0 are the series resonance frequency and the static capacitance of the resonator, respectively, while C_L is the *load capacitance*, defined as the series combination of C_1 and C_2 :

$$\frac{1}{C_L} = \frac{1}{C_1} + \frac{1}{C_2}. \tag{3.70}$$

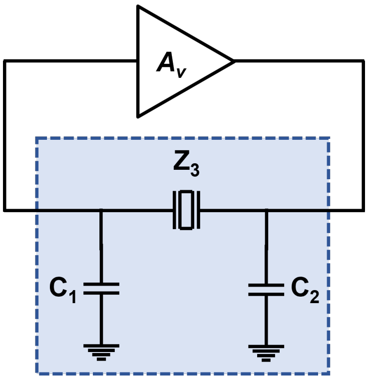

Figure 3.10: High-level schematic of the Pierce oscillator configuration using a resonator in the feedback network instead of a real inductor.

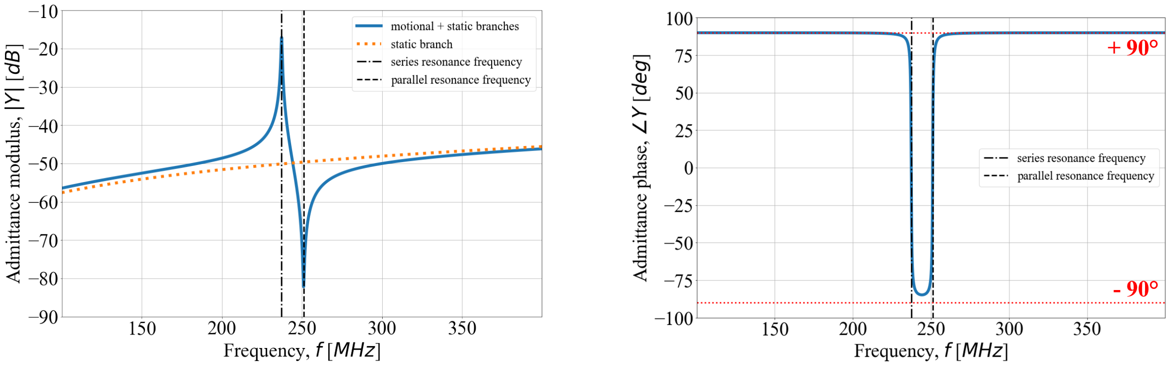

(a) Simulated admittance modulus.

(b) Simulated admittance phase. The phase is equal to + 90°, i.e. the resonator acts as a capacitor, except for the range between the series and the parallel resonance frequencies, where the phase theoretically reaches - 90°, i.e. the resonator acts as an inductor, passing from 0, i.e. the resonator acts as a pure resistor, exactly at the series and the parallel resonance frequencies.

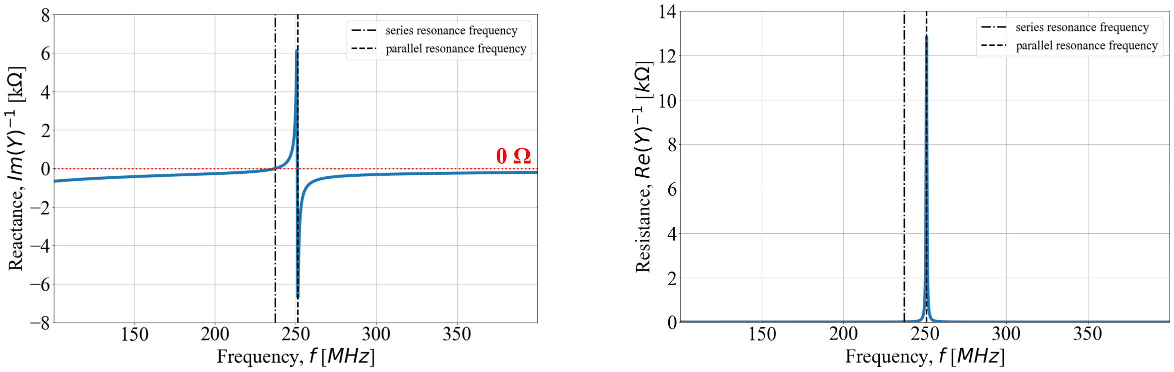

(c) Simulated reactance. The reactance is purely capacitive except for the range between the series and the parallel resonance frequencies, where the reactance is purely inductive passing from 0, i.e. the resonator acts as a pure resistor, exactly at the series and the parallel resonance frequencies.

(d) Simulated resistance. The resistance is negligible except for a spike at the parallel resonance frequency.

Figure 3.11: Results obtained from the analytical BVD model (without taking into account both the resistance modeling the dielectric losses, i.e. R_0, and the series resistance modeling the electrical losses associated with metal electrodes and routing, i.e. R_s) for a 30%-doped $ScAlN$ LVR with motional Q equal to 1000, and series and parallel resonance frequencies equal to around 237 MHz (dash-dotted black line) and 251 MHz (dashed black line), respectively.

Another important design equation for a Pierce oscillator with a piezoelectric resonator in its feedback network is the one that quantifies the *drive level*, i.e. the amount of power dissipated by the resonator. Monitoring this value is crucial to ensure good performance: if the drive level is too low, the oscillator might fail to oscillate or might have degraded performance in terms of phase noise, while a high drive level might damage the resonator or burn it. It can be evaluated as follows:

$$P_{dissipated} \simeq R_e \left(2\pi f_{osc} C_2 \frac{V_{DD}}{2\sqrt{2}}\right)^2, \tag{3.71}$$

where R_e is the effective resistance of the resonator at the frequency of oscillation, and $\frac{V_{DD}}{2\sqrt{2}}$ is the

RMS value of the supply voltage. Additionally, the resistor R_s shown in Figure 3.7 can be used to reduce the drive level by controlling the amount of current driving the resonator.

It is worth mentioning also that, in order to enhance the purity of the oscillating frequency, it is crucial to design the sustaining circuit in such a way that the oscillator operates as close as possible to the series resonant frequency f_{r_s} because it is the frequency that is predominantly determined by the intrinsic electromechanical behavior of the piezoelectric structure. Furthermore, it is the one that is the least affected by parasitic capacitances arising from the silicon substrate, bonding pads, or packaging.

However, real systems deviate from perfect periodicity and the deviation from their ideal perfect periodicity is referred to as *phase noise*. In particular, the phase noise, also called random or unintentional phase modulation, describes the variations in terms of frequency stability leading to a broadening of the spectral line in the frequency domain, which can cause the so-called *spectral regrowth* because, if the local oscillator of a mixer has phase noise, also the mixing products are subjected to a distortion and broadening effect that makes them more prone to interference issues.

In general, the assessment of frequency stability is crucial to maximizing the performance of the system. To this aim, the phase noise is typically quantified in the frequency domain or in the time domain. In particular, in the time domain, *Allan deviation* measurements are used to assess the long-term frequency stability by quantifying how much the output deviates from the nominal frequency over long integration times. Typically, there is an integration time that minimizes the Allan deviation and, according to its value, the sampling rate of the system should be set in order to maximize its sensitivity.

Chapter 4

Method

4.1 Refined SWaP milestones

Through the investigation of existing commercial components, a thorough study of the SWaP was performed, and an estimation of the system's power consumption and footprint was calculated. Moreover, an analysis based on the stationary EC measurement was also performed in order to determine the data acquisition rate of the system.

The initial system's specifications defined in section 2.1 were then updated with revised values that are expected to still ensure that the system meets the performance demanded by its final applicability for agricultural lands monitoring.

4.1.1 Data acquisition rate

An analysis based on the stationary EC measurement was performed to determine the data acquisition rate of the sensor. In stationary EC systems, it has been shown that a 1 Hz sampling rate is sufficiently fast to operate with an average wind speed of ~ 7 mph at an effective measuring height of 18 m [15]. Assuming that the drone is cruising at its maximum speed of ~ 50 mph [16], the equivalent wind velocity experienced by the system will be equal to the sum of the wind velocity and drone velocity (~ 70 mph, assuming a wind speed equal to 20 mph in the worst case scenario, i.e. level 4 of the Beaufort Wind Scale [67]). Since the wind velocity is proportional to the gas exchange rate, the sampling rate will scale linearly with the equivalent wind velocity.

According to this analysis, a sampling rate of 10 Hz will be sufficient to meet EC specifications. Therefore, relaxing the sampling rate from 20 Hz to 10 Hz, a spatial resolution of 2.3 m is achieved and a total distance of 63.5 km can be covered by the drone assuming that it is flying at its maximum cruising speed of 50 mph for a maximum flight time of 46 minutes.

4.1.2 Power consumption

Through the investigation of existing commercial components, a thorough study of the SWaP was performed, and an estimation of the system's power consumption was calculated. The read-out circuit combined with the IR MEMS resonator consumes an average of 0.4 mW (a negligible fraction of the power budget), the NDIR CO_2 sensor consumes an average power of 0.2 W [20], the COTS temperature and humidity sensor consumes an average power of 1.2 μW [68]. The QCL, on the other hand, consumes a typical power of 2.1 W [69]. Therefore, the total estimated power is approximately 1.8 W. Using a 14.8 V battery with a typical capacity of 450 mAh [70] and considering a maximum current of 400 mA consumed by the system, a circuit with a 2 W power consumption can be powered for more than 1 hour, exceeding the flight time.

According to this calculation, the power consumption specification can be relaxed and increased to less than 2.5 W.

4.1.3 Weight and volume

An estimation of the system's footprint, volume, and size was performed based on existing commercial components and products. The readout circuit combined with the IR MEMS resonator weights an average of 70 g and consumes a volume of 0.025 L (considering a chip occupying an area equal to 5x5 cm), the NDIR CO_2 sensor weights an average of 30 g and occupies an average volume of 0.01 L [20], the COTS temperature and humidity sensor weights an average of 5 g and consumes a negligible volume [68], the battery weights overall 55 g and occupies a volume of 0.03 L [70], the QCL weights an average of 80 g and occupies a volume of 0.886 mL [69]. With the design of an ultra-compact and light weighted gas cell with a volume of 0.3 L and a weight of 200 g, the total weight and volume of the system will be equal to 425 g and 0.355 L, respectively.

According to this calculation, the volume of the system meets the initial specifications, and keeping the volume as small as possible plays a very important role in the final application of the system since it reduces the air resistance (the drag force is directly proportional to the square of the volume), thereby making the flight time longer. However, the weight of the system can be relaxed and increased to less than 500 g. Figure 4.1, illustrates the relationship between the payload weight and maximum flight time of the selected drone. It demonstrates that changing the payload weight from 400 g to 500 g will cause a reduction of the flight time of only less than 2 minutes, thereby not affecting the final outcome of the application.

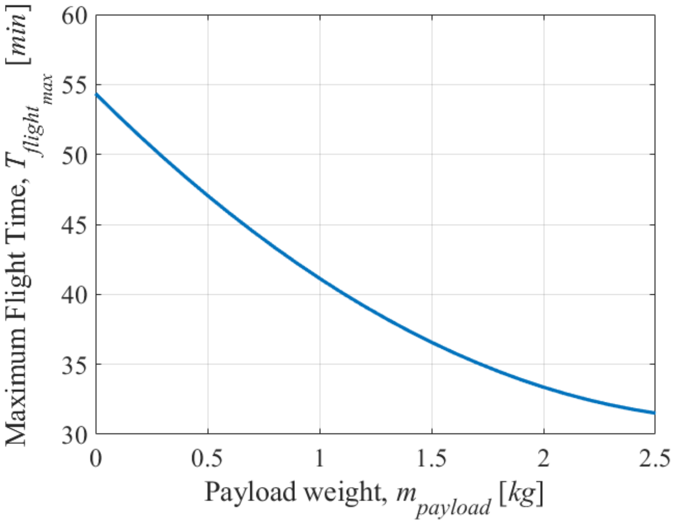

Figure 4.1: Change of the maximum flight time as a function of the payload's weight (data from [16]).

4.2 MWIR molecular absorption spectrum extraction

The MWIR spectral region is particularly important for trace gas detection and, in general, for applications of molecular absorption spectroscopy, because it accommodates the fundamental vibrational bands of several interesting molecules in gaseous samples like the ones which are interesting for atmospheric and environmental monitoring.

From the technological point of view, the highest sensitivity, i.e. the capability of detecting small concentrations can usually be obtained by using laser spectroscopy. This results from the high brightness and spatial coherence of lasers, which makes it possible to reach high Signal-to-Noise Ratios (SNRs) and long absorption path lengths. The sensitivity can be further increased by using MPCs and enhanced optical cavities. The high brightness also means that the high measurement sensitivity can be obtained with a short averaging time, which leads to fast, in practice real-time measurements. Also, the spectroscopic selectivity, i.e. the capability of resolving one molecular absorption line or species from another, is superior in laser spectroscopy because of the very sharp emission spectrum of lasers, as compared to more conventional methods based on more broadband light sources or relying on completely different detection principles.

From the fundamental point of view, the detection sensitivity can be optimized by doing spectroscopy in the MWIR spectral region, where many trace gas molecules have their strongest absorption features because of the presence of their fundamental rotational-vibrational bands. In particular, here the attention is focused on the so-called *atmospheric window*, i.e. at 3–5 μm (2000–3300 cm^{-1}), where the strongest absorption bands of the carbohydrates (CH stretch) and molecules with NH or OH stretching vibration lie. Moreover, within this particular spectral region, water vapor absorption is relatively small and this is useful in certain applications, such as atmospheric and environmental monitoring, where the measurement of trace gas spectra is often complicated by strong spectral features of the abundant water molecule.

MWIR molecular spectroscopy and, in particular, its application to trace gas analysis, has progressed significantly during the past two decades, owing to the development of coherent mid-infrared sources, detectors, and methods. One of the important enabling technological advances has been the invention of room-temperature QCLs and ICLs, which have extended the operating range of tunable semiconductor lasers from the visible and near-infrared to the mid-infrared [71].

Figure 4.2 shows the molar absorption cross-section spectra of the main trace gas molecules in the *atmospheric window*, without taking into account the abundances of the molecular species. In particular, they have been built by taking the fundamental spectroscopic parameters of a line transition (see Figure 4.3), i.e. the molecular line strength (spectral line intensity, S_{ij}, visualized as a shaded area under the line contour since it basically represents the integral of the absorbance over one line normalized with respect to both the optical path length and the concentration), its spectral position (wavenumber of the spectral line transition between lower and upper states i and j, ν_{ij}, in vacuum), and the line shape parameters γ and δ at the reference temperature and pressure (i.e. 296 K and 1 atm, respectively), from the HITRAN 2020 molecular spectroscopic database [72].

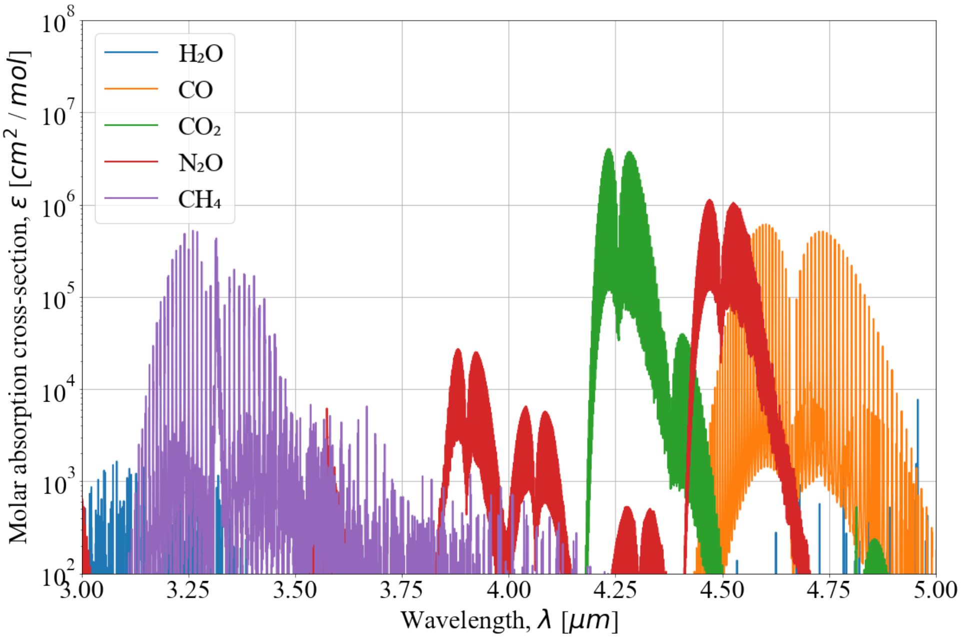

Figure 4.2: MIR absorption spectra of the main gases in the atmospheric window (3-5 μm) at 296 K and 1 atm from HITRAN database.

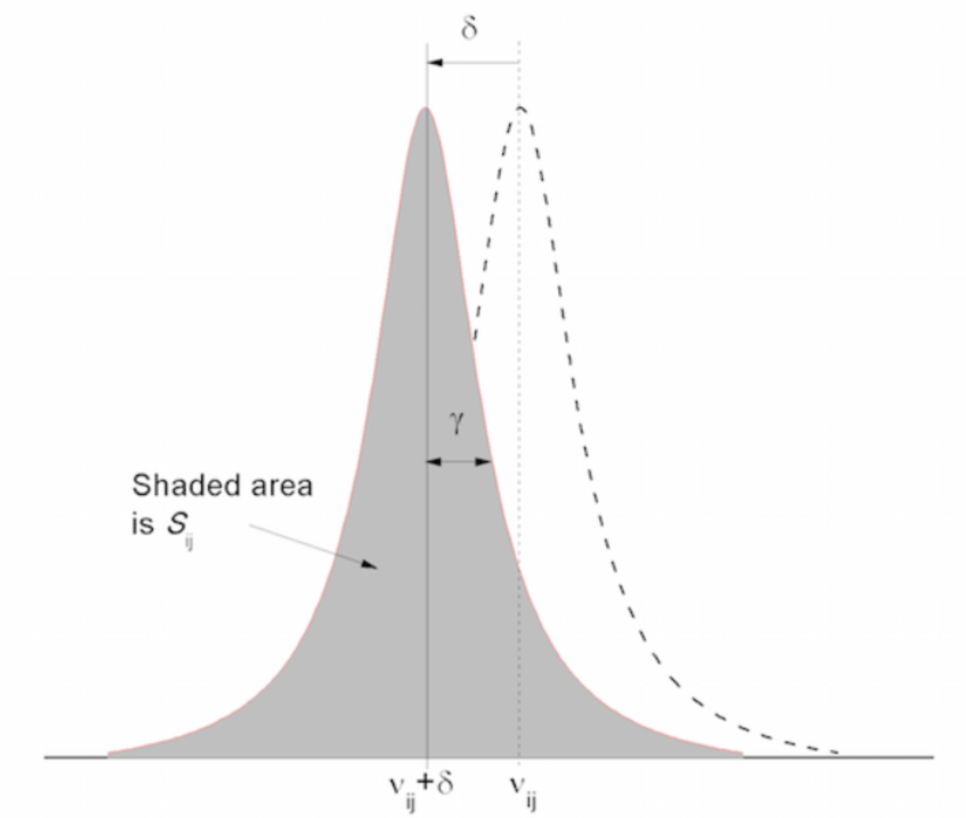

Figure 4.3: Schematic of fundamental spectroscopic parameters of a line transition in HITRAN (from [73]). The Lorentzian profile is assumed.

An analysis of the variation of the molar absorption cross-section spectra of the same trace gas molecules as a function of the temperature T and pressure p has been performed. In particular, the dependence of the line shape parameters, i.e. the half-width at half-maximum (HWHM) γ and the line shift δ, are first discussed:

- the line shift induced by a pressure p leads to a shifted position ν^*_{ij} of the transition wavenumber with respect to the vacuum transition one ν_{ij} that is proportional to δ:

  $$\nu^*_{ij} = \nu_{ij} + \delta p. \tag{4.1}$$

  It should include also a temperature dependence, but this effect has not been included in the HITRAN database yet.

- the Lorentzian HWHM $\gamma(p, T)$ for a gas at pressure p (atm), temperature T (K) and partial pressure p_{self} (atm) is calculated as:

  $$\gamma(p, T) = \left(\frac{T_{ref}}{T}\right)^{n_{air}} \left[\gamma_{air}(p_{ref}, T_{ref})(p - p_{self}) + \gamma_{self}(p_{ref}, T_{ref})p_{self}\right], \tag{4.2}$$

  where γ_{air} and γ_{self} represent the air-broadened and self-broadened contribution to the HWHM, respectively.

On the other hand, in order to calculate the line intensity at temperatures different from the HITRAN reference temperature of 296 K, one uses the following expression

$$S_{ij}(T) = S_{ij}(T_{ref}) \frac{Q(T_{ref})}{Q(T)} \frac{e^{-\frac{hcE''}{kT}} \left(1 - e^{-\frac{hc\nu_{ij}}{kT}}\right)}{e^{-\frac{hcE''}{kT_{ref}}} \left(1 - e^{-\frac{hc\nu_{ij}}{kT_{ref}}}\right)}, \tag{4.3}$$

where $Q(T)$ is the Total Internal Partition Sums (TIPS), h and k are the Planck and Boltzmann constants, respectively, E'' is the lower-state energy of the transition, and c is the speed of light so that hcE'' is the lower state energy and ν_{ij} is the wavenumber of the transition to which the spectral line is related. In particular, every isotopologue of a certain molecule has a unique set of quantum energy states, and the TIPS extracted from a supplemental data section of the HITRAN dataset [74] are given by summing over all the quantum energy states of that certain isotopologue. To this aim, the TIPS are very useful quantities because, for example, the equation of the state of a gas, the thermodynamic functions, or the heat capacity, can be written in terms of the TIPS and their dependence on the temperature.

Therefore, equations 4.1, 4.2, and 4.3 allow the parameters taken from HITRAN at a reference temperature and pressure to be propagated to other temperatures and pressures different from the reference ones.

In fact, in the atmosphere, a spectral line is broadened around the transition wavenumber ν_{ij} and the spread is represented by a normalized line-shape function that is usually assumed to be the Voigt one, which is a convolution of a Gaussian (Doppler-broadened) profile f_G and Lorentzian (pressure-broadened) profile f_L. However, in the lower atmosphere, i.e. close to the surface of the Earth, which is the space where the system is going to operate in its final application, pressure broadening of spectral lines dominates over the Doppler one (valid at very high altitudes) and a Lorentz profile can be assumed:

$$f_L(\nu,\nu_{ij},T,p)=\frac{1}{\pi}\frac{\gamma(p,T)}{\gamma(p,T)^2+(\nu-\nu_{ij}^*)^2}=\frac{1}{\pi}\frac{\gamma(p,T)}{\gamma(p,T)^2+\left[\nu-(\nu_{ij}+\delta p)\right]^2}. \tag{4.4}$$

In conclusion, the molecular absorption cross-section $\sigma(\nu,T,p)$ at a certain wavenumber ν, temperature T, and pressure p due to the single transition between lower and upper states i and j is given by:

$$\sigma_{ij}(\nu,T,p)=S_{ij}(T)f_L(\nu,\nu_{ij},T,p). \tag{4.5}$$

This equation is accurate enough to calculate the absorbance over a wavenumber range that is narrower than a single spectral line. However, for an equally accurate calculation over a wavenumber range wider than a single spectral line and so that includes more than one spectral line, it is necessary to sum over the contribution due to every spectral line inside that range because of the slow decay of the Lorentz function. Moreover, because of the peakiness of the spectrum, it is desirable to integrate the absorbance over each wavenumber value [75]. Therefore, the molecular absorption cross-section $\sigma(\nu,T,p)$ at a certain wavenumber ν, temperature T, and pressure p due to all the possible transition lines included into a wavenumber range centered in ν and symmetrically extended by $\Delta\nu$ is given by:

$$\sigma(\nu,T,p)=\sum\sigma_{ij}(\nu,T,p)=\frac{1}{2\Delta\nu}\sum S_{ij}(T)\int_{\nu-\Delta\nu}^{\nu+\Delta\nu}f_L(\nu,\nu_{ij},T,p)d\nu, \tag{4.6}$$

where

$$\int f_L(\nu,\nu_{ij},T,p)=\frac{1}{\pi}\int\frac{\gamma(p,T)}{\gamma(p,T)^2+(\nu-\nu_{ij}^*)^2}d\nu=\frac{1}{\pi}\text{atan}\left(\frac{\nu-\nu_{ij}^*}{\gamma(p,T)}\right). \tag{4.7}$$

Finally, the molar cross-section $\epsilon(\nu,T,p)$ can be obtained multiplying by the Avogadro's number N_A:

$$\epsilon(\nu,T,p)=N_A\cdot\sigma(\nu,T,p). \tag{4.8}$$

In conclusion, the HITRAN-based spectra of N_2O, CO_2, CO, CH_4, and H_2O absorption lines depicted in Figure 4.2 and extracted by the previously described expressions were used to assess potential interferences to N_2O detection coming from other atmospheric species whose absorption lines lie in the same spectral range.

4.3 Fabrication

Experimental characterization and optimization of the bottom electrode were performed as a first step after the design of the resonator described in section 5.1.3. This study is crucial since the quality of the piezoelectric layer depends on the smoothness of the surface underneath. For this purpose, a LOR photoresist was used for the lithography of the bottom electrode, combined with a lift-off process to obtain an undercut and therefore bottom fingers with smooth round edges. The recipe of the LOR was optimized to maximize the undercut and reduce the fencing effect, which consists in having unwanted metal on the edge of a feature. A comparison between the bottom fingers before and after optimization is shown in Figure 4.4.

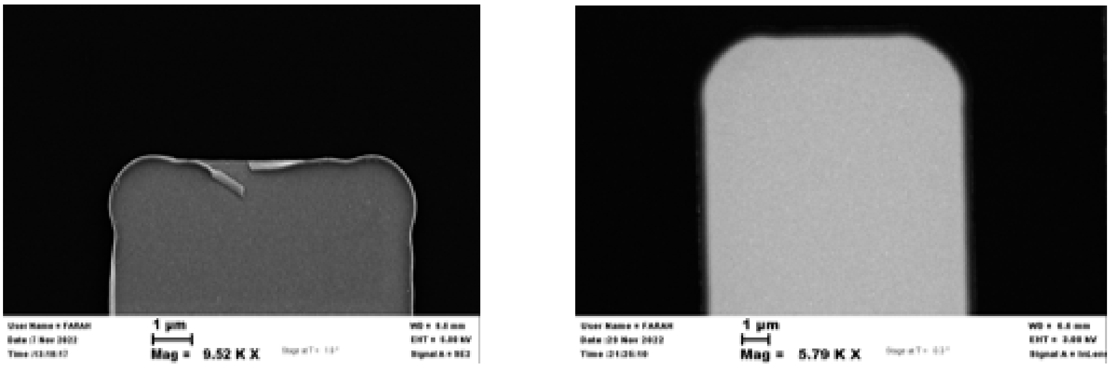

(a) Before optimization (top view).

(b) After optimization (top view).

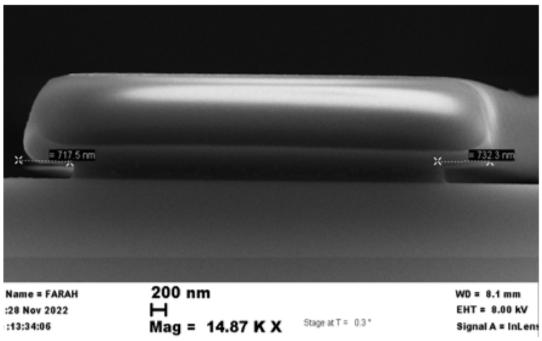

(c) After optimization (side view).

Figure 4.4: SEM picture of the fingers of the bottom interdigitated electrode.

Additionally, experimental characterization and optimization of the piezoelectric material were also conducted. Films of 36%-doped $ScAlN$ with thickness 250 nm were deposited on the patterned Pt layer using the Evatec CLUSTERLINE® 200 II multi-target co-sputtering deposition tool with different recipes. The crystallinity and inplane stress were measured to assess the quality of the film and to find the optimal recipe for the deposition, resulting in a rocking curve of 2.15 ° and a stress gradient of 375 MPa.

4.3.1 First batch

The resonators were fabricated using a five-mask process on three wafers with three different piezoelectric films, i.e. $ScAlN$ with different Sc concentration (15%, 28%, and 36%), in order to study the difference between the three designs and confirm the optimal Sc concentration to maximize the performance of the sensor. All the fabrication process steps are summed up in Table 4.1 and shown in Figure 4.5.

Process step	**Name**	**Details**
1	**Bottom electrode**	- LOR3A + S1813 lithography - Ti-Pt (10-50 nm) deposition by sputtering - Lift-off process
2	**Piezoelectric layer**	$ScAlN$ (250 nm) deposition by reactive sputtering
3	**Etch pits** **Anchors**	- S1813 lithography - Chlorine based Dry etch
4	**Top electrode resonator**	- S1813 lithography - Ti-Pt (10-50 nm) deposition by sputtering - Lift-off process
5	**Vias**	Wet etch in phosphoric acid
6	**Dicing**	Hand cut
7	**Release**	XeF_2 dry etch (40 cycles)

Table 4.1: Summary of process steps for the first batch of the fabrication.

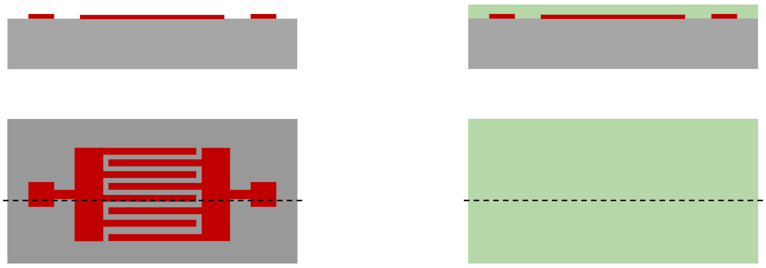

(a) Step 1: Sputtering and lift-off of 50 nm-thick Pt IDE.

(b) Step 2: Sputtering of 250 nm-thick $ScAlN$.

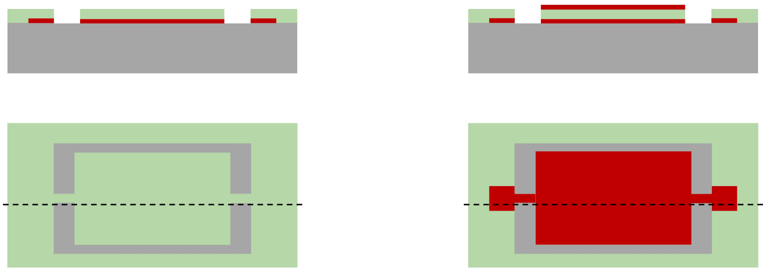

(c) Step 3: Dry etch for release pit.

(d) Step 4: Sputtering and lift-off of 50 nm-thick Pt layer.

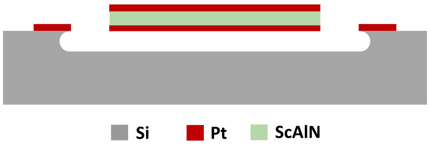

(e) Final step: releasing.

Figure 4.5: Overall schematic illustration of the device after the main microfabrication process steps followed during the first batch: cross-section on top and top view on the bottom.

After the testing of these devices with the vector analyzer, they turned out to have a low quality factor (around ~ 70) due to two main reasons:

1. the electrical loading of the devices was high, i.e. the electrical series resistance was large since the parasitic resistance was measured and was found to be around $\sim 260\ \Omega$, due to the high resistivity of Pt pads;
2. the devices were bending, as shown in the scanning electron microscope (SEM) image in Figure 4.6 visualizing the fabricated devices since the stress gradient through the metal stack introduced by the top Pt electrode layer was very high and all the three layers composing the device were extremely thin. This bending distorted significantly the shape of the acoustic cavity, thereby increasing the motional resistance and so reducing the quality factor of the device.

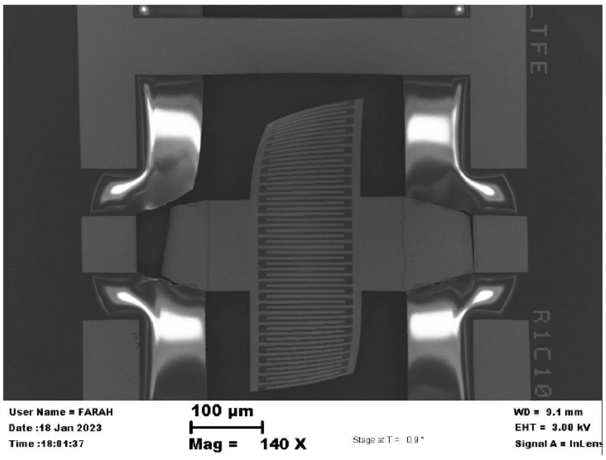

Figure 4.6: SEM picture of a bending resonator fabricated in the first batch.

4.3.2 Second batch

A second attempt to refine the design and solve the previously encountered problems was performed.

In particular, in order to solve the first issue of the previous batch, the pads were made of Au to improve the conductivity of the routing and reduce the series electrical resistance. On the other hand, in order to solve the second one, two solutions have been investigated: increasing the thickness of all the layers of the material stack to lower the amount of bending introduced by residual stress mismatch and changing the recipe for the top electrode to reduce the overall stress gradient in the stack. In particular, the best solution was changing the material of the top electrode from Pt to Al. Since Al is both softer and more electrically conductive than Pt, it led to an improvement of both the stress gradient and the series of electrical resistance issues. Moreover, the number of interdigitated fingers was reduced to minimize the area of the devices and therefore the number of release cycles required to fully release the devices, which decreased from 40 to 15. With such a lower amount of release cycles, the devices turned out to be less prone to bending and breaking.

The devices were fabricated using a six-mask process on wafers with the same piezoelectric film, i.e. 30%-doped $ScAlN$, to ensure a high electromechanical coupling and TCF due to the heavy Sc doping of AlN. All the fabrication process steps are summed up in Table 4.2 and shown in Figure 4.8.

Process step	Name	Details
1	**Bottom electrode**	- LOR3A + S1813 lithography - Ti-Pt (10-100 nm) deposition by sputtering - Lift-off process
2	**Piezoelectric layer**	$ScAlN$ (350 nm) deposition by reactive sputtering
3	**Top electrode resonator** **Bottom metal absorber**	- S1813 lithography - Ti-Al (10-100 nm) deposition by sputtering - Lift-off process
4	**Dielectric spacer absorber**	- AlN (250 nm) deposition
5	**Etch pits** **Anchors**	- S1813 lithography - Chlorine based Dry etch
6	**Vias**	Wet etch with H_3PO_4
7	**Pads**	- S1813 lithography - Ti-Au (10-90 nm) deposition by evaporation - Lift-off process
8	**Metal patches absorber**	- E-beam lithography - Ti-Au (5-80 nm) deposition by evaporation - Lift-off process
9	**Dicing**	Hand cut
10	**Release**	XeF_2 etching (15 cycles)

Table 4.2: Summary of process steps for the second batch of the fabrication.

From the testing of these devices, as expected, an improvement was obtained and they turned out to have a high motional quality factor (Q_m around $\sim$ 800) and good electromechanical coupling (k_t^2 around $\sim$ 3.3%).

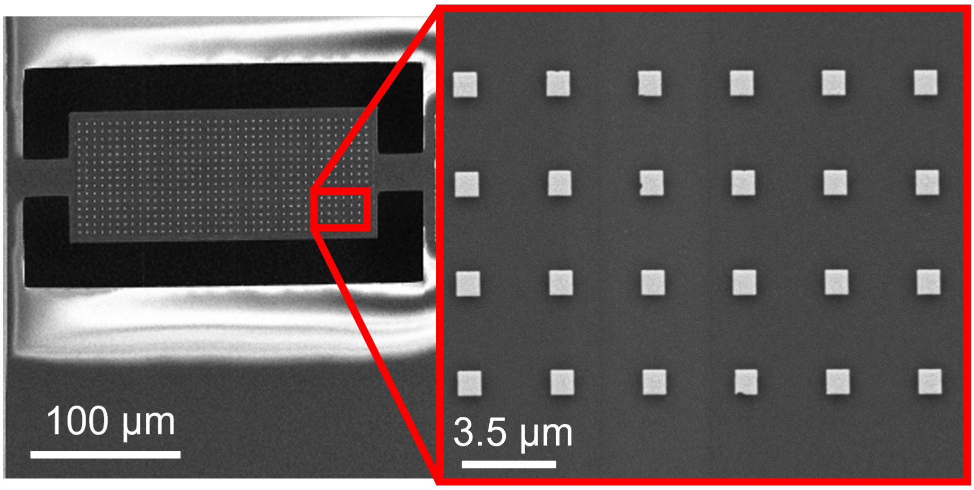

Figure 4.7: SEM picture of the resonator and plasmonic absorber fabricated in the second batch.

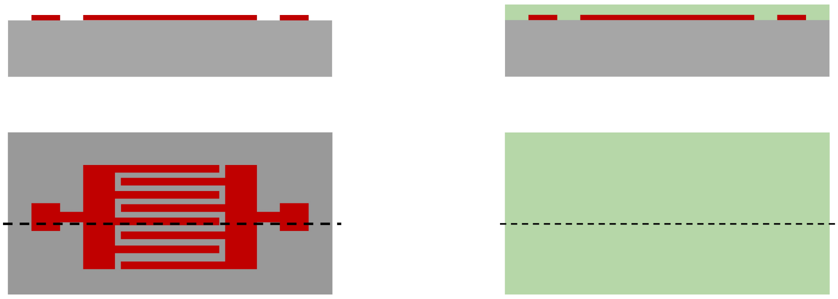

(a) Step 1: Sputtering and lift-off of 100 nm-thick Pt IDE.

(b) Step 2: Sputtering of 350 nm-thick $ScAlN$.

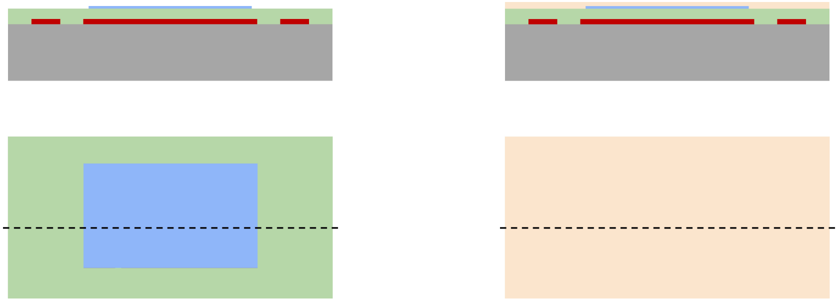

(c) Step 3: Sputtering of 100 nm-thick Al plate.

(d) Step 4: Sputtering of 250 nm-thick AlN.

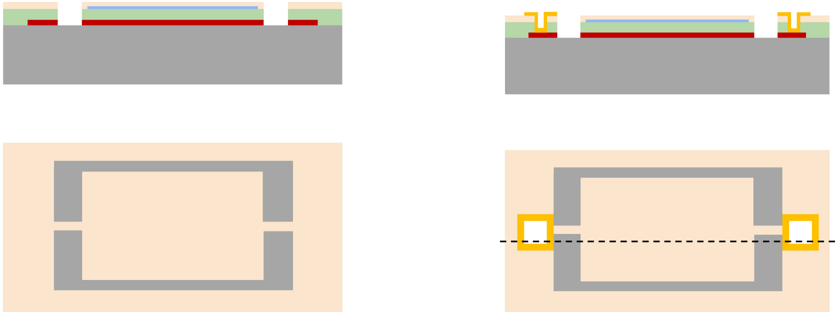

(e) Step 5: Dry etch for release pit.

(f) Step 6: Wet etch for vias followed by 100 nm-thick Au deposition for pads.

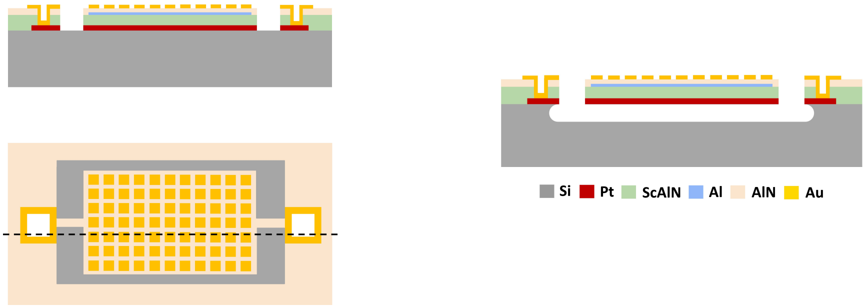

(g) Step 7: E-beam evaporation and lithography of 100 nm-thick Au patches.

(h) Final step: releasing.

Figure 4.8: Overall schematic illustration of the device after the main microfabrication process steps followed during the second batch: cross-section on top and top view on the bottom.

4.4 Experimental setup

The overall experimental setup proposed to efficiently characterize the system is shown in Figure 4.9 and consists of a low-power 4.53-μm QCL, free space-coupled to a compact long-path gas cell and a MEMS-CMOS IR detector. The QCL will turn on at the beginning of the sensing operation and remain on to continuously measure the N_2O concentration throughout the drone operation. The delivered IR power to the MEMS-CMOS IR detector will be attenuated as the IR beam passes through the long-path optical cell and is absorbed by the gas-specific IR absorption spectrum. The reduction in the available IR power will be detected by the MEMS-CMOS IR detector and translated into a corresponding concentration level. Moreover, a set of COTS sensors detecting temperature, humidity, and CO_2 concentration are included in order to perform the de-embedding of their contribution to the attenuation of the IR beam's power with respect to the one related to the N_2O concentration.

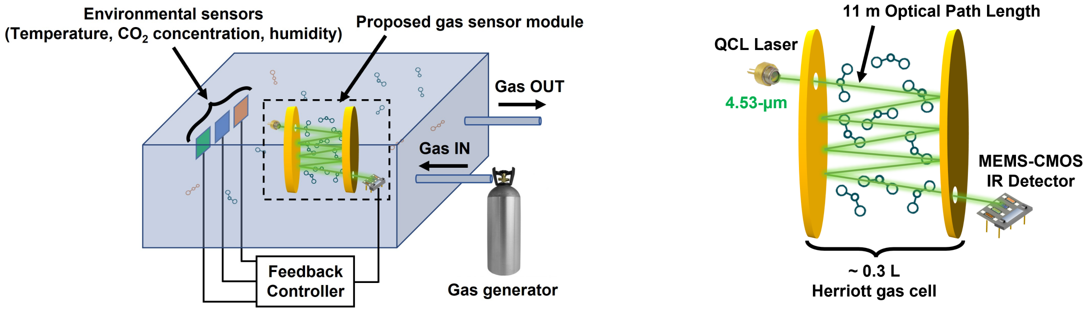

(a) Experimental setup. **(b)** Detailed gas sensor module.

Figure 4.9: Overall schematic illustration of the experimental setup.

Here in detail is described the experimental optical setup shown in Figure 4.10 that will be used to test the IR detection capabilities of the detector. A 4.53-μm QCL, collimated by an aspheric lens with an antireflection coating ensuring a reflectance lower than 1% at the operating wavelength, is used as an IR source. A dichroic filter is properly set up in a cage system to co-align a visible light beam from a red laser with the invisible QCL beam to facilitate the visual alignment between the QCL beam and the device under test inside the vacuum chamber (a proper alignment is needed to maximize the response of the detector). The cage system perfectly aligns the combined red-IR beam with the entrance of the gas cell and a flat reflective mirror mounted at the exit of the gas cell on a 3-axis linear translation stage is used to align the device placed inside the vacuum chamber to the red laser spot. The frequency response of the device under test, upon exposure to the QCL radiation modulated by the gas mixture contained in the gas cell, will be continuously monitored using a vector network analyzer (VNA) to which the detector will be connected through RF probes landed on the pads of the device from the inside of the vacuum chamber. It is worth noting that this optical setup is built on a small portable optical breadboard mounted together in such a way that all the optical elements are around a central hole through which the beam can pass and reach the CaF_2 window of the vacuum chamber.

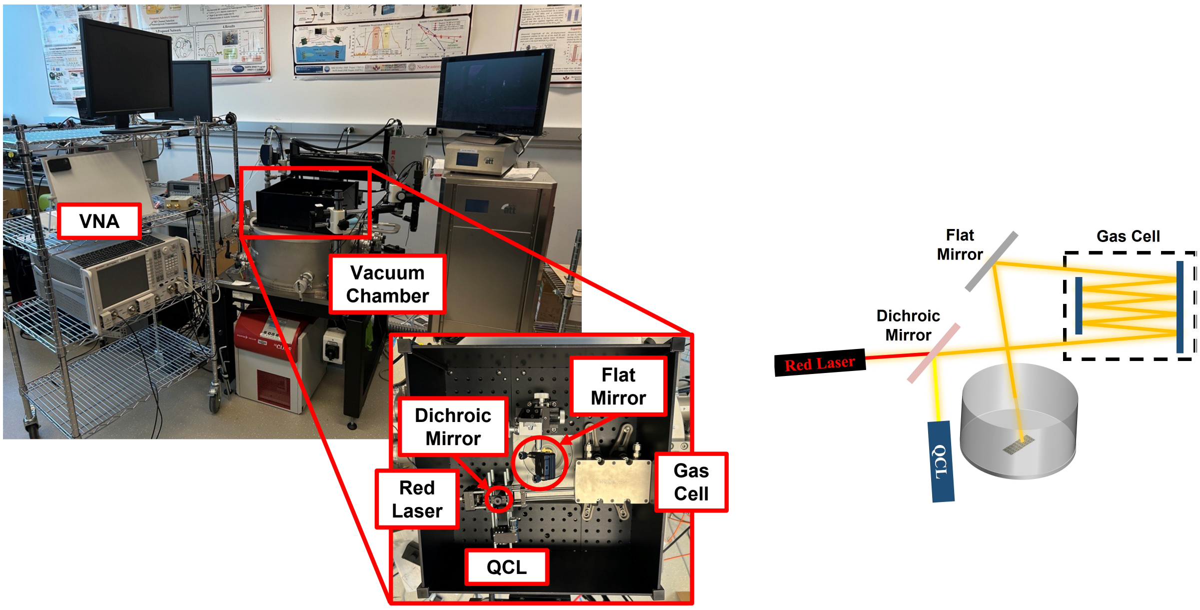

(a) Overall experimental setup. **(b)** Working principle of the optical setup.

Figure 4.10: Experimental IR testing optical table setup with a commercial QCL: a dichroic filter is properly set up in a cage system to co-align a red laser beam with the QCL collimated beam to facilitate the visual alignment with the device placed inside the vacuum chamber (the red laser is ON during the alignment and OFF during IR testing). The cage system perfectly aligns the combined red-IR beam with the entrance of the gas cell and a flat reflective mirror mounted at the exit of the gas cell on a 3-axis linear translation stage is used to align the device placed inside the vacuum chamber to the red laser spot.

The gas flow system needed to pump the desired gas mixture in the gas cell of the previously described experimental setup was designed, as shown in Figure 4.11. In particular, temporarily neglecting the interference to the N_2O measurement coming from the CO and H_2O, a system able to provide the targeted mixing ratio of N_2O and CO_2 molecules is presented:

- a tank for each gas to be provided is placed at the inlet of the gas flow system. Pure N_2O acts as a diluent, while the starting mixing ratio of the gas inside the other two tanks varies according to their final concentration to be achieved in the mixing chamber;
- a regulator is inserted at the outlet of each tank to lower the pressure of the exiting gas flow since the pressure inside each tank exceeds the maximum pressure that the mass flow controller can withstand;
- only the regulator connected to the N_2O tank is followed by a check valve blocking the possible flux of the other gases towards the N_2O tank in order to avoid the contamination and so the variation of the extremely low nominal mixing ratio of the N_2O tank;
- the flow rate of each gas is accurately set by a mass flow controller characterized by a certain range of tunable flow rates in order to achieve the targeted mixing ratio of molecules in the mixing chamber;
- a mixing chamber, where the flow of each gas converges by means of a four-union. The main aim of the mixing chamber is to monitor the achieved mixing ratio before making it go inside the gas cell by measuring the concentration of N_2O and CO_2 with commercial sensors placed inside;

- a gas cell, where the detection of the calibrated N_2O concentration is performed by means of the proposed sensor.

All the tubing is chosen to be chemically compatible with the involved gases.

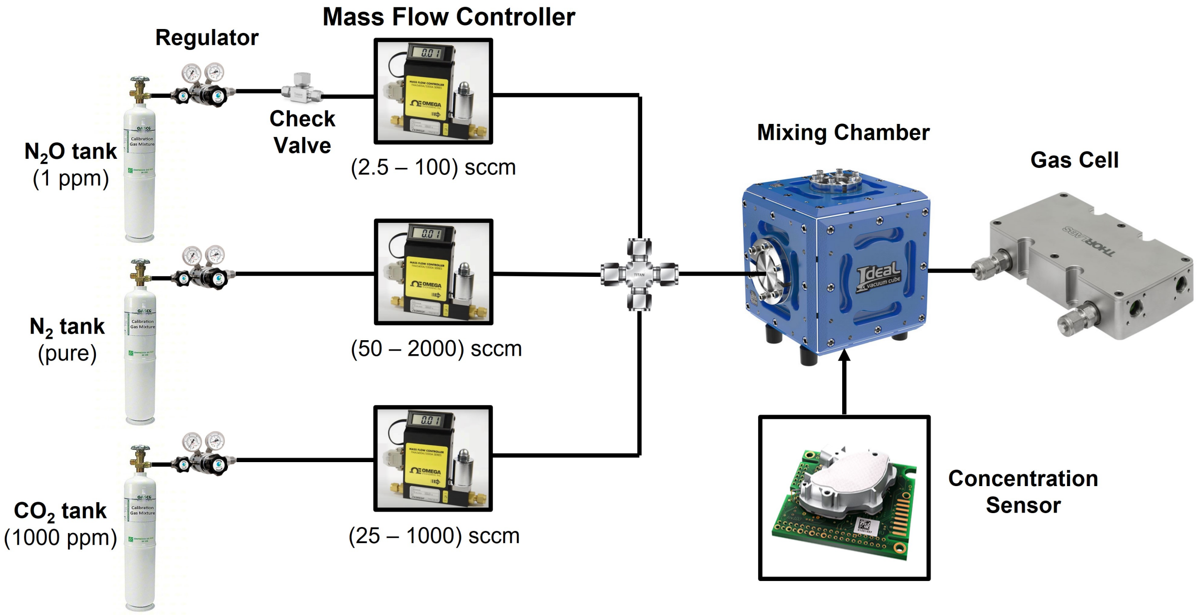

Figure 4.11: Experimental setup for the gas flow system needed to pump the targeted mixing ratio of molecules in the gas cell.

Chapter 5

Results

The previous sections of the thesis have extensively described the operating principle of the system from a purely theoretical standpoint, the methods used to identify its specifications, the steps followed to fabricate its core, and the experimental setup needed to test its correct functioning. This final section consists first of the critical analysis of the results obtained through PYTHON and MATLAB numerical simulations that have led to the first design of the system. Then the first experimental proof of the single sub-parts of the system is presented.

5.1 Design: numerical simulations

5.1.1 Gas cell

5.1.1.1 Optimal wavelength

The first analysis that has been carried out is related to the selection of the optimal operating wavelength according to the interference in the detection of N_2O produced by the absorption spectrum overlap with other molecules whose absorption lines are significantly high in a spectral region around the operating wavelength.

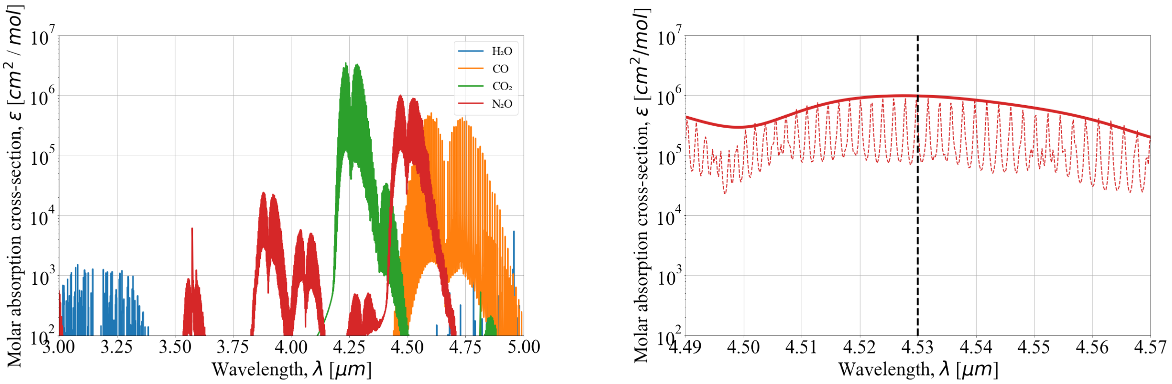

(a) MWIR absorption spectra of N_2O, CO_2, CO, and H_2O.

(b) MWIR absorption spectra of N_2O around 4.53 μm.

Figure 5.1: MWIR absorption spectra of gases involved in the operating wavelength region from HITRAN database.

To this aim, the MWIR absorption spectrum of N_2O, i.e. the target molecule, together with the one of all the other molecules whose absorption spectrum lies near the N_2O one, has been explored. Figure 5.1a clearly demonstrates how the closest molecules with the highest absorption values are CO_2 and CO, together with H_2O. In particular, the spectrum of both CO_2 (centered around 4.3 μm) and CO (centered around 4.7 μm), is partly overlapped with the one of N_2O (centered around 4.5 μm), thereby giving rise to the possibility of interference and so error in the N_2O concentration measurement. Moreover, the absorption spectrum of H_2O acts as a background all over the considered spectral range.

Their overlap has been quantitatively investigated to find an optimal value of the QCL's emission central wavelength able to minimize the interference and so the measurement error of N_2O concentration induced by the absorption coming from non-targeted background gases. In particular, according to equation 3.1, a rough estimation of the specific central wavelength able to simultaneously maximize the sensitivity of the system to the variation of N_2O concentration and minimize the one related to CO, H_2O, and CO_2 can be obtained dividing the variation of the laser power exiting the gas cell P_{out} due to an infinitesimally small variation of N_2O concentration c_{N_2O} by the one due to an infinitesimally small variation of CO_2, CO, and H_2O concentration. It can be demonstrated that this ratio can be approximated to the one of the molar absorption cross-sections if the optical path length l is sufficiently short (as in the condition where the system will be used):

$$\lim_{l \to 0} \frac{\frac{\partial P_{out}}{\partial c_{N_2O}}}{\frac{\partial P_{out}}{\partial c_i}} = \frac{\varepsilon_{N_2O}}{\varepsilon_i} \qquad \forall i = CO_2, CO, H_2O \tag{5.1}$$

Figure 5.2a shows the ratio between the N_2O absorbance and the CO_2, CO, and H_2O ones. This approach led to three preliminary optimal emission central wavelengths, i.e. the ones that maximize the ratio of N_2O absorbance with respect to the one of each of the interfering molecules, which turned out to be 3.88 μm, 4.46 μm, and 4.53 μm for CO, H_2O, and CO_2. In particular, Figure 5.1b demonstrates that the second highest peak of the N_2O absorbance is centered at 4.53 μm.

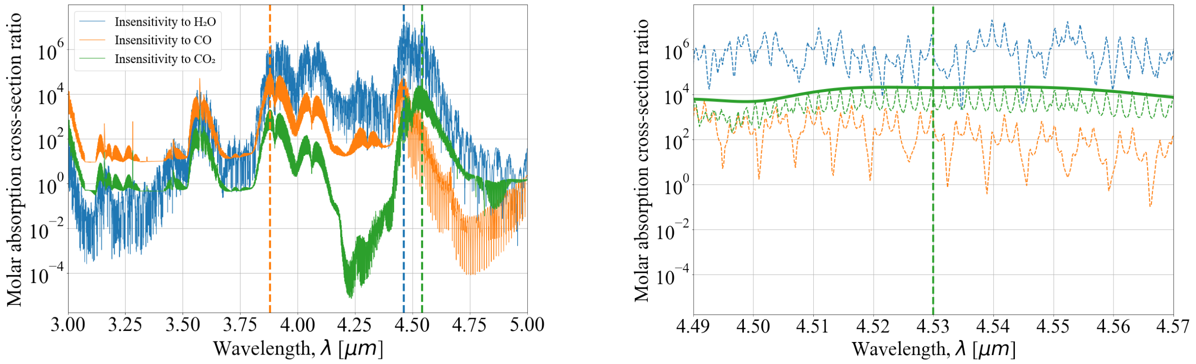

(a) MWIR absorption spectra ratio of N_2O with respect to CO_2, CO, and H_2O.

(b) MWIR absorption spectra ratio of N_2O with respect to CO_2, CO, and H_2O around 4.53 μm.

Figure 5.2: MWIR absorption spectra ratio of N_2O with respect to interfering background gases in the operating wavelength region from HITRAN database.

In order to quantify this interference and so the error to which it leads, an extensive literature review first led to finding the worst possible concentration range of all the interfering molecules in order to find their average concentration and the worst-case-scenario in terms of variation of their concentration:

- the trend of the average CO_2 concentration in the USA shown in [76] illustrates how, nowadays, the level turns out to be around 400 ppm. However, this value varies in crop fields, daily and periodically throughout the growing season due to the photosynthesis and autotrophic respiration of plants, and heterotrophic respiration of soil [77], leading to a worst-case fluctuation of CO_2 concentration around $\pm$ 100 ppm;
- the global background concentrations of CO range between 50 ppb and 120 ppb [78]. Therefore, in the absence of particular events and far from the big cities, its average concentration is around 85 ppb and this value varies moderately with a worst-case fluctuation in the order of $\pm$ 35 ppb in the crop field due to human activities, including engines and fuel combustion;
- the H_2O average concentration and worst-case fluctuation have been derived by a study about the most and least humid cities in the USA [79]. It can be seen as the relative humidity ranges from 90% to less than 40%. Therefore, the chosen worst-case range is 20 - 90 % RH with an average of 55 % and a fluctuation of $\pm$ 35%, which translates into a maximum water vapor concentration change of $\pm$ 6000 ppm.

In conclusion, since both the variation of CO_2 is much higher than the one of CO and the absorption coefficient of H_2O is significantly lower than the one of CO_2, the main source of interference among all the non-targeted background gases is considered to be CO_2. Therefore, the optimal emission central wavelength has been chosen to be 4.53 μm, i.e. the one ensuring the most effective insensitivity of the N_2O concentration measurement with respect to CO_2 interference. In particular, Figure 5.2b demonstrates that the ratio between the absorbance of N_2O and CO_2 is almost constant around 4.53 μm.

Once the optimal laser emission wavelength has been selected, in order to quantify the effect of the fluctuation of all these interference sources on the measured N_2O concentration, the change of transmitted IR power generated by 1 ppb variation in N_2O concentration was compared to the change of transmitted IR power due to the worst-case fluctuation of each source of interference. In particular, Figure 5.3a shows that a worst-case fluctuation of 100 ppm in the concentration of CO_2 leads to a variation of transmittance higher than the one due to a variation equal to 1 ppb of N_2O concentration. Therefore, compensation is needed by using a commercial NDIR sensor [20] whose accuracy can be lowered from 30 up to 3 ppm through appropriate environmental corrections for sensitivity to temperature, pressure, and relative humidity [80]. Concerning the component to the interference arising from the CO concentration fluctuations, Figure 5.3b illustrates that a compensation system for the variation of CO concentration during the operation of the sensor is not strictly required because a worst-case fluctuation of 35 ppb in the concentration of CO leads to a variation of transmittance lower than the one due to a variation equal to 1 ppb of N_2O concentration. On the other hand, Figure 5.3c demonstrates how the variation of transmittance due to the worst-case fluctuation equal to 35% of relative humidity is higher than the one due to the 1 ppb variation of N_2O. This means that also in this case it is necessary to compensate for this interference component by using a commercial humidity sensor able to achieve an accuracy of 1% RH [68].

Additionally, a further source of interference in the detection of N_2O is the temperature. In particular, it affects the performance of the sensor from a double standpoint:

- temperature changes the absorption spectrum of molecules;
- a change of environmental temperature induces a shift of the resonance frequency of the resonator that is not due to the laser power absorbed by the plasmonic absorber.

Therefore, it is important also to establish a suitable temperature range which is the most common for crop growth. It turns out to be from 10 to 40 °C, but Figure 5.3d shows that a variation of temperature from the ambient temperature towards both the upper and lower bound of this range induces a change of transmittance higher than the one due to the 1 ppb variation of N_2O. Therefore, also in this case, compensation is needed and it can be achieved by using a commercial temperature sensor with an accuracy of 0.1 °C [68].

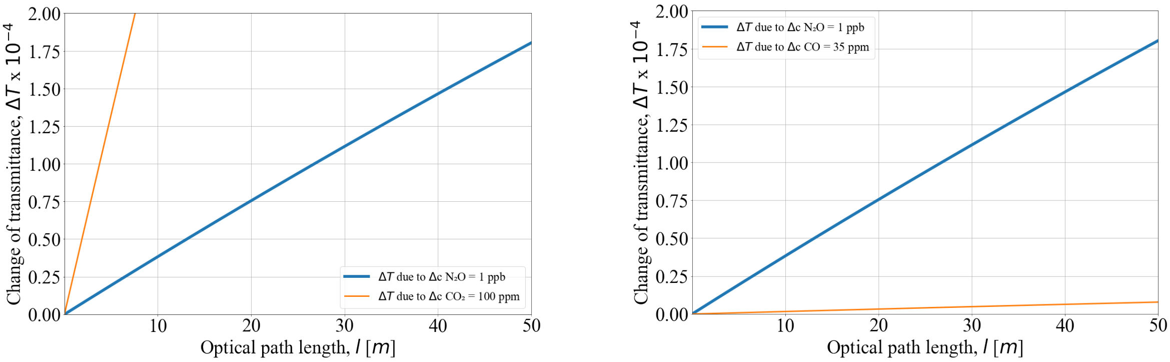

(a) Change in transmittance due to CO_2 fluctuations between 300 and 500 ppm with respect to the average value of 400 ppm.

(b) Change in transmittance due to CO fluctuations between 50 and 120 ppb with respect to the average value of 85 ppb.

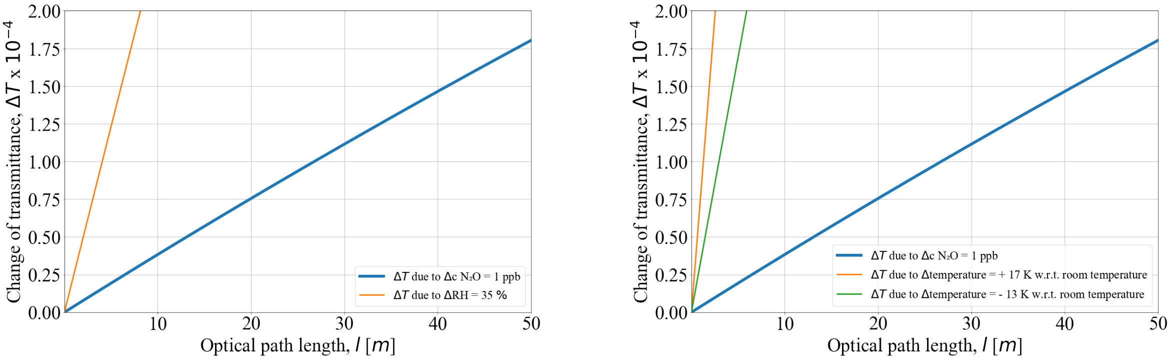

(c) Change in transmittance due to humidity fluctuations between 20 and 90 % with respect to the average value of 55%.

(d) Change in transmittance due to temperature fluctuations between 10 and 40 °C with respect to an average ambient temperature of about 23°C.

Figure 5.3: Comparison between the chance in transmittance due to 1 ppb variation of N_2O concentration and the one due to the worst-case fluctuation of all the interference sources.

In conclusion, combining all the sources of interference and considering the minimum accuracy achievable with commercial sensors, the change of transmittance due to all of them is equivalent to the one due to less than 1 ppb variation of N_2O, specifically $\sim \pm$ 0.48 ppb, thereby leading to an SNR slightly larger than 2. Therefore, in this way, it has been demonstrated that, despite all these sources of interference, the proposed system is still able to theoretically achieve the goal of 1 ppb detection sensitivity of N_2O.

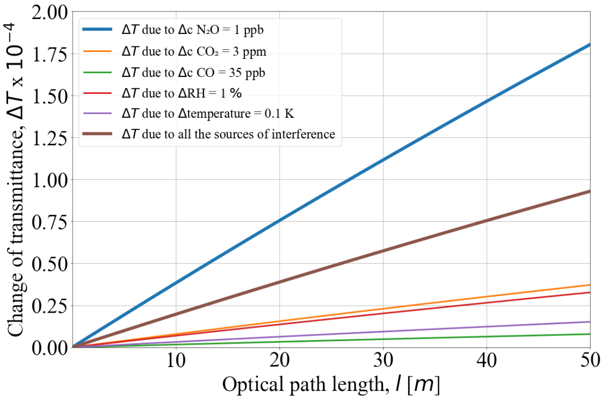

Figure 5.4: Comparison between the change in transmittance due to 1 ppb variation of N_2O concentration with respect to the one due to each source of interference and all of them together.

Moreover, during its operation, the laser tends to heat up and this leads to a shift of its central emission wavelength. In particular, from the datasheet of the used commercial QCL [69], it is possible to retrieve that the typical excursion of the emission central wavelength as a function of its temperature is not wider than 40 nm for a temperature range from 20 to 40 °C. Therefore, in order to check the insensitivity of the system to the variation of the internal temperature of the used commercial QCL, the change in transmittance due to 1 ppb variation of N_2O concentration as a function of the wavelength has been normalized to the one at the previously chosen one, i.e. 4.53 μm. This study allows to roughly estimate the 3 dB bandwidth of the sensitivity due to the laser emission central wavelength excursion. Figure 5.5 shows that it is nearly 50 nm, i.e. larger than the typical excursion of the emission central wavelength presented in the datasheet for a temperature range from 20 to 40 °C, even taking into account the bandwidth of the emission spectrum of the used commercial QCL, which has been roughly estimated to be not larger than 3 nm from its datasheet.

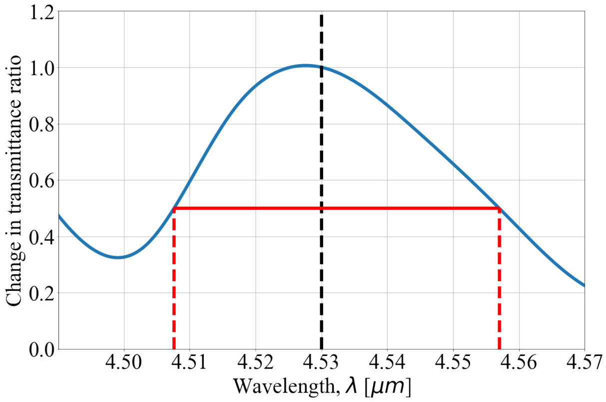

Figure 5.5: Normalized change in transmittance due to 1 ppb variation of N_2O concentration.

In conclusion, this analysis converged to a laser emission central wavelength of 4.53 μm based on the maximization of the system sensitivity, as well as its tolerance to multiple varying interfering parameters.

5.1.1.2 Other interference sources

Other sources of interference arise from the drone operation. In particular, it leads to:

- vibrations, which can derive from both:
    - motors and propeller blades, which can be modeled as a vibration of frequency comprised between 10 and 70 Hz [81], and whose effect can be reduced by maintaining the drone speed constant;
    - the interaction between the drone and the airflow, which can be modeled as a vibration of frequency comprised between 2 and 10 Hz [81], and whose effect depends on air turbulence and weather, thereby being conditions that cannot be controlled.

  However, in general, vibrations do not represent a high risk for the proper operation of the readout circuit, but they can induce misalignment between the laser beam and the detector due to the vibrations that are transferred to the optical system, i.e. the mirrors used to build the optical cavity and the laser mounting system. Therefore, in order to minimize this risk, the laser beam diameter will be maximized together with the stiffness of the mounting system of both the laser and the mirrors. Moreover, a system of dashpots will be designed in order to isolate as much as possible the whole sensing system with respect to the drone platform. To this aim, an analysis of the misalignment tolerances with respect to the trajectory the laser follows in the optical cavity has been performed in section 5.1.1.4.

- airflow problems and, in particular, to a low air exchange between the external environment to be analyzed and the gas cell, which can cause problems and untrue measurements. The best way we have identified to minimize this further risk is using an open gas cell. Moreover, the airflow generated by the drone's propellers could also prevent the environmental atmosphere to enter the gas cell or lead to its alteration. This is the reason why the whole sensing system will be mounted far enough from the propellers by means of a system of long cables.

5.1.1.3 Optimal optical path length

In order to quantify the minimum optical path length required to achieve the predetermined sensitivity goal, which is a minimum detectable variation of N_2O concentration $\Delta c_{N_2O_{min}}$ equal to 1 ppb, some reasonable assumptions have been considered based on a literature review of gas detectors relying on the same detection principle, as well as datasheets of commercially available lasers:

- plasmonic absorber area equal to 100 x 100 μm^2;
- minimum variation of the impinging optical IR power $\Delta Q_{IR_{min}}$ detectable by the plasmonic absorber equal to 20 nW;
- laser beam diameter equal to 1 mm;
- IR optical power emitted by the laser entering the gas cell P_{in} equal to 20 mW and uniformly distributed over the entire area of the laser beam's cross-section so that just a fraction is the one impinging the plasmonic absorber.

In fact, knowing that:

$$\Delta Q_{IR_{min}} = \Delta c_{N_2O_{min}} \cdot \left| \frac{\mathrm{d}P_{out}}{\mathrm{d}c_{N_2O}} \right| \cdot \frac{A_{absorber}}{A_{beam}} = \Delta c_{N_2O_{min}} \cdot P_{in} \left| \frac{\mathrm{d}T}{\mathrm{d}c_{N_2O}} \right| \cdot \frac{A_{absorber}}{A_{beam}}, \tag{5.2}$$

where T is the transmittance defined by equation 3.1, then $\Delta c_{N_2O_{min}}$ can be plotted as a function of the optical path length l:

$$\Delta c_{N_2O_{min}} = \frac{\Delta Q_{IR_{min}}}{P_{in} \left| \frac{\mathrm{d}T}{\mathrm{d}c_{N_2O}} \right|} \cdot \frac{A_{beam}}{A_{absorber}}, \tag{5.3}$$

where

$$\left| \frac{\mathrm{d}T}{\mathrm{d}c_{N_2O}} \right| = l \cdot \epsilon_{N_2O} \cdot \ln(10) \cdot 10^{-A} = l \cdot \epsilon_{N_2O} \cdot \ln(10) \cdot 10^{-l \sum_i \epsilon_i c_i}. \tag{5.4}$$

Therefore, assuming a laser central emission wavelength equal to 4.53 μm, i.e. the optimal value explained in the previous section, the necessary minimum optical path length turns out to be equal to about 20 m, as shown in Figure 5.6.

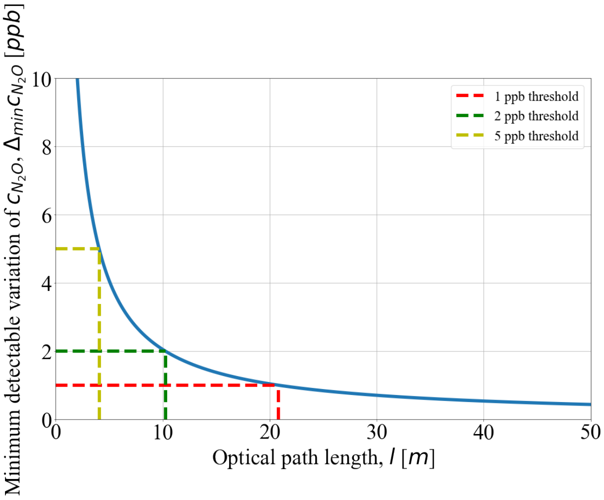

Figure 5.6: Minimum optical path length necessary to achieve a 1 ppb (20.80 m), 2 ppb (10.25 m), and 5 ppb (4.06 m) sensitivity.

In particular, equation 5.4 shows a double dependence of $\Delta c_{N_2O_{min}}$ on the optical path length l:

- linear decreasing, whose contribution dominates at short l, since the system's sensitivity increases with the optical path length due to increasing interaction length between the laser beam and the molecules to be detected;
- exponential increasing, whose contribution dominates at long l, since the transmitted power becomes no longer detectable.

Therefore, also in this case, the optimal optical path length l ensuring the smallest minimum detectable variation of N_2O concentration has to be found as a trade-off between these two contributions and, in particular, before that the exponential contribution matters. Figure 5.7a shows the same graph as Figure 5.6, but over a wider x-axis scale, so that the contribution at longer l is now visible. It follows the same trend as Figure 5.7b, which shows the intrinsic sensitivity of the system, i.e. its transfer function $\left| \frac{\mathrm{d}P_{out}}{\mathrm{d}c_{N_2O}} \right|$

equal to P_{in} that multiplies equation 5.4, passing from a linear increasing to a sublinear one up to a saturation followed by a decreasing of performance for too long optical path lengths.

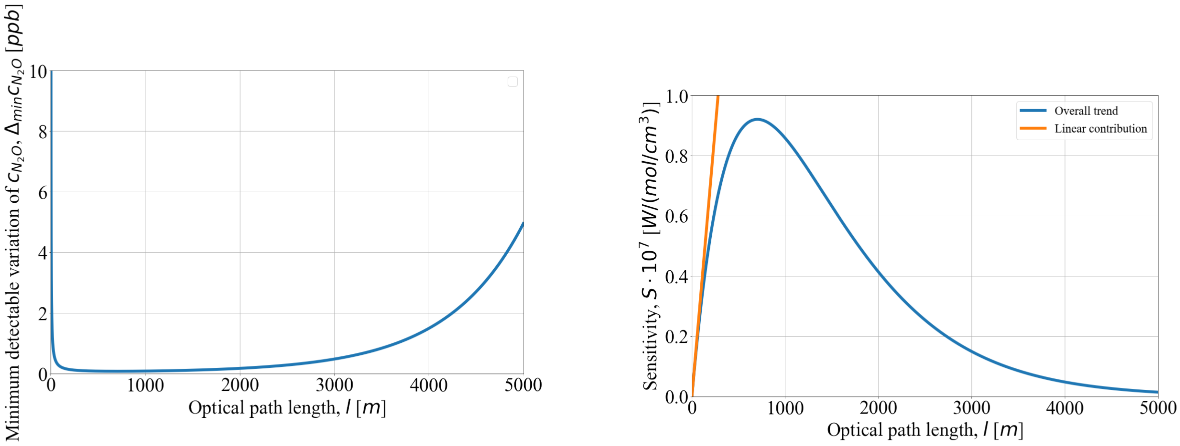

(a) Minimum detectable variation of N_2O concentration. **(b)** Transfer function of the gas cell.

Figure 5.7: Graphs up to an optical path length of 5 km to show the contribution of all the l-dependent factors.

5.1.1.4 Mirrors

A customized Herriott gas cell has been designed to have an open system with an optical path length that can be tuned according to the number of reflections and the distance among the spherical mirrors in order to achieve the goal of the project in terms of sensitivity. Moreover, also the volume can be tuned according to the distance among the mirrors and optimized in order to fulfill the related point in the SWaP requirements.

A schematic representation of the designed Herriott cell is shown in Figure 5.8. It consists of two facing highly reflective spherical mirrors with a common optical axis. A hole is machined into one of the mirrors, called *near mirror*, to allow the input beam coming from the QCL to enter the cavity. Another hole is machined in the opposite mirror, called *far mirror*, to allow the output beam pointing towards the sensor to exit the cavity.

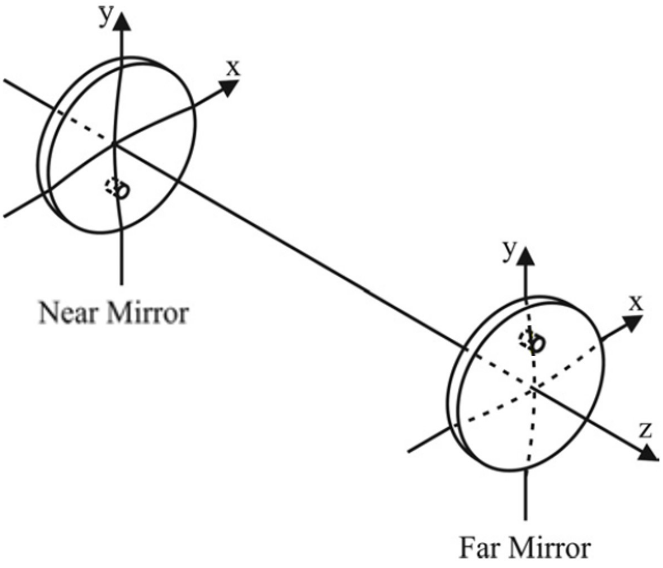

Figure 5.8: Schematic representation of the Herriott cell.

Therefore, in order to properly design the Herriott gas cell, the analytical model described in section 3.1.2 has been used and an example of the results obtained by running it is presented in Figure 5.9. Considering the specifics of some mirrors commercially available that have been used for the experimental demonstration described in section 5.2.1, i.e. diameter of 5.08 cm, focal length of 200 mm and reflectivity not lower than 98% in the wavelength range between 2 and 20 μm, and placing them at a distance of 14 cm to not exceed the volume limitation of 0.3 L set by the SWaP requirements, a maximum number of 79 reflections can be theoretically achieved by placing the entrance and exit holes, which have a diameter of 4 mm, in the positions shown in Figure 5.9 (the green and the blue spot represent the entering and exiting points, whose coordinates are equal to around (0.84, 1.82) cm and (1.96, 0.44) cm, respectively). The maximum number of reflection points is set by the fact that, if exceeded, the beam starts to retrace its path, known as *re-entrant condition*, thereby causing interference problems and exiting the cell from the entrance hole. In particular, Figure 5.9 shows the points where the beam is going to reflect on each mirror and it demonstrates that the distance among the spots on the same mirror is around 2 mm, i.e. larger than the beam size, thereby avoiding any type of interference during the multiple reflections. This pattern is obtained when the laser beam enters the Herriott gas cell with an inclination angle equal to around - 6.85° and 0° on the xz and yz plane, respectively.

Moreover, assuming that the entering beam has a circular shape with a diameter equal to 1 mm, the model is also able to show how the beam size evolves during the multiple reflections and, in particular, how its size increases as the beam reflects farther from the x-axis, i.e. for increasing y coordinate. In fact, since the incident beam is not an ideal ray, but it has a finite diameter, a cluster of parallel rays circularly surrounding a central ray has been used to simulate a beam with a certain diameter so that the outline of the cross-section of this cluster of rays defined the spot shape. Therefore, by tracing each ray of this cluster individually, the evolution of the beam size during the multiple reflections can be analyzed. This analysis has been very important for the final application because spherical mirrors' aberrations typically lead to a circular spot with a crescent size that can cause overlap between two neighboring spots and so to interference.

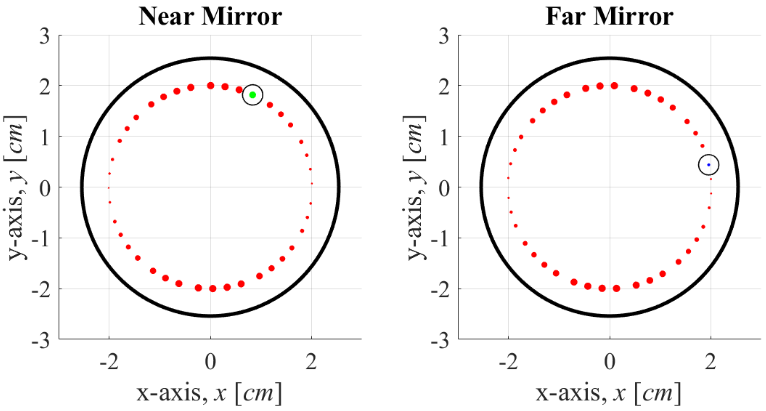

Figure 5.9: Reflection pattern on the mirrors and beam size evolution.

This setup allows to achieve of an overall optical path length close to 11 m with 79 passes, but, considering the worst-case scenario of the lowest reflectivity ensured by the vendor equal to 98%, the 80% of the optical power entering the cell is lost, thereby decreasing the sensitivity of the system. This means that a trade-off between optical path length and mirror losses must be also taken into account to finally fulfill the required sensitivity target. In fact, the power exiting the gas cell P_{out} is subjected to a reduction with respect to the entering one P_{in} due to, not only the absorbance A of the molecules in between the mirrors but also the mirrors' losses:

$$P_{out} = P_{in} \cdot R^{N-1} \cdot 10^{-A} = P_{in} \cdot R^{N-1} \cdot 10^{-dN \sum_i \epsilon_i c_i}, \tag{5.5}$$

where R is the reflectivity of the mirrors, N is the number of reflections, and d is the distance between the mirrors. Therefore, a further contribution has to be added to the calculation of the minimum detectable variation of N_2O concentration. In particular, this contribution is strongly dependent on the value of the reflectivity of the used mirrors, and Figure 5.10 shows how it is stronger than the exponential one mentioned in section 5.1.1.3 at shorter optical path lengths, thereby preventing the achievement of a sensitivity of 1 ppb, even using mirrors that ensure a reflectivity not smaller than 99.5 %. This means that, for the final application, mirrors that guarantee even higher reflectivity, like dielectric mirrors, are needed.

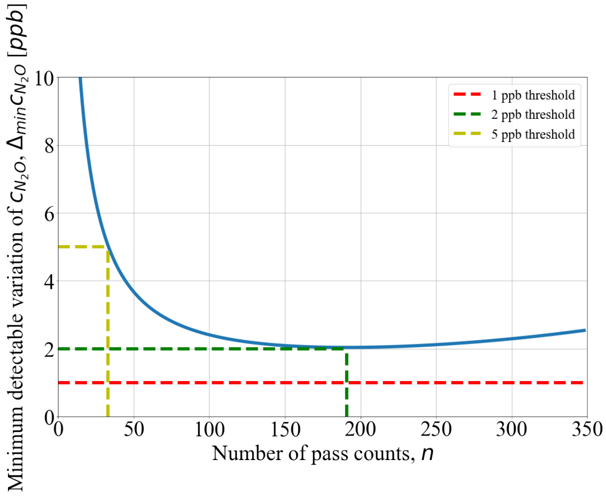

Figure 5.10: Minimum optical path length necessary to achieve a 1 ppb (not achievable), 2 ppb (26.74 m, i.e. 191 reflections among two mirrors spaced by a 14 cm distance) and 5 ppb (4.62 m, i.e. 33 reflections among two mirrors spaced by a 14 cm distance) sensitivity taking into account the mirror losses of mirrors with reflectivity equal to 99.5 %.

Finally, the variability of the reflection pattern on the mirrors with respect to the entering parameters has been studied in order to understand the alignment tolerances the overall system has to satisfy to guarantee the correct operation when subjected to the vibrations due to the drone flight. In particular, a Monte Carlo simulation has been set in order to assess the effect of such uncertainty. Figure 5.11a and Figure 5.12a show how the pattern changes if the entering coordinates and inclination angles are subjected to a variability modeled as a Gaussian distribution with the mean equal to the ideal values previously mentioned and the standard deviation of 0.25 mm and 0.1°, respectively. Specifically, Figure 5.11b and Figure 5.12b the standard deviation of the beam's position on the mirrors due to the variability of coordinates and inclination angles are both characterized by a periodic evolution where the minimum is achieved in the reflection points close to the x-axis, i.e for a y coordinate around 0, and to the straight line traced by joining the entering position with the center of the mirror, respectively. Finally, Figure 5.13 demonstrates that the reflection pattern is still distinguishable even after combining these two contributions of variability because each of them dominates in different positions of the mirror, thereby achieving an overall standard deviation that is almost constant but not as large to compromise the proper operation of the system, i.e. the interference among the reflecting beams.

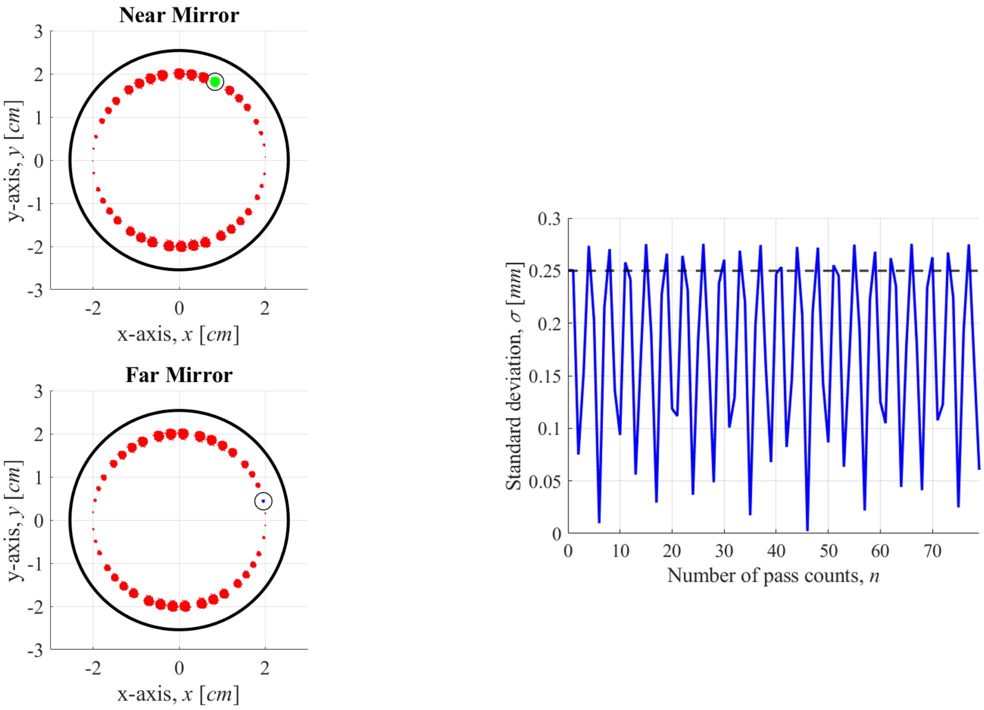

(a) Reflection pattern. **(b)** Standard deviation evolution.

Figure 5.11: Effect of the variability on the beam's entering coordinates.

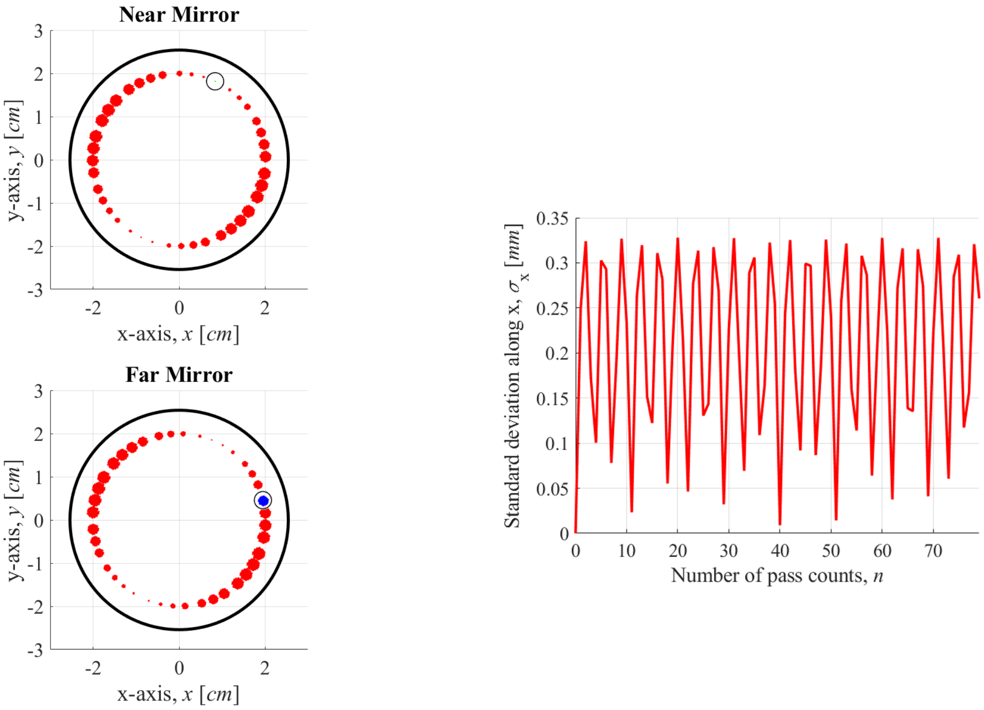

(a) Reflection pattern. **(b)** Standard deviation evolution.

Figure 5.12: Effect of the variability on the beam's entering inclination angles.

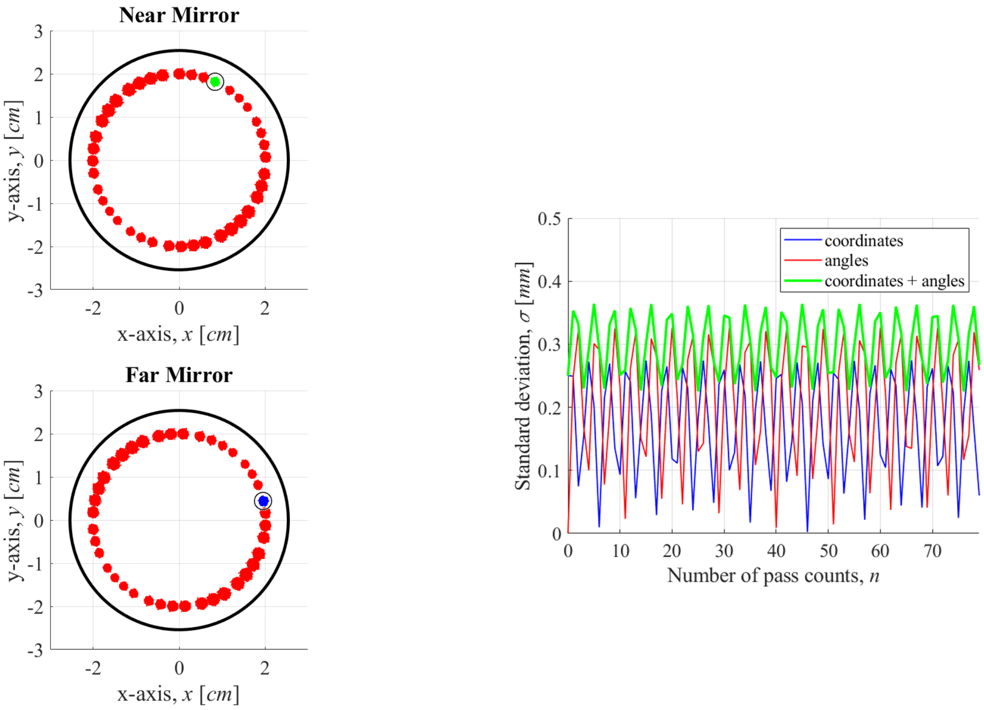

(a) Reflection pattern. **(b)** Standard deviation evolution.

Figure 5.13: Effect of the variability on both the beam's entering coordinates and inclination angles.

5.1.2 Plasmonic absorber

The optimization of the plasmonic absorber to tailor the absorption peak at $\sim 4.53\ \mu m$ for N_2O gas sensing was performed using the analytical model described in section 3.2.1 before and Finite Integration Technique (FIT) with the commercial software CST after.

Different dielectric materials to be used as spacer have been investigated to find an optimal trade-off between:

- the overall *temperature coefficient of frequency* TCF and so the *responsivity* R of the sensor according to equation 3.13;
- the overall *thermal capacitance* C_{th} and so the *thermal time constant* τ according to equation 3.19;

of the whole resonant body (i.e. actual piezoelectric resonator and the plasmonic absorber integrated on top).

Table 5.1, shows the values of the investigated material's parameters affecting the aforementioned trade-off, together with the *mass density* ρ due to the mass loading effect induced by the integration of the plasmonic absorber on top of the actual piezoelectric resonator.

Dielectric material	***TCF***	***c [J/(kg · K)]***	***ρ [kg/m^3]***
SiO_2	positive	700	2400
SiN	negative	890	2800
AlN	negative	800	3200

Table 5.1: Material properties involved in the selection of the dielectric spacer material (average values from [82]).

The analytical model of the plasmonic absorber was firstly run to find the optimal values of the geometrical parameters. The thickness (100 nm) and material (Au) of both the bottom ground layer and the top cross-shaped patches were kept constant. Three different dielectric materials, SiO_2, SiN, and AlN, were investigated and so three different sets of values (see Table 5.2), were found for each of them to center the peak of the absorption efficiency spectrum at the optimal laser emission central wavelength of 4.53 μm because of their different dispersion of the relative electric permittivity. In particular, the values adopted for the dispersion of the complex relative electric permittivity for both the dielectric and metal materials involved in the design are the ones extracted from the model developed by [83] and [84], respectively.

Dielectric material	***a [nm]***	***b [nm]***	***Λ [μm]***	***t [nm]***
SiO_2	150	1.42	3.5	200
SiN	150	0.84	3.5	300
AlN	150	1.01	3.5	250

Table 5.2: Optimal set of values for the tunable geometrical parameters obtained from the analytical model.

The thickness of the dielectric spacer, which is determined by the relative electrical permittivity, affects the final volume of the resonant body and so its thermal capacitance. As the real part of the electrical permittivity increases (the average value over the operating wavelength range increases going through SiO_2, AlN, and SiN), the thickness of the dielectric spacer must also increase to keep the parallel-plate capacitance constant. This is the reason why, considering the different intrinsic material properties and assuming the same area of the plasmonic absorber, SiN provides the largest contribution to the overall thermal capacitance of the device due to both its highest specific heat capacity c and the largest thickness that is required for the correct operation of the device, even though its TCF is negative. On the other hand, the material typically used for this purpose according to the literature, i.e. the SiO_2, provides the smallest contribution to the overall thermal capacitance of the device due to both its lowest specific heat capacity c and the smallest thickness that is required for the correct operation of the device, but its TCF is positive, thereby partially compensating the negative TCF provided by the $ScAlN$ piezoelectric layer of the actual resonator and so reducing the overall sensitivity of the system (this is the reason that has led to the investigation of other materials). Therefore, as mentioned before, a trade-off is needed and, since the potential SiN layer could also be damaged during the final release of the device, thereby making its use incompatible with the whole fabrication process flow, AlN is the best option because, even if it provides a larger contribution to the overall thermal capacitance of the device than SiO_2, its TCF is negative, thereby boosting the overall TCF and sensitivity of the sensor, and it is fully compatible with the fabrication process flow. Moreover, even if AlN is denser than SiN, its smaller required thickness compensates also for this issue. Figure 5.14 shows the results in terms of peak wavelength, absorptance peak, and FWHM obtained from the analytical model using AlN as a dielectric layer and the values reported in Table 5.2 as geometrical parameters, which are 4.54 μm, 99%, and 115.6 nm, respectively.

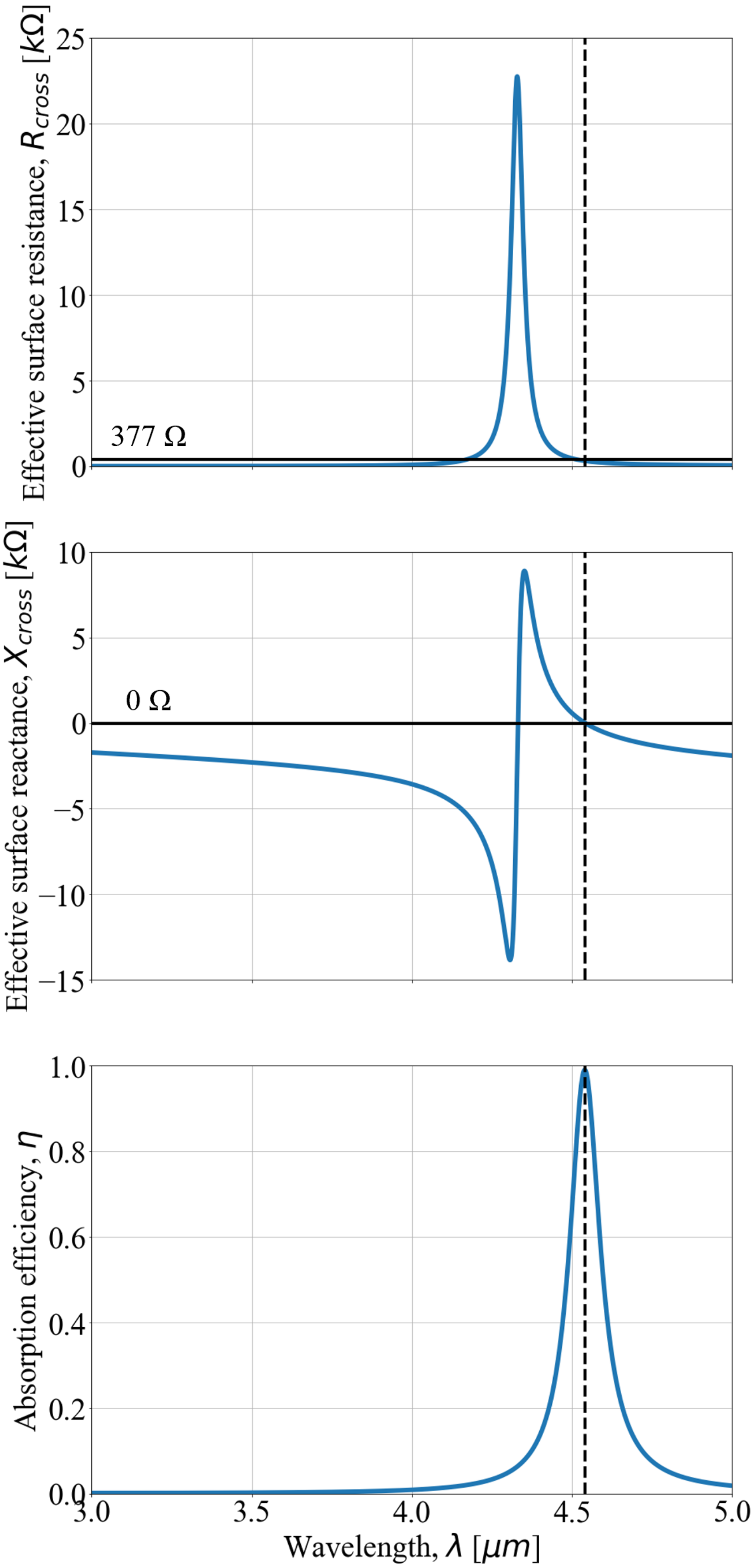

Figure 5.14: Results obtained from the analytical model for a plasmonic absorber with an AlN dielectric spacer and values of the geometrical parameters equal to the ones reported in Table 5.2. The position of the peak of the absorption efficiency is approximately where the resonance occurs, i.e. the wavelength at which the imaginary part of the effective surface impedance goes to 0 Ω, while its height depends on the mismatch of the real part of the effective surface impedance with respect to the characteristic impedance of the free space, i.e. 377 Ω.

After identifying the appropriate material through faster simulations using an analytical model, FIT simulations were run using a CST model and the previously found optimal values of the geometrical parameters to verify them. The results shown in Figure 5.15 only required a slight correction to one of the dimensions of the patches, specifically the length of the cross b. Additionally, the material of the bottom ground layer was changed from Au to Al to make the fabrication of the entire stack easier and with reduced stress (since Al is a softer material) without any significant variation of the absorption profile. Even with this change, only a small variation of b was needed to center the peak of the absorption spectrum as close as possible to 4.53 μm. In fact, since a thickness of 100 nm for the bottom metal layer is much larger than the penetration depth of both Au and Al, a significant variation in the device's behavior was not expected. Therefore, a simulated absorption efficiency close to 99.1% around 4.527 μm with a bandwidth of 236.31 nm has been obtained by just tweaking b from 1.01 μm to 1.03 μm. The only large discrepancy with respect to the analytical model is the wider bandwidth. However, the value computed by the FIT simulation can be considered still good enough for this application since the overall system includes a narrow-band light source like a QCL and not a wide-band one like a Light Emitting Diode (LED), thereby not affecting at all the selectivity of the measurement, which depends only on the bandwidth of the QCL that is two order of magnitudes smaller.

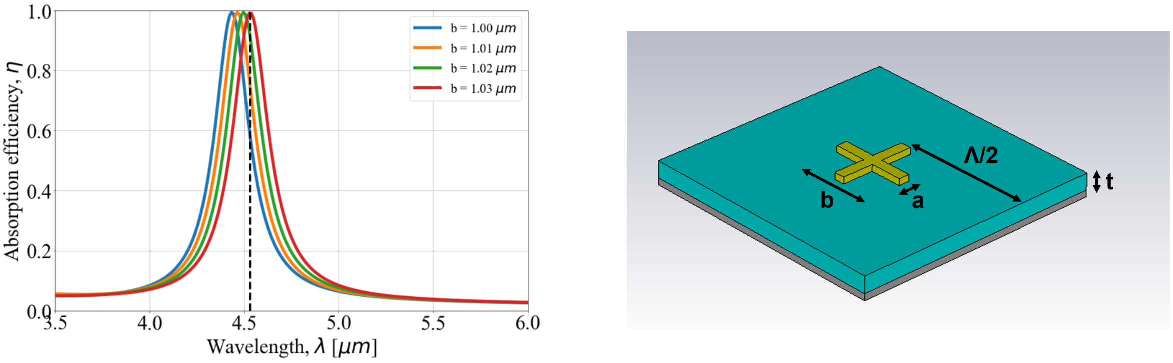

(a) Absorptance spectrum. **(b)** CST modeling with labeled geometrical dimensions.

Figure 5.15: CST simulation of cross-shaped patches.

In conclusion, the final stack of materials was chosen to be 100 nm of bottom Al reflector with 250 nm of AlN on top and 100 nm of Au for the patches. As shown in Figure 5.15, near 100% absorption η with a FWHM $\sim$ 240 nm can be achieved at a wavelength around 4.53 μm when the length b and the width a of the gold-patches are set to 1.03 μm and 150 nm, respectively, and their periodicity Λ to 3.5 μm.

However, for the first proof of concept of the device, square-shaped patches were fabricated keeping the same stack of materials, since they are theoretically less affected by the fabrication process variability. Therefore, simulations with this shape have been performed and they demonstrate a slight worsening of the performance in terms of absorption peak and bandwidth, as expected from equation 3.36 since a is equal to b and so it is larger than the cross-shaped patches. In particular, as shown in Figure 5.16, near 99 % (98.7 %) absorption η with a FWHM $\sim$ 250 nm (247.65 nm) can be achieved at a wavelength around 4.53 μm (4.538 μm) when the length b and the width a of the gold-patches are set both to 870 nm, respectively, and their periodicity Λ to 3.5 μm.

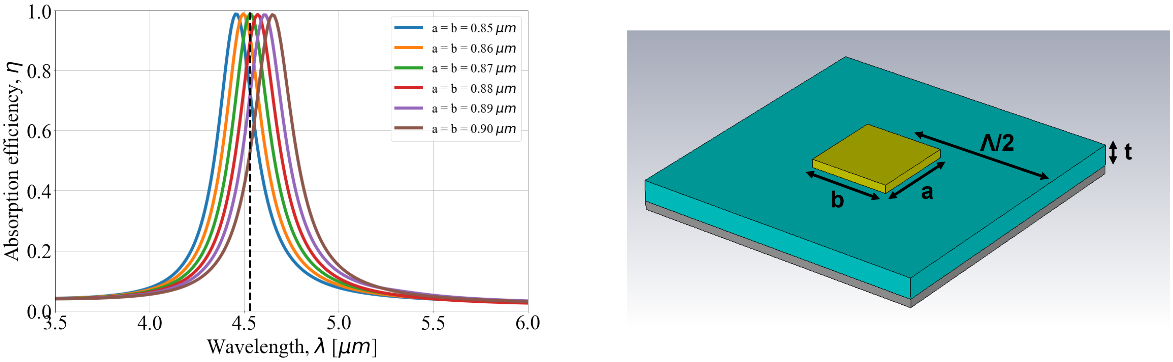

(a) Absorptance spectrum. **(b)** CST modeling with labeled geometrical dimensions.

Figure 5.16: CST simulation of square-shaped patches.

5.1.3 Laterally vibrating piezoelectric resonator

Three different piezoelectric materials commonly used to build resonators, i.e. AlN, $ScAlN$, and $LiNbO_3$, were investigated to maximize the *thermal conductivity* k and the TCF of the resonators and so improve the overall performance of the infrared sensor.

Table 5.3 shows the values of the aforementioned material's parameters, together with the d_{33} and d_{31} piezoelectric coefficients of the three materials under investigation. The 30%-doped $ScAlN$ has a significantly higher coupling coefficient for the acoustic mode of interest [85]. Moreover, $ScAlN$ and $LiNbO_3$ are comparable in terms of both TCF [86] and thermal conductivity, while AlN is characterized by both a lower TCF [87] and a higher thermal conductivity [88]. Since a higher TCF and a lower thermal conductivity yielding to a higher thermal resistance lead to a greater change in temperature and so to a better sensitivity of the sensor, AlN is discarded. However, even if $ScAlN$ and $LiNbO_3$ are comparable in their thermal properties, $LiNbO_3$ is highly anisotropic and $ScAlN$ has higher d_{33} and d_{31} piezoelectric coefficients. Therefore, $ScAlN$ was chosen for the piezoelectric material of the resonators.

Piezoelectric material	***TCF [ppm / °C]***	***k [W/(m · K)]***	***d_{33} [pm/V]***	***d_{31} [pm/V]***
AlN	- 25	122.8	5.7	- 2.5
$ScAlN$ (30 %)	-40	3.8	15	- 8
$LiNbO_3$	-86	5.6	6	- 1

Table 5.3: Material properties involved in the selection of the piezoelectric material.

Another important parameter that was investigated is the *thermal mass* of the device, which depends on the thickness and volume of the stack of materials of the resonant body. Reducing the thermal mass means reducing the thermal constant of the devices and so increasing the detection speed, thus enabling a higher sampling rate. To this aim, the resonator has been initially designed with a thin Pt bottom IDE of 50 nm, a 250 nm-thick $ScAlN$ piezoelectric layer, and a thin Pt top electrode of 50 nm, as shown in section 4.3.1. However, problems arose from the fabrication of this stack, leading to changes toward thicker layers (100 - 350 -100 nm as top electrode, piezoelectric material, and bottom interdigitated electrode stack) and Al instead of Pt as the top electrode in the second batch, as discussed in section 4.3.2. After choosing the materials and their respective thicknesses, the size and geometry of the devices were selected according to the resonance frequency to be achieved. In particular, since the frequency of operation is depending on the width and separation of the interdigitated bottom electrodes, a pitch size of

25 μm with a single finger width of 19 μm has been chosen so that a resonator with a resonance frequency in the 150 MHz range could be obtained as a trade-off between reducing the complexity of the read-out circuit design and reducing the complexity of the fabrication since larger devices are harder to release. These values were selected by performing 2D Finite Element Method (FEM) simulations in COMSOL. A $ScAlN$ model with doping-level dependent piezoelectric coefficients, mass density, and dielectric permittivity was used [89]. In particular, the lateral-extensional mode of vibration was visualized, while the electromechanical coupling and resonance frequency of the resonators were extracted. Figure 5.17 illustrates the results obtained from the simulations.

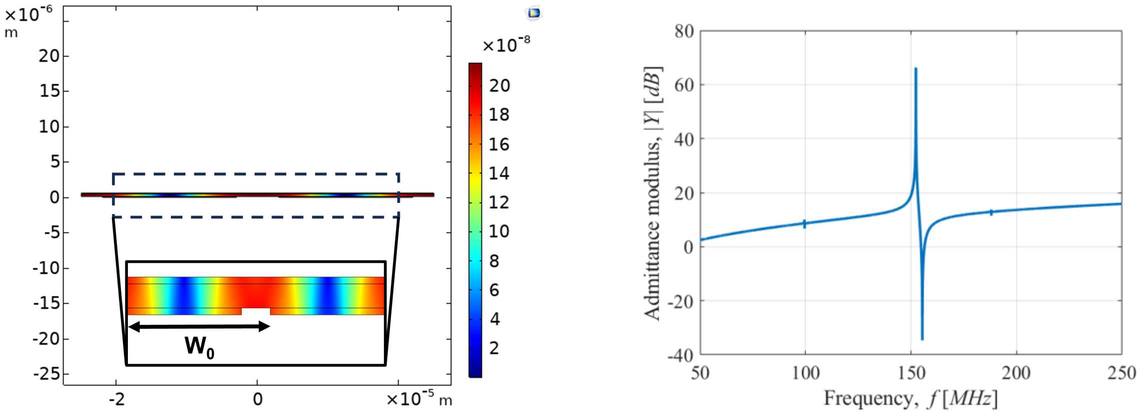

(a) Mechanical deformation: the red and blue colors indicate the locations of its maximum and minimum values, respectively.

(b) Admittance response: the acoustic resonance occurs around 153 MHz setting the IDE pitch size W_0 at 25 μm and the single finger width at 19 μm.

Figure 5.17: COMSOL simulation of the proposed device.

5.1.4 Read-out circuit

To verify the analytical model described in section 3.3, the Pierce oscillator was simulated in ADS using the mBVD model described in section 3.2.2 as the equivalent impedance of the resonator in the feedback network with values of its components coming from the model fitting described in section 5.2.3. The schematic of the circuit is presented in Figure 5.18.

An AC simulation was performed first to extract the open loop gain and phase. After verifying the Barkhausen criteria, a transient simulation was performed to monitor the oscillation over time and extract the oscillation frequency, which turns out to be around 150 MHz from the peak-to-peak measurement of the oscillation period shown in Figure 5.19a, thereby matching the analytical model. Finally, a harmonic balance simulation was performed to check the tones of the sine wave oscillation, further confirming the oscillator to oscillate at 150 MHz, since the highest tone is the first one as shown in Figure 5.19b.

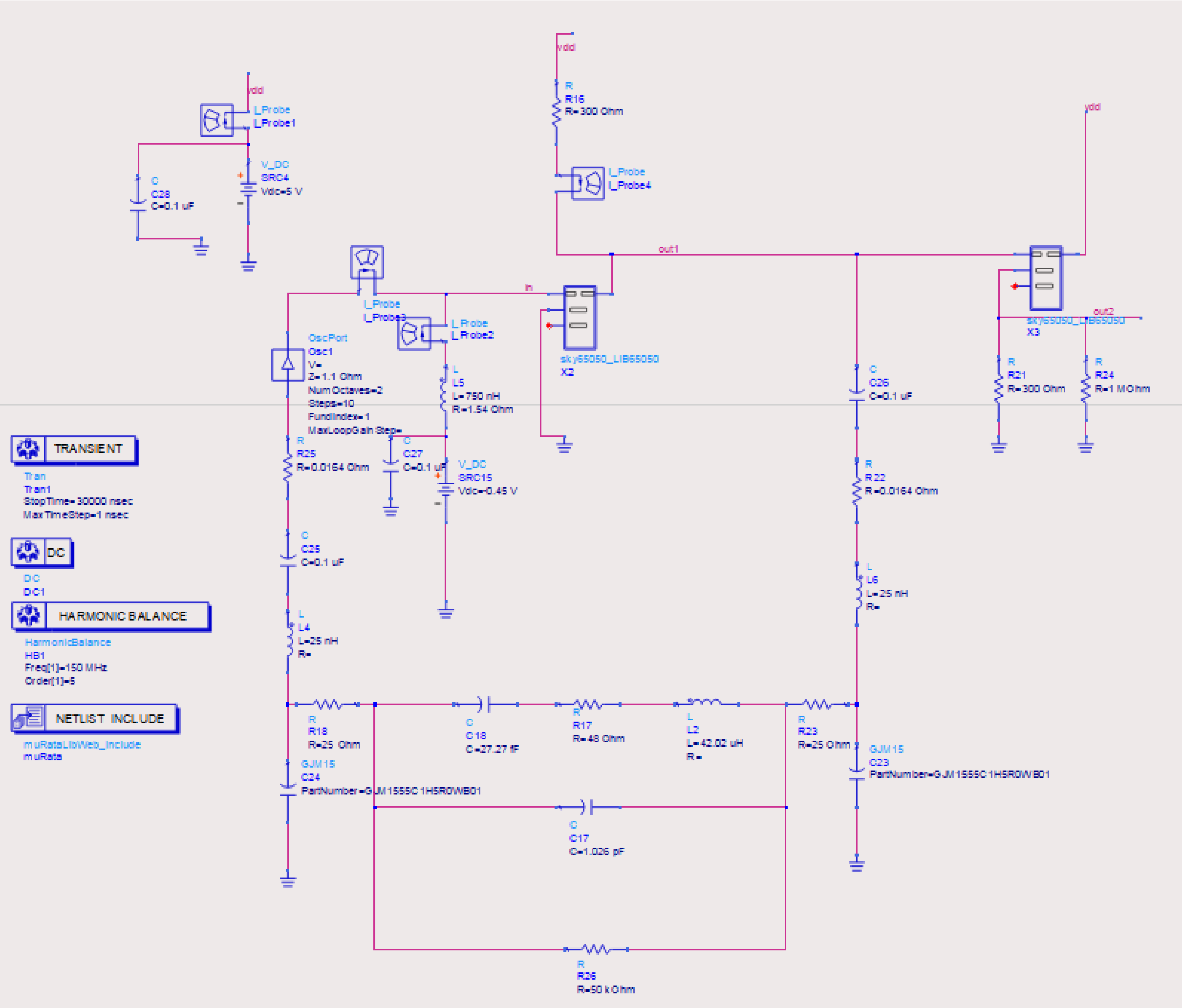

Figure 5.18: Schematic of the Pierce oscillator in ADS.

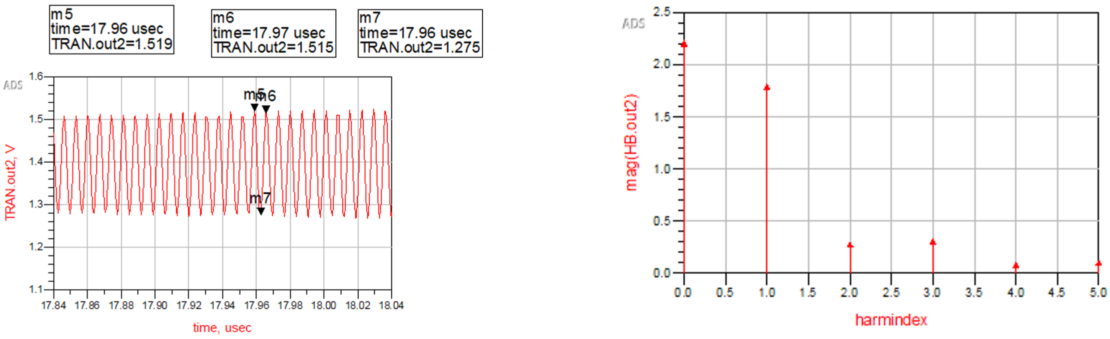

(a) Transient simulation of the output of the oscillator. **(b)** Harmonic balance simulation.

Figure 5.19: ADS simulation results.

5.2 Experimental proof

5.2.1 Spot pattern and multiple reflections

The customized Herriott gas cell has been built by using the two commercially available gold-coated concave spherical mirrors described in section 5.1.1.4 [90], mounted along a common optical axis through a cage system fixed onto an optical table.

In particular, Figure 5.20 shows the experimental setup implemented to validate the analytical model of the Herriott cell described in section 3.1.2. A red laser emits a beam whose size is firstly reduced by a pinhole and then it is forced to enter the Herriott cell through the hole properly positioned on the near mirror with a certain inclination angle set by the reflection on a properly oriented silver-coated flat mirror. While the laser beam undergoes multiple reflections between the two spherical mirrors, thereby multiplying its optical path length, a circular spot pattern is described on both the near and far mirrors. Eventually, the laser beam exits the Herriott cell through the hole properly positioned on the far mirror. In particular, since both the distance between the spherical mirror composing the Herriott cell and the angle with which the beam enters the Herriott cell are the two most crucial parameters that allow obtaining the desired spot pattern and so the targeted optical path length to be covered, a system of linear translation stages and a kinematic mirror mount are used. Specifically, the near mirror is kept fixed, while the far one is mounted on a linear translation stage allowing for the precise tuning of the distance between them. Moreover, the red laser is aligned with the center of the silver-coated flat mirror and they are both mounted on a system consisting of two combined linear translation stages allowing for the tuning of the distance of the reflection point from both the optical axis of the Herriott cell and the surface of the near mirror. Additionally, the orientation of the silver-coated flat mirror can be further precisely tuned by mounting it on a kinematic mirror mount.

A power meter has been used to measure the power of the laser beam before and after entering the Herriott cell in order to retrieve the number of reflections and so the covered optical path length from the amount of power lost through the nominal mirror losses at the operating wavelength.

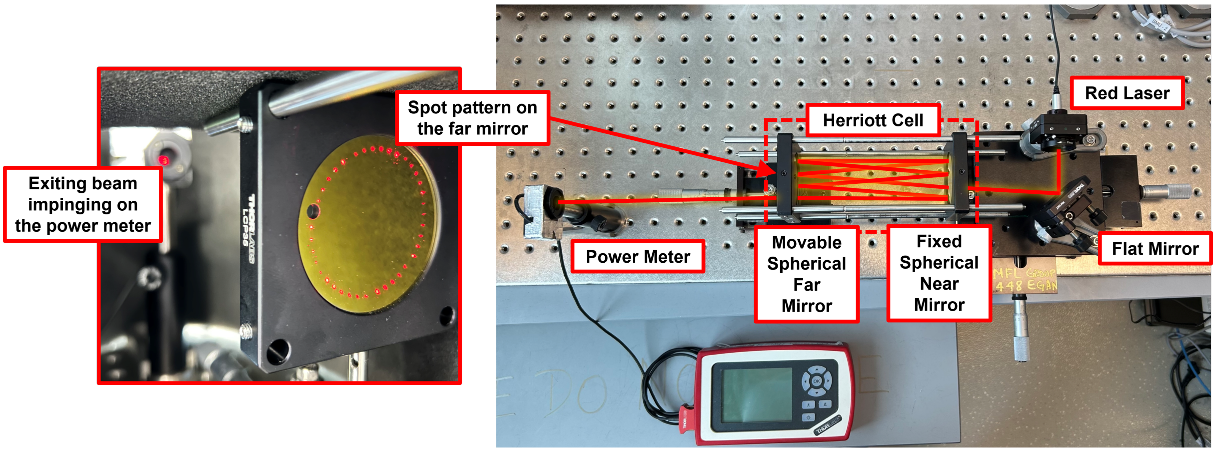

Figure 5.20: Optical setup built to prove the Herriott cell analytical model with the spot pattern obtained on the far mirror.

5.2.2 FTIR measurement

The *reflectance* R of the fabricated devices were measured using a Bruker V70 Fourier Transform InfraRed (FTIR) spectrometer coupled with a Hyperion 1000 microscope. The *absorption efficiency* η was then calculated as follows:

$$\eta = 1 - R - T \simeq 1 - R, \tag{5.6}$$

where the *transmittance* T through the bottom metal plate is considered negligible, since the material stack has been designed so that the thickness of the underlying Al electrode, i.e. 100 nm, is much larger, i.e. around one order of magnitude higher, than its penetration depth. In particular, Figure 5.21a demonstrates a partial agreement of the experimental results collected after the releasing process with the FIT simulations run on CST, especially regarding the spectral position of the absorption peak. On the other hand, the absolute value of absorption is significantly lower and the bandwidth is slightly wider. In order to assess this problem, the same measurement has been performed on another chip also before the releasing process. In particular, Figure 5.21b shows an experimentally extracted absorption peak of around $\sim 80\%$ near the wavelengths targeted during the CST simulations before the releasing process. However, a drastic decrease of the absorption and a shift of the wavelength at which the peak of absorption occurs was observed after the releasing process. This allowed to ascribe the reason to something not controllable that occurs during the XeF_2 etching performed to release the device: the lateral dimensions of the Au patches may decrease during the releasing process, thereby leading to a shifted spectrum. However, concerning the huge decrease of the absorption value, a possible reason can be a possible bending of the resonator that can still occur after the releasing process, leading to a not perfectly normal impinging of the laser beam with respect to the device surface, which affects the performance of the plasmonic metamaterial absorbers especially when the patches are square-shaped and not cross-shaped.

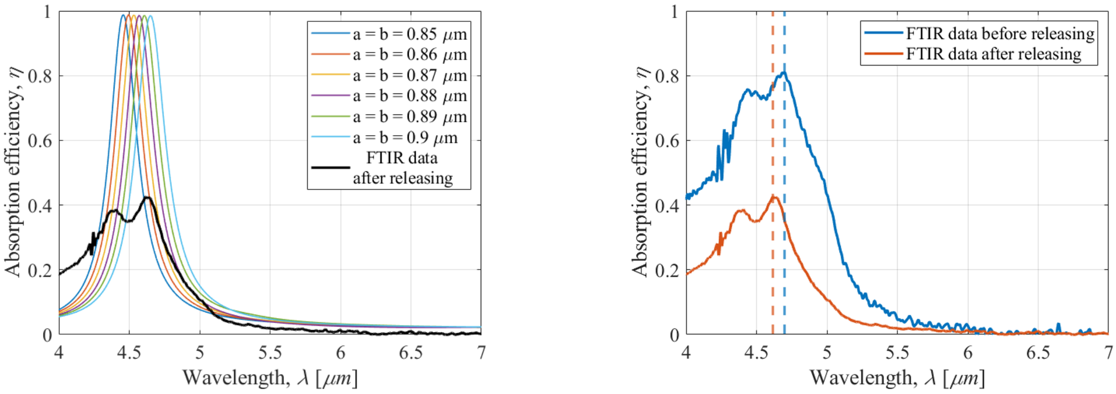

(a) Comparison of the experimental results after the release of the device with the CST simulations.

(b) Comparison of the experimental results before and after the release of the device.

Figure 5.21: FTIR measurement results.

The small discrepancy in terms of absorption, wavelength, and FWHM of the main peak between simulation and measurement results could be due to both the diffraction induced by both the non-flat bottom surface of the absorber resulting from the topography of the IDE and possible defects from the fabrication of plasmonic nanostructures. This difference can be reduced by tuning the fabrication process. Additionally, changing the geometry of the top Au patches from a square to a cross will sharpen the response, make it more immune to impinging beam angle and polarization, and reduce the absorption bandwidth, resulting in a more robust system immune to spectral interference. Moreover, in order to counterbalance the shrinking of the lateral dimensions of the Au patches during the releasing process, two possible solutions can be explored in the future: intentionally fabricate Au patches slightly larger or capping Au patches with a Pt layer thinner than 10 nm, even if this additional Pt layer may cause a $\sim$ 15% increasing in bandwidth (from data collected during previous experiments run in the same laboratory).

5.2.3 RF electrical response and TCF measurement

The devices were tested in an RF probe station under indoor ambient conditions and their RF electrical responses were measured by an Agilent E5071C VNA after Short-Open-Load (SOP) calibration. The electromechanical performance of the devices was quantified by mBVD model fitting, as shown in Figure 5.22a. In particular, a resonance frequency $f_0 \sim 148.4\ MHz$, a high motional quality factor $Q_m \sim 800$, and a high electromechanical coupling $k_t^2 \sim 3.3\%$ were extracted from the fitting of the motional branch C_m, L_m, and R_m, which turned out to be equal to 0.274 fF, 0.419 μH, and 48.82 Ω, respectively. Moreover, the static capacitance C_0 and series resistance R_s were found to be 1.026 fF and 61 Ω, respectively. Finally, a NEP around $\sim$ 600 $pW/Hz^{1/2}$ was measured by monitoring the noise-induced frequency fluctuation of the resonator.

The TCF of the devices was also characterized by repeated admittance measurements over a wide range of temperatures set by heating up the stage of the probe station, as shown in Figure 5.22b. A TCF value twice as large than previous demonstrations ($\sim$ - 27 ppm/K with AlN as a piezoelectric layer and SiO_2 as a dielectric spacer for the plasmonic metamaterial absorbers [24]) was found to be $\sim$ - 55 ppm/K.

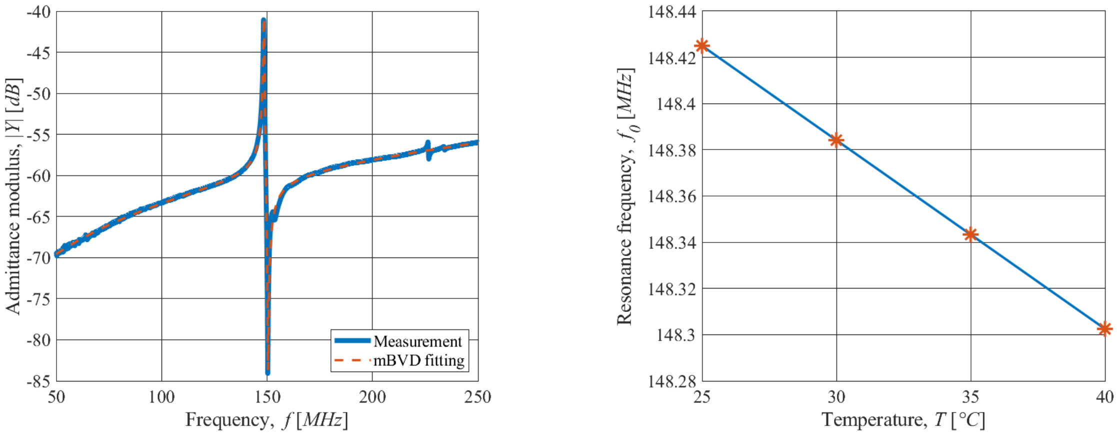

(a) Measured admittance response of the resonant IR sensor and the corresponding mBVD fitting.

(b) TCF extraction as the slope of the curve normalized to the resonance frequency at ambient temperature.

Figure 5.22: RF electrical response and TCF measurement.

5.2.4 IR response measurement

The experimental setup shown in Figure 5.23 was used to test the responsivity to the IR light of the device. In particular, its IR response was tested using a blackbody IR source, which was firstly calibrated with a power sensor consisting of a $HgCdTe$ photodiode sensible to IR light (Thorlabs S180C). Placing the sensor at a distance comparable to the one at which the device was tested later, the power P_{sensor} of the IR light emitted by the blackbody was measured, thereby characterizing and estimating the power density ρ_{BB} of the IR light beam emitted by the blackbody as follows:

$$\rho_{BB} = \frac{P_{sensor}}{A_{sensor}}, \tag{5.7}$$

where A_{sensor} is the active area of the power sensor.

The fabricated device was placed inside a vacuum chamber and exposed to the blackbody IR radiation through a transparent CaF_2 window. The amount of IR power delivered to the device under test was then calculated as follows:

$$P_{delivered} = \rho_{BB} \cdot A_{device} \cdot T_{CaF_2}, \tag{5.8}$$

where ρ_{BB} is the calibrated power density, A_{device} is the area of the device covered by the plasmonic absorbers, and T_{CaF_2} is the transmittance of CaF_2 window.

The corresponding portion of IR power absorbed by the device was finally calculated as follows:

$$P_{absorbed} = P_{delivered} \cdot \eta, \tag{5.9}$$

where η is the measured FTIR absorption efficiency. It is worth noting that, the absorbed power estimated in this way represents the maximum possible value: a minor potential misalignment between the device and the IR beam emitted by the blackbody inevitably results in a loss of power density delivered and so absorbed by the device. Therefore, the actual absorbed power is likely to be smaller than the estimated maximum value.

In particular, setting the temperature of the blackbody to 950 $^{\circ}C$, the absorbed power was estimated to be $\sim$ 84 μW, causing a down-shift in the resonance frequency around $\sim$ 30 kHz shown in Figure 5.24, which corresponds to a temperature increase in the device $\sim$ 3.5 K given the measured TCF. Moreover, knowing the measured TCF and resonance frequency of the device when not illuminated, the thermal resistance of the device was readily extracted to be $\sim 4.75 \cdot 10^4 K/W$ from the estimated absorbed power and down-shift in the resonance frequency. The thermal time constant was estimated to be $\sim$ 2.9 ms based on the quantified thermal resistance and the thermal capacitance, which was estimated from the nominal properties of the materials composing the stack of the device and assuming perfect thermal isolation with respect to the substrate.

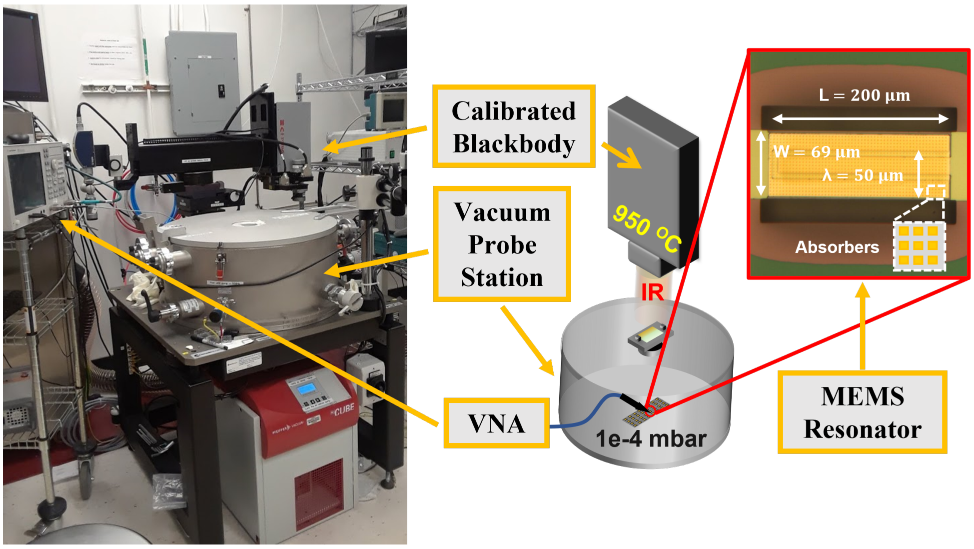

Figure 5.23: Experimental setup for IR response measurement.

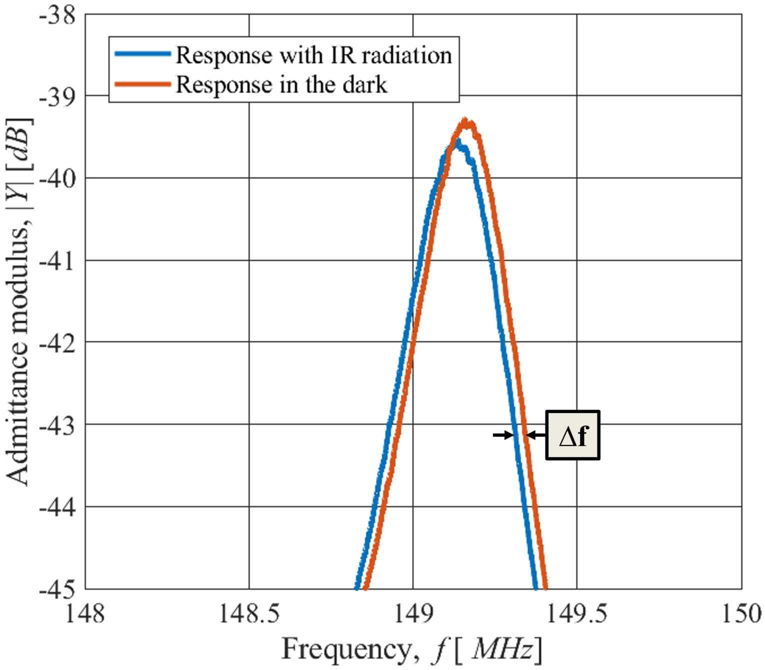

Figure 5.24: IR-induced frequency shift in the device.

5.2.5 Pierce oscillator

The PCB layout of the Pierce oscillator was designed in Eagle (see Figure 5.25a) and sent to the manufacturer for fabrication (see Figure 5.25b). In particular, in order to ensure good performance, high tolerance and temperature stability components were used to implement the layout. Moreover, wide traces were used and a large distance between the direct current (DC) and RF parts was kept to avoid interferences. The IC chip was connected to the MEMS resonator by wire-bonding, even if it is worth mentioning that post-CMOS MEMS-IC integration is always feasible as the devices are fabricated at very low temperatures.

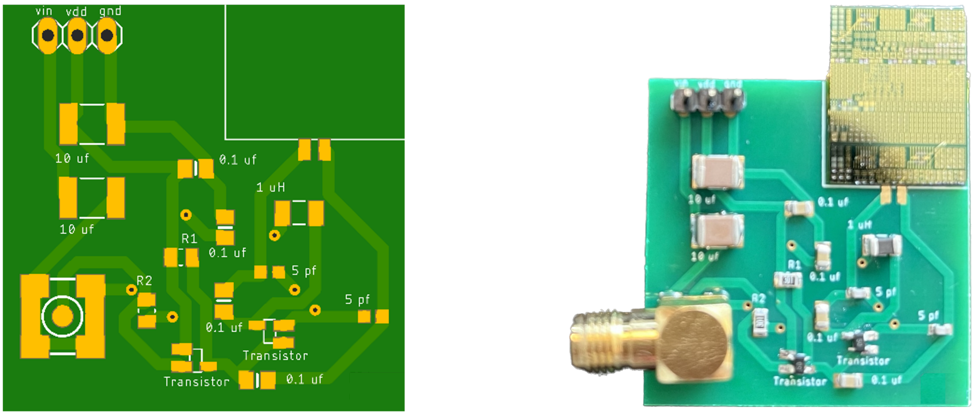

(a) Final PCB layout designed. **(b)** Final PCB used for the testing.

Figure 5.25: PCB layout: the board includes all the components specified in the simulated circuit in section 5.1.4, an SMA connector used to connect the output of the circuit to the oscilloscope during the testing, the pins used to power the circuit with bench-top DC power supplies, and an area where the fabricated die is taped to wire-bond the resonator and include it in the feedback loop of the oscillator.

The experimental setup shown in Figure 5.26 was implemented to perform time domain measurements through an oscilloscope in order to monitor the output voltage of the oscillator, i.e. the frequency of the generated sine wave, which turned out to be 149 MHz, as predicted from the ADS simulation. As a further confirmation, the harmonic balance was performed and the main tone was found at 150 MHz, as shown in Figure 5.27a. Moreover, the phase noise was extracted using a signal spectrum analyzer by measuring the difference between the power of the signal at the nominal oscillating frequency (expressed in dBm), i.e. the carrier, and the noise power over a 1 Hz bandwidth at a certain frequency offset from the nominal oscillating frequency (expressed in dBm/Hz). For this reason, its unit of measurement is dBc/Hz, which refers to the noise power in dBm/Hz with respect to the power of the carrier, and the obtained curve of the phase noise from 100 Hz to 1 MHz frequency offset from the carrier is shown in Figure 5.27b. Table 5.4 includes some reference phase noise values for specific frequency offsets. As expected, the phase noise is always negative and it increases in modulus as the frequency offset increases.

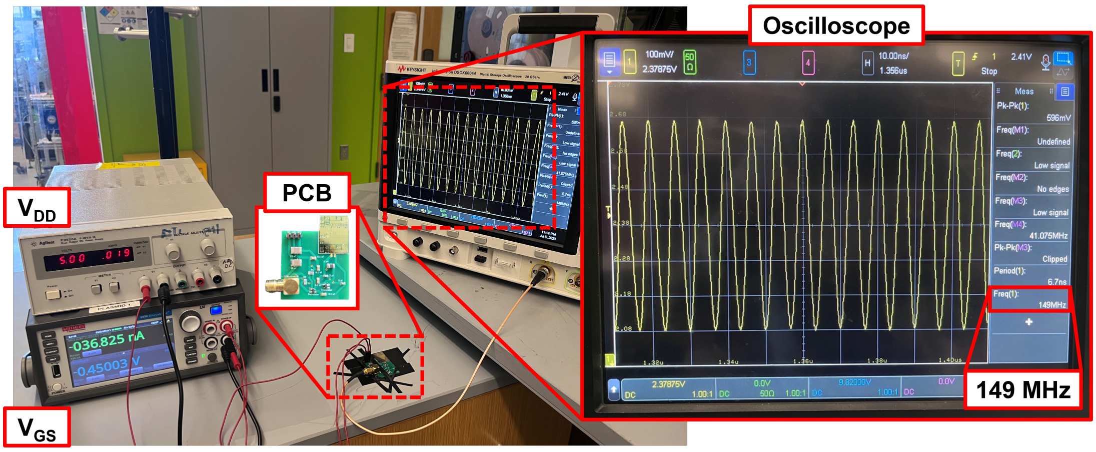

Figure 5.26: Experimental setup for the analysis of the Pierce oscillator. Two bench-top DC power supplies are used to power the circuit at the two needed voltage levels through 3 pins inserted on the PCB. The output of the circuit is monitored by an oscilloscope connected to the PCB through an SMA cable.

(a) Harmonic balance. **(b)** Phase noise.

Figure 5.27: Experimental results from the analysis of the Pierce oscillator.

Offset	***Phase Noise** [dBc/Hz]*
1 kHz	- 70.00
10 kHz	- 100.70
100 kHz	- 116.00
1 MHz	- 132.35

Table 5.4: Phase noise values at specific frequency offsets.

After implementing and testing the single Pierce oscillator circuit, the complete circuit for the differential reading will be implemented.

Chapter 6

Conclusions

A complete design and fabrication of all the sub-parts of a N_2O sensor suitable for operation on a drone platform was performed. The work was firstly focused on the needed optical components, starting from the selection of the optimal laser emission wavelength and the necessary optical path length, and continuing with the design, realization, and testing of a custom Herriott cell. Contemporarily, the design and fabrication of the MEMS-based IR detector were performed and its performance was assessed in terms of both electromechanical and IR response. Lastly, a Pierce oscillator was designed as read-out circuit by using the fabricated resonator as the frequency-selective element in the feedback network and, after realizing the PCB, it was tested by monitoring its output voltage and extracting both the frequency of oscillation and the phase noise.

The experimental results presented in the last part of the previous chapter represent the first experimental demonstration of a $ScAlN$ MEMS resonant IR detector for chemical sensing. The device employs a stack of 30%-doped 350 nm-thick $ScAlN$ and 250 nm-thick AlN to respectively define the resonator and the IR-selective metamaterial layer, targeting an absorption wavelength close to 5 μm, which is typical for IR spectroscopy applications. The device achieved an IR absorption of approximately 80% at an IR wavelength of 4.8 μm, along with a motional quality factor Q_m of about 800 and an electromechanical coupling k_t^2 of about 3.3%. Moreover, by utilizing AlN for the metamaterial dielectric and highly doped $ScAlN$ for the resonant cavity, the TCF has been doubled up to - 55 $ppm/°C$, compared to prior implementations relying on an AlN-SiO_2 stack, which presented a TCF not larger than -27 $ppm/°C$. These experimental results represent a promising initial stride and demonstrate the potential of the $ScAlN$-AlN stack to move towards uncooled, miniaturized, and highly sensitive IR sensors by means of exploiting the improved material properties that it offers with respect to other more conventional stacks. However, many optimizations can be performed to enhance the device sensitivity to incident power down to the nW range [64]. Firstly, the metamaterial stack implemented on AlN requires further investigation to sharpen the IR absorption response. In fact, previous studies on SiO_2 have shown that optimizing the dielectric and patch thickness, as well as switching to a cross-shaped design, are useful steps towards this goal [43]. Additionally, the resonator used in this first experimental demonstration was fully anchored to the substrate, which is a significantly sub-optimal design for thermally insulating the resonator. Therefore, a narrow and thin anchor design is preferable to maximize the temperature change occurring in the plate for a given incident power. Finally, the total stack thickness must be reduced as much as possible to lower the device's thermal capacitance, thereby improving the time response of the IR sensor.

6.1 Future studies

This thesis work has been carried on during the first one-year phase of a three-year research project led and managed by PI Prof. Rinaldi at Northeastern University, and funded by the ARPA-E OPEN 2021 program. I will keep working on the same project up to its completion during my PhD degree.

In particular, this first phase was focused on the design of the overall system and the fabrication of the MEMS IR sensor with performance meeting the program requirements. The second phase will focus on the test of the LAS gas sensor system with a commercial QCL and a commercial gas cell integrated using the experimental optical table setup already designed and implemented (shown and described in section 4.4) to validate the performance metrics first, followed by the design and production of a customized gas cell suitable for a drone platform, while the final one-year phase will focus on the sensor vacuum packaging, system integration, and optimization to meet the goals on SWaP as well as the test of the system with actual drones for the validation of extended operation time and high-speed data acquisition.

Moreover, during the whole 3-year project, a robust go-to-market strategy and transition plan will be developed by performing tasks on market analysis, cost modeling, end-user engagement, competitive analysis, patent white space analysis, and techno-economic analysis. In particular, the technology-to-market (T2M) transition is also encouraged by the unique capabilities of the facilities that the *George J. Kostas Nanoscale Technology and Manufacturing Research Center* at Northeastern University owns. In particular, it is the only academic institution in the USA hosting a foundry-compatible tool for the deposition of high-quality AlN-$ScAlN$ piezoelectric thin films on 8-inch wafers.

6.2 Other potential applications

Finally, a market analysis on gas sensors has been conducted, crafting an initial product hypothesis and searching for potential product-to-market fit. In particular, three industries have been identified: oil and gas leaks, domestic air quality, and industrial air quality. These three markets were selected based on the shared value of having a high-speed and low-power gas sensor. Oil and gas leaks in particular take advantage of drone-based gas sensing approaches while air quality monitoring uniquely benefits from highly responsive gas sensors. As such, each market has been explored extensively to discover potential value that can be added to each industry:

- in the oil and gas industry, methane gas leaks may occur anywhere along a company's network of pipelines. As a result, these big businesses need responsive solutions for detecting and addressing these leaks to minimize the environmental impact. Currently, companies take advantage of a variety of airborne vehicles, both manned and unmanned, to carry out this challenge. The drone-based gas sensing technology presented in this thesis fits well into this industry's needs as a lightweight solution that provides high spatial and temporal resolution in a given surveillance range. By taking advantage of such a zero-power sensor, the drone will consume far less battery power than industry-standard drones, leading to longer flight times and increased data acquisition;
- as a result of COVID-19, domestic residents have become more interested in maintaining high-quality living environments through smart home solutions. This gas-sensing technology could be applied also in air quality purification and monitoring systems. By providing highly responsive gas sensing, this gas sensor will improve air purification systems' performance while simultaneously

maintaining longer battery life. As a near zero-power sensor, the gas sensor will positively impact the battery lifespan of wall-mounted devices, thus requiring cheaper, lower-cost batteries for finished products as well as the ability easily integrate multiple sensors working in parallel. This design choice is essential in air quality control, as gas sensors need to accurately track the presence of several volatile organic compounds to deliver accurate readouts;

- unlike domestic air quality systems, industrial air quality systems must monitor much larger spaces, both indoors and outdoors while additionally providing overt alarm systems to warn of high concentrations of hazardous gases, such as sulfuric acid or ammonia. While both industries benefit from high-speed gas sensing, industrial air quality monitoring will specifically take advantage of the low volume of each gas sensor. This allows for scalable gas monitoring systems to meet the needs of large manufacturing plants or networks of mining shafts. Furthermore, the small form factor will allow for easy integration into both fixed and portable devices, allowing for key pipelines to be monitored at all times without sacrificing the ability to detect hazardous gases in more remote spaces. As a high-quality scalable device, the proposed gas sensor brings clear advantages to industrial air quality monitoring.

Three additional markets to target have been also identified: food and beverages, gas supply chain, and transportation of perishable goods. However, each of these markets raised individual concerns with proceeding with the T2M effort of the proposed system. While the presence of CO_2 is a staple for sodas and other sugary refreshments, quality control of this gas is easily done using paper colorimetry strips rather than electronic gas sensors. Similarly, industrial gas suppliers rely primarily on pressure sensors rather than gas sensors to accurately determine the amount of gas transported. While climate control is important when transporting produce and livestock, temperature and humidity sensors provide sufficient evidence of a safe transportation environment, removing the need for gas sensors.

The particular application of the proposed gas sensor is its integration with lightweight drones such that surveyors can easily assess large tracts of farmland for N_2O concentration. While other companies have made little effort to monitor N_2O, several groups have demonstrated the potential of CH_4 mapping using drone-based gas sensing. For example, ABB Hoverguard serves as an early example of a large corporate interest in drone-based gas sensing. As a business drone-based CH_4 detection, it has seen regular use in oil and gas leak detection from companies such as UgCs, SeekOps, and Ravan Air. The gas sensing capabilities of the proposed system will be at least on par with industry standards in the most significant parameters. However, each of these drones comes equipped with software to process and analyze data collected by the drone, a feature that is planned to be addressed.

References

[1] *U.S. Environmental Protection Agency*. URL: https://www.epa.gov/ (visited on 10/07/2022).

[2] Susan Solomon et al. *Climate change 2007-the physical science basis: Working group I contribution to the fourth assessment report of the IPCC*. Vol. 4. Cambridge university press, 2007.

[3] A. R. Ravishankara, John S. Daniel, and Robert W. Portmann. “Nitrous Oxide N_2O: The Dominant Ozone-Depleting Substance Emitted in the 21st Century”. In: *Science* 326.5949 (2009), pp. 123–125. DOI: 10.1126/science.1176985. URL: https://www.science.org/doi/abs/10.1126/science.1176985.

[4] Dave S Reay et al. “Global agriculture and nitrous oxide emissions”. In: *Nature climate change* 2.6 (2012), pp. 410–416.

[5] Leilei Ruan and G Philip Robertson. “Initial nitrous oxide, carbon dioxide, and methane costs of converting conservation reserve program grassland to row crops under no-till vs. conventional tillage”. In: *Global Change Biology* 19.8 (2013), pp. 2478–2489.

[6] P. M. Vitousek et al. “Nutrient Imbalances in Agricultural Development”. In: *Science* 324.5934 (2009), pp. 1519–1520. DOI: 10.1126/science.1170261. URL: https://www.science.org/doi/abs/10.1126/science.1170261.

[7] Alan Stanton et al. *Portable nitrous oxide sensor for understanding agricultural and soil emissions*. Tech. rep. Southwest Sciences, Inc., Santa Fe, NM (United States), 2017.

[8] Markku Vainio and Lauri Halonen. “Mid-infrared optical parametric oscillators and frequency combs for molecular spectroscopy”. In: *Physical Chemistry Chemical Physics* 18.6 (2016), pp. 4266–4294.

[9] Hans Zogg et al. “Photovoltaic IV-VI on Si infrared sensor arrays for thermal imaging”. In: *Optical Engineering* 34.7 (1995), pp. 1964–1969.

[10] T. White, N. Butler, and R. Murphy. “An uncooled IR sensor with digital focal plane array [and medical application]”. In: *IEEE Engineering in Medicine and Biology Magazine* 17.4 (1998), pp. 60–65. DOI: 10.1109/51.687965.

[11] Josep M Bayona, Carmen Domínguez, and Joan Albaigés. “Analytical developments for oil spill fingerprinting”. In: *Trends in Environmental Analytical Chemistry* 5 (2015), pp. 26–34.

[12] Pierre Barritault et al. “Low power CO2 NDIR sensing using a micro-bolometer detector and a micro-hotplate IR-source”. In: *Sensors and Actuators B: Chemical* 182 (2013), pp. 565–570.

[13] J Tanaka et al. “Thermopile infrared array sensor for human detector application”. In: *2014 IEEE 27th International Conference on Micro Electro Mechanical Systems (MEMS)*. IEEE. 2014, pp. 1213–1216.

[14] Doris Ng et al. “Cmos-Mems SC0.12AL0.88 N-Based Pyroelectric Infared Detector with CO2 Gas Sensing”. In: Jan. 2021, pp. 852–855. DOI: 10.1109/MEMS51782.2021.9375435.

[15] F.C. Bosveld and A.C.M. Beljaars. “The impact of sampling rate on eddy-covariance flux estimates”. In: *Agricultural and Forest Meteorology* 109.1 (2001), pp. 39–45. ISSN: 0168-1923. DOI: https://doi.org/10.1016/S0168-1923(01)00257-X. URL: https://www.sciencedirect.com/science/article/pii/S016819230100257X.

[16] *DJI Matrice 300 RTK*. URL: https://enterprise.dji.com/it/matrice-300 (visited on 10/10/2022).

[17] Araceli Larios. “Challenges in the measurement of emissions of nitrous oxide and methane from livestock sector”. In: *Reviews in Environmental Science and Bio/Technology* 15 (May 2018).

[18] Alan Fried and Dirk Richter. “Infrared absorption spectroscopy”. In: *Analytical Techniques for Atmospheric Measurement* 1 (2006), pp. 72–146.

[19] Yu Hui et al. “Plasmonic piezoelectric nanomechanical resonator for spectrally selective infrared sensing”. In: *Nature Communications* 7 (Apr. 2016), p. 11249. DOI: 10.1038/ncomms11249.

[20] *Senseair K30 NDIR Carbon Dioxide Sensor*. URL: https://senseair.com/products/flexibility-counts/k30/ (visited on 10/13/2022).

[21] *Viasensor G200 N2O analyzer*. URL: https://www.viasensor.info/ (visited on 10/17/2022).

[22] *Sumitomo Electric compact DFB-QCL*. URL: https://global-sei.com/qcl/ (visited on 10/14/2022).

[23] *Axetris LGD Compact-A CH4*. URL: https://www.axetris.com/en/lgd/products/lgd-compact/lgd-compact-a-ch4 (visited on 10/24/2022).

[24] Zhenyun Qian et al. “Narrowband MEMS resonant infrared detectors based on ultrathin perfect plasmonic absorbers”. In: *2016 IEEE SENSORS*. 2016, pp. 1–3. DOI: 10.1109/ICSENS.2016.7808614.

[25] RF Curl and Frank K Tittel. “7 Tunable infrared laser spectroscopy”. In: *Annual Reports Section" C"(Physical Chemistry)* 98 (2002), pp. 219–272.

[26] *Multipass gas cells overview by RP Photonics*. URL: https://www.rp-photonics.com/multipass_gas_cells.htmlE (visited on 10/16/2022).

[27] ML Thoma, R Kaschow, and FJ Hindelang. “A multiple-reflection cell suited for absorption measurements in shock tubes”. In: *Shock Waves* 4 (1994), pp. 51–53.

[28] Béla Tuzson et al. “Compact multipass optical cell for laser spectroscopy”. In: *Optics letters* 38.3 (2013), pp. 257–259.

[29] John U White. “Long optical paths of large aperture”. In: *JOSA* 32.5 (1942), pp. 285–288.

[30] D. Herriott, H. Kogelnik, and R. Kompfner. “Off-Axis Paths in Spherical Mirror Interferometers”. In: *Appl. Opt.* 3.4 (1964), pp. 523–526. DOI: 10.1364/AO.3.000523. URL: https://opg.optica.org/ao/abstract.cfm?URI=ao-3-4-523.

[31] Donald R Herriott and Harry J Schulte. “Folded optical delay lines”. In: *Applied Optics* 4.8 (1965), pp. 883–889.

[32] Claude Robert. “Simple, stable, and compact multiple-reflection optical cell for very long optical paths”. In: *Applied Optics* 46.22 (2007), pp. 5408–5418.

[33] Aliaksandr Hubarevich et al. “Ultra-thin broadband nanostructured insulator-metal-insulator-metal plasmonic light absorber”. In: *Opt. Express* 23.8 (2015), pp. 9753–9761. DOI: `10.1364/OE.23.009753`. URL: `https://opg.optica.org/oe/abstract.cfm?URI=oe-23-8-9753`.

[34] Joo-Yun Jung et al. “Infrared broadband metasurface absorber for reducing the thermal mass of a microbolometer”. In: *Scientific Reports* 7.1 (2017), pp. 1–8.

[35] Shinpei Ogawa and Masafumi Kimata. “Metal-Insulator-Metal-Based Plasmonic Metamaterial Absorbers at Visible and Infrared Wavelengths: A Review”. In: *Materials* 11.3 (2018). ISSN: 1996-1944. DOI: `10.3390/ma11030458`. URL: `https://www.mdpi.com/1996-1944/11/3/458`.

[36] Shiwen Luo et al. “Perfect narrow band absorber for sensing applications”. In: *Optics express* 24.9 (2016), pp. 9288–9294.

[37] Abdul Aleem Jamali and Bernd Witzigmann. “Plasmonic perfect absorbers for biosensing applications”. In: *Plasmonics* 9 (2014), pp. 1265–1270.

[38] Hung-Hsin Chen et al. “A plasmonic infrared photodetector with narrow bandwidth absorption”. In: *Applied Physics Letters* 105.2 (2014), p. 023109.

[39] Jonathan Y Suen et al. “Multifunctional metamaterial pyroelectric infrared detectors”. In: *Optica* 4.2 (2017), pp. 276–279.

[40] Erdem Aslan et al. “Metamaterial plasmonic absorber for reducing the spectral shift between near- and far-field responses in surface-enhanced spectroscopy applications”. In: *Sensors and Actuators A: Physical* 267 (2017), pp. 60–69.

[41] Zhenyun Qian et al. “Zero-power infrared digitizers based on plasmonically enhanced micromechanical photoswitches”. In: *Nature nanotechnology* 12.10 (2017), pp. 969–973.

[42] Shuang Zhang et al. “Near-infrared double negative metamaterials”. In: *Opt. Express* 13.13 (2005), pp. 4922–4930. DOI: `10.1364/OPEX.13.004922`. URL: `https://opg.optica.org/oe/abstract.cfm?URI=oe-13-13-4922`.

[43] Sungho Kang et al. “Ultra-Narrowband Metamaterial Absorbers for High Spectral Resolution Infrared Spectroscopy”. In: *Advanced Optical Materials* 7.2 (2019), p. 1801236. DOI: `https://doi.org/10.1002/adom.201801236`. eprint: `https://onlinelibrary.wiley.com/doi/pdf/10.1002/adom.201801236`. URL: `https://onlinelibrary.wiley.com/doi/abs/10.1002/adom.201801236`.

[44] Sungho Kang et al. “Ultra narrowband infrared absorbers for omni-directional and polarization insensitive multi-spectral sensing microsystems”. In: *2017 19th International Conference on Solid-State Sensors, Actuators and Microsystems (TRANSDUCERS)*. 2017, pp. 886–889. DOI: `10.1109/TRANSDUCERS.2017.7994191`.

[45] Atsushi Sakurai, Bo Zhao, and Zhuomin Zhang. “Prediction of the resonance condition of metamaterial emitters and absorbers using LC circuit model”. In: *International Heat Transfer Conference Digital Library*. Begel House Inc. 2014.

[46] Atsushi Sakurai, Bo Zhao, and Zhuomin M Zhang. “Resonant frequency and bandwidth of metamaterial emitters and absorbers predicted by an RLC circuit model”. In: *Journal of Quantitative Spectroscopy and Radiative Transfer* 149 (2014), pp. 33–40.

[47] H. Bhugra and G. Piazza. *Piezoelectric MEMS Resonators*. Microsystems and Nanosystems. Springer International Publishing, 2017. Chap. 2. ISBN: 9783319286860. URL: `https://books.google.com/books?id=2d0ijwEACAAJ`.

[48] Miguel A Caro et al. “Piezoelectric coefficients and spontaneous polarization of ScAlN”. In: *Journal of Physics: Condensed Matter* 27.24 (2015), p. 245901.

[49] Azadeh Ansari. “Single crystalline scandium aluminum nitride: An emerging material for 5G acoustic filters”. In: *2019 IEEE MTT-S International Wireless Symposium (IWS)*. IEEE. 2019, pp. 1–3.

[50] Chih-Ming Lin et al. “Thermal compensation for aluminum nitride Lamb wave resonators operating at high temperature”. In: *2010 IEEE International Frequency Control Symposium*. IEEE. 2010, pp. 14–18.

[51] Chengjie Zuo et al. “Multifrequency pierce oscillators based on piezoelectric AlN contour-mode MEMS technology”. In: *Journal of Microelectromechanical Systems* 19.3 (2010), pp. 570–580.

[52] Clark T-C Nguyen. “MEMS technology for timing and frequency control”. In: *IEEE transactions on ultrasonics, ferroelectrics, and frequency control* 54.2 (2007), pp. 251–270.

[53] Gianluca Piazza, Philip J Stephanou, and Albert P Pisano. “AlN contour-mode vibrating RF MEMS for next generation wireless communications”. In: *2006 European Solid-State Device Research Conference*. IEEE. 2006, pp. 61–64.

[54] Eric A Vittoz, Marc GR Degrauwe, and Serge Bitz. “High-performance crystal oscillator circuits: Theory and application”. In: *IEEE journal of solid-state circuits* 23.3 (1988), pp. 774–783.

[55] Manohar Nagaraju et al. “A 400μW differential FBAR sensor interface IC with digital readout”. In: *2015 Joint Conference of the IEEE International Frequency Control Symposium & the European Frequency and Time Forum*. IEEE. 2015, pp. 218–221.

[56] Ming Dong et al. “Herriott Cell Design With Minimum Volume and Multiple Reflection Rings for Infrared Gas Sensing”. In: *IEEE Photonics Technology Letters* 31.7 (2019), pp. 541–544. ISSN: 1941-0174. DOI: `10.1109/LPT.2019.2901196`.

[57] Gregory S. Engel and Elisabeth J. Moyer. “Precise multipass Herriott cell design: Derivation of controlling design equations”. In: *Opt. Lett.* 32.6 (2007), pp. 704–706. DOI: `10.1364/OL.32.000704`. URL: `https://opg.optica.org/ol/abstract.cfm?URI=ol-32-6-704`.

[58] Christopher G. Tarsitano and Christopher R. Webster. “Multilaser Herriott cell for planetary tunable laser spectrometers”. In: *Appl. Opt.* 46.28 (2007), pp. 6923–6935. DOI: `10.1364/AO.46.006923`. URL: `https://opg.optica.org/ao/abstract.cfm?URI=ao-46-28-6923`.

[59] Sungho Kang et al. “Chip-Scale MEMS-CMOS Multispectral Infrared Chemical Sensor”. In: *2019 IEEE 32nd International Conference on Micro Electro Mechanical Systems (MEMS)*. 2019, pp. 133–136. DOI: `10.1109/MEMSYS.2019.8870703`.

[60] Ruyue Cui et al. "Three-dimensional printed miniature fiber-coupled multipass cells with dense spot patterns for ppb-level methane detection using a near-IR diode laser". In: *Analytical Chemistry* 92.19 (2020), pp. 13034–13041.

[61] Vikrant J Gokhale, Paul D Myers, and Mina Rais-Zadeh. "Subwavelength plasmonic absorbers for spectrally selective resonant infrared detectors". In: *SENSORS, 2014 IEEE*. IEEE. 2014, pp. 982–985.

[62] Zhenyun Qian et al. "High figure-of-merit NEMS thermal detectors based on 50-nm thick AlN nano-plate resonators". In: *Applied Physics Letters* 115.26 (2019), p. 261102. DOI: 10.1063/1.5128643. eprint: https://doi.org/10.1063/1.5128643. URL: https://doi.org/10.1063/1.5128643.

[63] H. Bhugra and G. Piazza. *Piezoelectric MEMS Resonators*. Microsystems and Nanosystems. Springer International Publishing, 2017. Chap. 5. ISBN: 9783319286860. URL: https://books.google.com/books?id=2d0ijwEACAAJ.

[64] Sila Deniz Calisgan et al. "Spectroscopic Chemical Sensing Based on Narrowband MEMS Resonant Infrared Detectors". In: *2018 IEEE SENSORS*. 2018, pp. 1–4. DOI: 10.1109/ICSENS.2018.8589600.

[65] Marvin Frerking. *Crystal oscillator design and temperature compensation*. Springer Science & Business Media, 2012.

[66] W.M. Sansen. *Analog Design Essentials*. The Springer International Series in Engineering and Computer Science. Springer US, 2007. ISBN: 9780387257471. URL: https://books.google.it/books?id=d-Mv4nxmaPMC.

[67] *U.S. Average Wind Speed State Rank*. URL: http://www.usa.com/rank/us--average-wind-speed--state-rank.htm (visited on 10/07/2022).

[68] *Sensirion SHT45 - Humidity and Temperature sensor*. URL: https://sensirion.com/products/catalog/SHT45/ (visited on 11/21/2022).

[69] *Distributed Feedback QCLs on D-Mounts by Thorlabs*. URL: https://www.thorlabs.com/newgrouppage9.cfm?objectgroup_id=9101 (visited on 11/27/2022).

[70] *Tattu 450mAh 4S1P 14.8V 75C Lipo Battery Pack With XT30 Plug*. URL: https://nassaunat%20ionalcable.com/products/tattu-450mah-4s1p-14-8v-75c-lipo-battery-pack-with-xt30-plug?gclid=CjwKCAjw8-OhBhB5EiwADyoY1VzjW%20JBclWb9N-9AmvjedqrX-4HIrJdTJQi7Y0TMeObg0tYOidCEthoCuNYQAvD_BwE (visited on 10/08/2022).

[71] Lauri Halonen and Markku Vainio. "Mid-infrared optical parametric oscillators and frequency combs for molecular spectroscopy". In: *Phys. Chem. Chem. Phys.* 18 (Jan. 2016). DOI: 10.1039/C5CP07052J.

[72] I.E. Gordon et al. "The HITRAN2020 molecular spectroscopic database". In: *Journal of Quantitative Spectroscopy and Radiative Transfer* 277 (2022), p. 107949. ISSN: 0022-4073. DOI: https://doi.org/10.1016/j.jqsrt.2021.107949. URL: https://www.sciencedirect.com/science/article/pii/S0022407321004416.

[73] *HITRAN Database*. URL: https://hitran.org/ (visited on 09/26/2022).

[74] Robert R. Gamache et al. “Total internal partition sums for the HITRAN2020 database”. In: *Journal of Quantitative Spectroscopy and Radiative Transfer* 271 (2021), p. 107713. ISSN: 0022-4073. DOI: https://doi.org/10.1016/j.jqsrt.2021.107713. URL: https://www.sciencedirect.com/science/article/pii/S0022407321002065.

[75] *How to Calculate Absorption Coefficient from HITRAN Data*. URL: http://home.pcisys.net/~bestwork.1/CalcAbs/CalcAbsHitran.html (visited on 10/02/2022).

[76] *U.S. Department of Commerce, NOAA - Global Monitoring Laboratory - Carbon Cycle Greenhouse Gases*. URL: https://gml.noaa.gov/ccgg/trends/mlo.html (visited on 12/05/2022).

[77] LH Allen Jr. “Variations in carbon dioxide concentration over an agricultural field”. In: *Agricultural meteorology* 8 (1971), pp. 5–24.

[78] World Health Organization et al. “Air quality guidelines for Europe 2nd ed Geneva WHO Regional Publishers”. In: (2000).

[79] Sam Wasson. *The Most and Least Humid Cities in the U.S.* URL: https://housemethod.com/moving/most-and-least-humid-cities/ (visited on 11/13/2022).

[80] Cory R Martin et al. “Evaluation and enhancement of a low-cost NDIR CO2 sensor”. In: *Atmos. Meas. Tech. Discuss* (2017), pp. 1–25.

[81] Changfeng Ge et al. “Development of a drone’s vibration, shock, and atmospheric profiles”. In: *Applied Sciences* 11.11 (2021), p. 5176.

[82] *AZoMaterials database*. URL: https://www.azom.com/ (visited on 12/15/2022).

[83] Jan Kischkat et al. “Mid-infrared optical properties of thin films of aluminum oxide, titanium dioxide, silicon dioxide, aluminum nitride, and silicon nitride”. In: *Applied optics* 51.28 (2012), pp. 6789–6798.

[84] Aleksandar D Rakić et al. “Optical properties of metallic films for vertical-cavity optoelectronic devices”. In: *Applied optics* 37.22 (1998), pp. 5271–5283.

[85] Mahmoud Al Ahmad and Robert Plana. “Piezoelectric coefficients of thin film aluminum nitride characterizations using capacitance measurements”. In: *IEEE Microwave and wireless components letters* 19.3 (2009), pp. 140–142.

[86] Jialin Wang, Mingyo Park, and Azadeh Ansari. “Thermal characterization of ferroelectric aluminum scandium nitride acoustic resonators”. In: *2021 IEEE 34th International Conference on Micro Electro Mechanical Systems (MEMS)*. IEEE. 2021, pp. 214–217.

[87] Sitao Fei and Hao Ren. “Temperature characteristics of a contour mode MEMS AlN piezoelectric ring resonator on SOI substrate”. In: *Micromachines* 12.2 (2021), p. 143.

[88] Yue Zheng et al. “Self-heating and quality factor: Thermal challenges in aluminum scandium nitride bulk acoustic wave resonators”. In: *2021 21st International Conference on Solid-State Sensors, Actuators and Microsystems (Transducers)*. IEEE. 2021, pp. 321–324.

[89] Oliver Ambacher et al. “Wurtzite ScAlN, InAlN, and GaAlN crystals, a comparison of structural, elastic, dielectric, and piezoelectric properties”. In: *Journal of Applied Physics* 130.4 (2021), p. 045102.

[90] *Concave Mirrors for Herriott Cells by Thorlabs*. URL: https://www.thorlabs.com/newgrouppage9.cfm?objectgroup_id=8169 (visited on 02/18/2023).